Interpreting the Cratering Histories of Bennu, Ryugu, and Other Spacecraft-explored Asteroids

W. F. Bottke[1] , D. Vokrouhlický[2] , R.-L. Ballouz[3] , O. S. Barnouin[4] , H. C. Connolly, Jr.[3,5] , C. Elder[6], S. Marchi[1] ,
T. J. McCoy[7], P. Michel[8] , M. C. Nolan[3], B. Rizk[3] , D. J. Scheeres[9] , S. R. Schwartz[3], K. J. Walsh[1] , and D. S. Lauretta[3]

[1] Southwest Research Institute, Boulder, CO, USA; bottke@boulder.swri.edu
[2] Institute of Astronomy, Charles University, V Holešovičkách 2, CZ-18000, Prague 8, Czech Republic
[3] Lunar & Planetary Laboratory, University of Arizona, Tucson, AZ, USA
[4] Johns Hopkins University Applied Physics Laboratory, Laurel, MD, USA
[5] Department of Geology, Rowan University, Glassboro, NJ, USA
[6] Jet Propulsion Laboratory, Caltech, Pasadena, CA, USA
[7] Smithsonian National Museum of Natural History, Washington, DC, USA
[8] Observatoire de la Côte d'Azur, CNRS, Laboratoire Lagrange, Nice, France
[9] Smead Department of Aerospace Engineering, University of Colorado, Boulder, CO, USA
Received 2020 January 27; revised 2020 April 1; accepted 2020 April 8; published 2020 June 12

Abstract

Asteroid crater retention ages have unknown accuracy because projectile–crater scaling laws are difficult to verify. At the same time, our knowledge of asteroid and crater size–frequency distributions has increased substantially over the past few decades. These advances make it possible to empirically derive asteroid crater scaling laws by fitting model asteroid size distributions to crater size distributions from asteroids observed by spacecraft. For $D > 10$ km diameter asteroids like Ceres, Vesta, Lutetia, Mathilde, Ida, Eros, and Gaspra, the best matches occur when the ratio of crater to projectile sizes is $f \sim 10$. The same scaling law applied to $0.3 < D < 2.5$ km near-Earth asteroids such as Bennu, Ryugu, Itokawa, and Toutatis yield intriguing yet perplexing results. When applied to the largest craters on these asteroids, we obtain crater retention ages of ~1 billion years for Bennu, Ryugu, and Itokawa and ~2.5 billion years for Toutatis. These ages agree with the estimated formation ages of their source families and could suggest that the near-Earth asteroid population is dominated by bodies that avoided disruption during their traverse across the main asteroid belt. An alternative interpretation is that $f \gg 10$, which would make their crater retention ages much younger. If true, crater scaling laws need to change in a substantial way between $D > 10$ km asteroids, where $f \sim 10$, and $0.3 < D < 2.5$ km asteroids, where $f \gg 10$.

Unified Astronomy Thesaurus concepts: Main belt asteroids (2036); Near-Earth objects (1092)

1. Introduction

The target of NASA's asteroid sample return mission OSIRIS-REx (Origins, Spectral Interpretation, Resource Identification, and Security–Regolith Explorer) is the near-Earth object (NEO) (101995) Bennu. Bennu has a diameter $D_{ast} \sim 0.5$ km, a 4.4% mean albedo, and a spectral signature consistent with a composition similar to CM- or CI-type carbonaceous chondrite meteorites (e.g., Hamilton et al. 2019; Lauretta et al. 2019). The retrieval and study of primitive asteroidal materials, whose provenance may go back to the earliest times of solar system history, may allow us to glean insights into the nature of planetesimal and planet formation. Another goal of the OSIRIS-REx mission is to determine whether samples from Bennu can inform us about its individual evolution, as well as that of its parent body. A critical part of this analysis will be to place Bennu's samples into a geologic, geochemical, and dynamical context, and that means learning as much as we can about Bennu's history from its physical and orbital properties. As part of this work, our goal in this paper is to interpret Bennu's cratering history and what it can tell us about Bennu's trek from its formation location, presumably in the main asteroid belt, to its current orbit (e.g., Bottke et al. 2015b).

To set the stage for our work, we first describe what has been inferred about Bennu's collisional and dynamical history to date. A plausible evolution scenario is that Bennu was created in the catastrophic disruption of a main belt parent body with $D_{ast} > 100$–200 km approximately 1–2 billion years (Ga) ago (e.g., Campins et al. 2010; Walsh et al. 2013; Bottke et al. 2015b). Using numerical simulations and building on earlier work by Campins et al. (2010) and Walsh et al. (2013), Bottke et al. (2015b) argued that Bennu most likely came from the low-albedo Eulalia asteroid family (once called the Polana family) or New Polana asteroid family (the actual family associated with (142) Polana). Both have low inclinations ($i \sim 2°$–$3°$) and are located in the region adjacent to Jupiter's 3:1 mean motion resonance at ~2.5 au. The largest remnant of the Eulalia family, likely (495) Eulalia, is located at semimajor axis $a = 2.487$ au, whereas the largest remnant of the New Polana family, (142) Polana, is at $a = 2.42$ au. The estimated age of the Eulalia family as derived from its dynamical evolution is 830 [+370, −100] Ma, whereas the age of New Polana is thought to be 1400 [+150, −150] Ma. Using suites of numerical runs, Bottke et al. (2015b) also showed that New Polana was modestly favored as a source for Bennu over Eulalia by a 70 [+8, −4]% to 30 [+4, −8]% margin, a result consistent with previous work (e.g., Campins et al. 2010).

Bennu's orbit and spin state are affected by the nongravitational Yarkovsky and Yarkovsky–O'Keefe–Radzievskii–Paddack (YORP) thermal effects (e.g., Rubincam 2000; Bottke et al. 2006a; Chesley et al. 2014; Vokrouhlický et al. 2015; Hergenrother et al. 2019; Nolan et al. 2019). The former is a small force caused by the absorption of sunlight and reemission of this energy as infrared photons (heat). The recoil produces a thrust that leads to steady changes in Bennu's semimajor axis

over long timescales. The latter is a thermal torque that, complemented by a torque produced by scattered sunlight, modifies Bennu's rotation rate and obliquity. Modeling results indicate that the YORP effect readily modified Bennu's spin axis to a value approaching $180°$, the same value it has today, and this allowed the Yarkovsky effect to drive Bennu inward across the inner main belt (e.g., Bottke et al. 2015b). Additional consequences of the YORP effect on Bennu's shape and surface are discussed below.

After spending most of its lifetime moving inward toward the Sun across the inner main belt, Bennu entered into the ν_6 secular resonance that defines the innermost boundary of the main asteroid belt. From there, Bennu was driven onto a high-eccentricity (e) orbit where it underwent encounters with the terrestrial planets. One such encounter, most likely with Earth, removed it from the ν_6 resonance and placed it onto an $a < 2$ au orbit. At that point, planetary encounters and smaller planetary resonances moved Bennu onto its current Earth-like orbit with $(a, e, i) = (1.126$ au, $0.204, 6°035)$.

At some point along the way, Bennu achieved an orbit low enough in eccentricity to become collisionally decoupled from the main belt. At that point, sizable collisions on Bennu became far less common, with the NEO population smaller by roughly a factor of 1000 than the main belt population (e.g., Bottke et al. 1994, 2015a). Using the population of 682 asteroids with $D_{ast} \geqslant 50$ km defined by Farinella & Davis (1992), Bottke et al. (1996) found that NEOs were largely safe from striking main belt bodies when their aphelion values $Q \leqslant 1.6$ au (e.g., Figures 2 and 3 of Bottke et al. 1996). According to dynamical runs from Bottke et al. (2015b), we found that the median timescale to go from this boundary to Bennu's current (a, e, i) orbit was 2.6 Ma. Most test bodies took <20 Ma, though 3% of them managed to avoid it for 70–140 Ma.

Accordingly, if Bennu came from the Eulalia or New Polana families, the time spent on an orbit collisionally decoupled from the main belt was probably a tiny fraction of its entire lifetime. Therefore, if Bennu's largest craters date back to those times, we can deduce that they were formed by main belt projectiles. For reference, comparable arguments can be made for (162173) Ryugu, the 1 km diameter carbonaceous chondrite-like target of JAXA's Hayabusa2 sample return mission (Watanabe et al. 2019), which also likely came from the Eulalia or New Polana families (Campins et al. 2013; Bottke et al. 2015b). The net number of impacts, though, may only be part of the story, particularly if Bennu has experienced frequent global crater erasure events.

The origin of Bennu's top-like shape may also tell us about its history. Bennu is a gravitational aggregate made of smaller components, what is often referred to as a "rubble-pile" asteroid (e.g., Barnouin et al. 2019; Scheeres et al. 2019). Michel et al. (2020) argue that Bennu's shape may have been derived from the reaccretion of fragments produced when the parent body was disrupted. Alternatively, it may have been spun up by YORP torques into a top-like shape (e.g., Walsh & Jacobson 2015).

The YORP effect is also active today. An analysis of rotation data spanning the years 1999–2019 indicates that Bennu is currently spinning up at a rate of $(3.63 \pm 0.52) \times 10^{-6}$ deg day^{-2} (Hergenrother et al. 2019; Lauretta et al. 2019; Nolan et al. 2019). If these kinds of accelerations were common in the past, it seems reasonable that Bennu's shape has been heavily influenced by YORP spin-up processes (Scheeres et al. 2019).

The invocation of the YORP spin-up mechanism to explain the shape of Bennu and other top-shaped asteroids, however, presents us with a paradox. If YORP is actively affecting the shape and surface properties of small asteroids, creating a dynamic environment where landslides, mass-shedding events, and satellite formation are common (e.g., Barnouin et al. 2019; Scheeres et al. 2019), one would expect to see few if any craters on that surface. Instead, an analysis of images from Bennu indicates that it has several tens of craters of diameters 10 m $< D_{crater} < 150$ m (Walsh et al. 2019). The largest craters are perhaps the most unexpected, because they are likely to be the oldest and the least susceptible to erasure via impact-induced seismic shaking (e.g., Richardson et al. 2005) or some other process. Comparable crater signatures were also found on Ryugu (Sugita et al. 2019). Like Bennu, Ryugu is top shaped and shows evidence of mass movement. Even small potato-shaped asteroids imaged by spacecraft, such as (4179) Toutatis and (25143) Itokawa, which have mean diameters of ~ 2.5 and ~ 0.3 km, show a plethora of craters, with several having diameters $D_{crater} > 100$ m (Jiang et al. 2015; Marchi et al. 2015).

When considered together, we are left with only a few options to explain the craters on these small asteroids.

Option 1 is that the surfaces of many small asteroids are in fact ancient. This implies that some process is regulating YORP-driven mass shedding. As discussed in Bottke et al. (2015b), a possible mechanism for this would be "stochastic YORP." Statler (2009) showed that modest shape changes in asteroids, produced by a variety of processes (e.g., crater formation, changes to asteroid rotational angular momentum by YORP), caused asteroids' spin rates, but not their obliquities, to undergo a random walk. This mechanism could slow down how often asteroids achieve YORP-driven mass-shedding events. In fact, Bottke et al. (2015b) found that some stochastic YORP-like process was needed to explain the orbital distribution of asteroid families such as Eulalia and New Polana. Another possible process with approximately the same effect would be that small asteroids achieve YORP equilibrium states from time to time, where further spin-up or spin-down is minimized until some shape change takes place (e.g., cratering, boulder movement; Golubov & Scheeres 2019).

Option 2 would be that Bennu's surface is relatively young, as are the surfaces of Ryugu, Itokawa, and Toutatis. The craters found on these worlds would then need to form at a much higher rate than in Option 1. One way to achieve this would be to assume that the crater–projectile scaling laws for small asteroids (hereafter crater scaling laws) allow relatively small impactors to make large craters on the surface of these $D_{ast} < 2.5$ km bodies. The crater scaling laws for Option 1 would instead predict that larger asteroids are needed to make the observed craters.

At this time, we argue that the crater scaling laws for small asteroids are not well-enough constrained to rule out Option 1 or 2 for Bennu. If we treat crater scaling laws as a free parameter, both scenarios appear to be consistent with the observational evidence we have for Bennu thus far, namely that substantial YORP accelerations have been measured (Hergenrother et al. 2019; Nolan et al. 2019), evidence for landslides exist (Barnouin et al. 2019), yet numerous craters

have been identified (Walsh et al. 2019). Comparable arguments can be made for Ryugu, Itokawa, and Toutatis.

What is needed is additional evidence that can tip the balance between Options 1 and 2. Ultimately, this comes down to finding a way to assess crater scaling laws for asteroids.

1.1. Methodology for Our Crater Production Models

In this paper, we attempt to glean insights into crater scaling laws for small asteroids like Bennu, Ryugu, Itokawa, and Toutatis by first modeling and interpreting the crater records of large main belt asteroids observed by spacecraft (i.e., diameter $D_{ast} > 10$ km). Our procedure is to create a crater production model specific to each target asteroid. This involves the calculation of several components:

1. An assessment of the size–frequency distribution (SFD) of the main asteroid belt.
2. A crater scaling law that can transform asteroid impactors from Component 1 into craters on the target asteroid.
3. A calculation of the estimated collision probabilities and impact velocities between objects in the main belt population and the target asteroid.
4. The time that a stable surface on the target asteroid (or possibly the entire target asteroid itself) has been recording craters above a threshold crater diameter. This time will be referred to in the paper as the crater retention age or surface age.

Components 1 through 3 come from models whose accuracy depends on constraints and issues that are discussed in more detail below. Component 4, the crater retention age, is an output value that is calculated from a fit between the observed crater SFD found on the surface of the target asteroid and that target's crater production model (e.g., Marchi et al. 2015).

For each crater production model, we intend to test a range of formulations for Components 1 and 2 against the crater SFD found regionally or globally on the target asteroid. This means that for every target asteroid discussed below, there will be an envelope of model main belt SFDs, possible crater scaling laws, and estimated crater retention ages that provide good fits to the data as measured using chi-squared tests. Our preference is to let these fits tell us which combinations of components yield superior results. At the completion of our runs, a confluence of similar components across many different target asteroids, each with different physical parameters, will allow us to predict those that nature prefers.

We purposely avoid terrains that have reached saturation equilibrium or have experienced substantial crater erasure. This leads us to exclude small craters below some threshold diameter from our analysis, with the definition of "small" defined on a case-by-case basis.

Our method also makes use of a number of assumptions that the reader should understand prior to a more in-depth discussion of the components within each crater production model:

Assumption 1. The size and shape of the main belt SFD has been in steady state for billions of years (within a factor of 2 or so) for projectile sizes that make observable craters on our target asteroids.

As discussed in a review by Bottke et al. (2015a), the main belt is the primary source for the near-Earth asteroid population, which in turn provides impactors to the Moon and other terrestrial planets. The evidence suggests the lunar impact flux over the last 3–3.5 Ga has been fairly constant (within a factor of 2 or so) over this time (e.g., Ivanov et al. 2002; Marchi et al. 2009; Hiesinger et al. 2012; but see also Robbins 2014 and Mazrouei et al. 2019). This constraint suggests that the main belt SFD for asteroids smaller than 10 km or so has largely been in a steady state over this time (within a factor of 2). A strongly decaying main belt SFD would produce a very different lunar impact rate.

Results of collisional evolution models also suggest that a steady state emerged in the main belt SFD over the past several billion years (e.g., Bottke et al. 2015a). Asteroid families are produced from time to time in the main belt, but their fragment SFDs are much smaller than the main belt background SFD, at least for impactor sizes of interest in this paper. Once a family is created, the SFD begins to undergo collisional evolution via the same asteroid disruption laws that affect all other asteroids. This slowly grinds the new family's SFD into the same shape as the background SFD. The consequence is that the main belt is constantly replenished by new breakup events, but these events are rarely substantial enough to strongly modify the overall main belt SFD.

A potential test of Assumption 1 is to compare the crater retention ages of target asteroids in asteroid families (or the surface of a target asteroid that can be connected with the origin of an asteroid family) with independent measures of the family's age. If the surface of the target asteroid in question has been recording impact craters from a time almost immediately after the family-forming event, we would expect all of these age constraints to be similar to one another. Examples of independent chronometers are (i) estimates of asteroid family age from models that track the dynamical evolution of family members and (ii) shock degassing ages of meteorite samples that were reset by impact heating caused by the family-forming event.

A concurrence of ages may represent potential evidence that the components applied in the crater production model are reasonably accurate. We will explore this issue below using data from the asteroids (4) Vesta, (243) Ida, and (951) Gaspra.

Assumption 2. Most main belt asteroids with diameter $D_{ast} > 10$ km are on reasonably stable orbits and commonly have been on such orbits for billions of years.

Although the main belt was potentially affected by giant-planet migration early in its history (e.g., Morbidelli et al. 2015; Vokrouhlický et al. 2016; Nesvorný et al. 2017), the conclusion of these titanic dynamical events left the majority of $D_{ast} > 10$ km asteroids on fairly stable orbits within the main belt region. From there, new $D_{ast} > 10$ km asteroids are created from time to time by family-forming events, but they are unlikely to move far from the orbits on which they were placed by the ejection event itself (e.g., Nesvorný et al. 2015).

Evidence for this comes in a variety of forms, ranging from the calculations of asteroid proper elements for larger main belt asteroids, where dynamical stability can be demonstrated (e.g., Knežević et al. 2002), to billion-year integrations of the future dynamical evolution of $D_{ast} > 10$ km asteroids, where only a small fraction can escape the main belt (Nesvorný & Roig 2018). All main belt asteroids undergo modest oscillations in their eccentricities and inclinations from secular perturbations, but the forced components of this oscillation do not modify the free components. These results indicate that

nearly all of our large target asteroids have been in the same approximate orbits for a long-enough period of time that our crater production models can be based on their present-day orbits.

Assumption 3. Models are currently the best option to estimate the main belt SFD at sub-kilometer sizes.

As discussed in more detail below, existing asteroid surveys are unable to detect large numbers of sub-kilometer main belt asteroids, and those sub-kilometer bodies that have been detected have to be carefully debiased to avoid selection effects (i.e., for a given absolute magnitude, a survey will find more high-albedo bodies than low-albedo bodies; Morbidelli et al. 2003; Masiero et al. 2011). To sidestep this limitation, we will use model main belt SFDs calculated from collision evolution models as input for our crater production models. These model main belt SFDs are constructed to fit existing main belt constraints (as we understand them) and therefore are probably the best we can do with what is available at this time (e.g., Bottke et al. 2015a).

In the next few sections, we discuss our calculations of the components discussed above, starting with Component 1, the predicted main belt SFD.

2. Deriving a Model Main Belt Size–Frequency Distribution (Component 1)

2.1. Understanding Collisional Evolution in the Main Belt

To understand cratering on Bennu and other main belt asteroids, our first task is to assess the main belt SFD (i.e., Component 1 from Section 1.1). This entails modeling how the main asteroid belt undergoes collisional evolution.

First, although the main belt has a diverse population, nearly all asteroids have orbits that cross one another, especially when secular perturbations are included (Bottke et al. 1994, 1996). For example, using the 682 asteroids with $D_{ast} > 50$ km located between 2 and 3.2 au (Bottke et al. 1994), we find that 90% and 71% of individual asteroids cross 80% and 90% of the population, respectively. Even those located along the inner-most edge of the main belt near 2.2 au can still be struck by nearly half of all main belt asteroids. Effectively, this means that there are no hiding places. Accordingly, one would expect that the shape of the impactor SFD hitting most target bodies should largely represent an amalgam of the main belt SFD as a whole.

Second, collisional evolution models indicate that the main belt SFD is in a quasi-steady state with a wave-like shape driven by the shape of the asteroid disruption law (e.g., Bottke et al. 2005a, 2005b, 2015a). Assuming all asteroids are disrupted in a similar manner, which impact modeling work suggests is a fairly reasonable approximation (e.g., Jutzi et al. 2013), simulations that produce the best match with both the main belt SFD and constraints provided by asteroid families indicate that asteroid disruption scaling laws undergo a transition between strength and gravity scaling near $D \sim 0.2$ km (Benz & Asphaug 1999; Bottke et al. 2005a, 2005b, 2015a). Asteroids near this transition are relatively easy to disrupt, leading to a relative deficit of bodies with $D_{ast} \sim 0.1$–0.5 km. This "valley" in the SFD leads to an overabundance, or a "peak," of multi-kilometer bodies that would be destroyed by such projectiles. Collisional models suggest this peak in the main belt SFD is near $D_{ast} \sim 2$–3 km (e.g., O'Brien & Greenberg 2003 reviewed in Bottke et al. 2015a).

As new-fragment SFDs are input into the asteroid belt from cratering or catastrophic disruption events, the individual bodies in the SFD undergo collisional evolution. As this grinding proceeds, for asteroids with $D_{ast} < 10$ km, the shapes of the new-fragment SFDs take on the same wavy profile as the background main belt SFD over tens to hundreds of million years (e.g., Bottke et al. 2005a, 2005b, 2015a). In this manner, the wavy shape of the main belt SFD can be considered to be in a quasi-steady state.

Collisions may not be the only mechanism affecting asteroid sizes and the wavy shape of the main belt SFD. Asteroids with diameters smaller than a few kilometers may also be affected by mass-shedding events produced by YORP thermal torques, the same processes that can modify the spin vectors of small asteroids (e.g., Marzari et al. 2011; Jacobson et al. 2014). The influence of YORP torques on asteroid sizes and the main belt SFD itself depends on the frequency of these mass-shedding events (e.g., Bottke et al. 2015a). Any changes to the main belt SFD produced by YORP mass shedding, however, would drive new-fragment SFDs to the same shape as the background main belt SFD.

The consequence is that the main belt SFD likely maintains a wavy profile that stays relatively constant over billions of years. The absolute number of asteroids in the inner, central, and outer main belt SFDs may change as asteroids are dynamically lost or as new families are formed, but modeling work suggests that these effects rarely modify the overall shape of the main belt SFD as a combined whole for very long.

2.2. Motivation for Generating a Different Main Belt Size Distribution

With that said, there are several reasons to consider formulations of the main belt SFD different from those discussed in Bottke et al. (2005b). The changes we suggest below have been driven by substantial progress in small-body studies over the last two decades. In that time, a plethora of new data has been obtained on the shape of the present-day NEO SFD from a wide variety of surveys (e.g., the Catalina Sky Survey, Lincoln Near-Earth Asteroid Research (LINEAR), Panoramic Survey Telescope and Rapid Response System (Pan-STARRS), Spacewatch, the Near-Earth Object Wide-field Infrared Survey Explorer survey) and on asteroid crater SFDs from various missions (see Sections 3 and 4). Both components —revised asteroid SFDs and new asteroid crater SFDs— suggest that the SFD presented in Bottke et al. (2005a, 2005b) may be modestly inaccurate for $D_{ast} < 1$ km.

For example, consider Figure 2 of Bottke et al. (2015a). It shows the cumulative model main belt and NEO SFDs of Bottke et al. (2005b) against recent formulations of the NEO SFD by Harris & D'Abramo (2015; see also Stokes et al. 2017). We find that the shape of the Harris & D'Abramo (2015) NEO SFD is fairly wavy, with substantial slope changes taking place near $D_{ast} \sim 0.1$–0.2 km and 2–3 km. Bottke et al. (2005b) instead predicted that (i) the smaller of the two inflection points should occur at $D_{ast} \sim 0.5$ km, (ii) that a less shallow slope should occur between 0.1–$0.2 < D_{ast} < 2$–3 km, and (iii) a less steep SFD should occur between $0.01 < D_{ast} < 0.1$ km. While features (ii) and (iii) are somewhat dependent on the removal rates of small asteroids from the main belt via the Yarkovsky effect, feature (i) cannot be explained in such a manner. In general, an inflection point in

the SFD of a source population should also be reflected in the daughter population unless removal rates are highly variable.

From the crater perspective, Figure 4 of Marchi et al. (2015) showed a fit between the Bottke et al. (2005b) formulation of the main belt SFD and the SFD of $0.1 < D_{crater} < 10$ km craters found on or near Vesta's Rheasilvia basin. It indicated that the Marchi et al. (2015) fit, while tolerable, seemed to miss a key feature and inflection point between $0.7 < D_{crater} < 2$ km. A mismatch in this size range would be consistent with Bottke et al. (2005b) predicting that a key inflection point is at $D_{ast} \sim 0.5$ km rather than 0.1–0.2 km.

There are several plausible ways we could modify the main belt SFD of Bottke et al. (2005b) in the size range of interest:

1. Modifying the Yarkovsky depletion rates of asteroids from the main belt.
2. Allowing YORP-driven mass shedding to strongly affect the diameters of sub-kilometer asteroids, as suggested by Marzari et al. (2011) and Jacobson et al. (2014).
3. Modify the disruption scaling law for main belt asteroids.

We do not favor Scenario 1. Our tests using the Bottke et al. (2005b) model indicate that to move the position of a main belt inflection point from 0.5 to 0.1–0.2 km, we would need to assume (i) much larger Yarkovsky-driven removal rates than in Bottke et al. (2005b), which would require even more main belt disruptions to keep the NEO population resupplied, and (ii) that the removal process has a size dependence between 0.1–0.2 and 0.5 km. Such changes produce strong modifications to the model NEO SFD, giving it a shape inconsistent with the observed SFD.

We find Scenario 2 to be more intriguing, with modeling work from Marzari et al. (2011) and Jacobson et al. (2014) suggesting YORP-driven mass shedding could be a major factor in decreasing the diameter of sub-kilometer bodies and thereby changing the main belt SFD. A potential concern with this hypothesis, however, is that small asteroids observed by spacecraft have a number of $D_{crater} > 0.1$ km craters (e.g., Bennu, Ryugu, Itokawa, Toutatis). If the Option 1 interpretation turns out to be true, and these asteroids have long crater retention ages for the largest craters, it would rule out substantial YORP-driven mass shedding from these worlds. Note that this does not mean that YORP is unimportant; it still provides an easy way to explain the obliquities, top-like shapes, the existence of satellites, and the mass-shedding events seen for many small asteroids (e.g., Jewitt et al. 2015). Nevertheless, it would imply that YORP's ability to influence the main belt SFD may be more limited than suggested by these models.

In this paper, we focus our investigation on Scenario 3. Our work indicates that it is possible to modify the asteroid disruption scaling law in a manner that yields a main belt SFD consistent with constraints (e.g., shape of the observed main belt SFD, number of asteroid families, asteroid craters, NEO SFD, laboratory impact experiments). With that said, though, Scenario 2 might still be a major player in explaining the shape of the main belt SFD in this size range.

2.3. Modeling Collisional Evolution in the Main Asteroid Belt

2.3.1. Collisional and Dynamical Depletion Evolution Code (CoDDEM)

Most of the asteroids that hit Bennu-sized bodies are a few tens of meters or smaller in diameter, well below the

observational limit of the asteroid belt. For reference, current surveys are only able to detect large numbers of $\sim$1–2 km diameter bodies (e.g., Jedicke et al. 2002; Gladman et al. 2009). Accordingly, the precise nature of the impactor population making craters on most asteroids observed by spacecraft is not yet known. Progress is being made, with digital tracking on ground-based telescopes having great potential (e.g., Heinze et al. 2019). New data may also become available in the 2020s from both the Large Synoptic Survey Telescope and space-based infrared surveys like the Near-Earth Object Surveillance Mission (formally NEOCam). Still, a full observational assessment of the sub-kilometer main belt SFD will not be available for some time.

Until that time arrives, it makes sense to use collisional evolution models to estimate the unknown nature of the small-body main belt SFD. To this end, we model the main belt SFD using the self-consistent one-dimensional collisional evolution code CoDDEM. Model details and the testing procedure for CoDDEM are discussed in Bottke et al. (2005a, 2005b; see also the review in Bottke et al. 2015a). Here we provide the essentials needed to understand our new results.

We run CoDDEM by entering an initial main belt SFD where the population (N) has been binned between 0.0001 km $< D <$ 1000 km in logarithmic intervals $d\log D = 0.1$. The particles in the bins are assumed to be spherical and are set to a bulk density of 2.7 g cm^{-3}, a common asteroid bulk density value. CoDDEM then computes the time rate of change in the differential population N per unit volume of space over a size range between diameters D and $D + dD$ (Dohnanyi 1969; Williams & Wetherill 1994):

$$\frac{\partial N}{\partial t}(D, t) = -I_{DISRUPT} + I_{FRAG} - I_{DYN}. \quad (1)$$

Here, $I_{DISRUPT}$ is the net number of bodies that leave between D and $D + dD$ per unit time from catastrophic disruptions. The collisional lifetime of a given target body in a bin in the current main belt is computed using estimates of the intrinsic collision probability and mean velocities between asteroids in the main belt, defined as $P_i = 2.86 \times 10^{-18}$ km^{-2} yr^{-1} and $V_{imp} = 5.3$ km s^{-1}, respectively (Bottke et al. 1994; see also Bottke et al. 2015a).

The projectile capable of disrupting D_{target} is defined as $d_{disrupt}$:

$$d_{disrupt} = \left(\frac{2Q_D^*}{V_{imp}^2}\right)^{1/3} D_{target}. \quad (2)$$

We set Q_D^* as the critical impact specific energy—the energy per unit target mass needed to disrupt the target and send 50% of its mass away at escape velocity. Our functions for Q_D^* at different asteroid sizes are tested below.

When a body breaks up, the results go into the I_{FRAG} parameter, which describes the number of bodies entering a given size bin per unit time that were produced by a given disruption event. CoDDEM uses fragment SFDs as discussed in Bottke et al. (2005a, 2005b). The implication is that the destruction of large asteroids serves as a source to replenish the small-body population via a "collisional cascade."

The I_{DYN} parameter accounts for the number of bodies lost from a given size bin via dynamical processes, such as asteroids being removed by planetary perturbations or an object entering into dynamical resonance via the Yarkovsky effect and escaping into planet-crossing orbits. This component is used to

create our synthetic NEO SFD from the main belt population, as described in Bottke et al. (2005b).

In those runs, which we exactly duplicate in our new simulations, it was assumed that the primordial main belt contained on the order of 200 times the number of objects in the existing main belt, with the vast majority of the material ejected by interactions with planetary embryos within 1–2 Myr of the formation of the first solids. The dynamical removal mechanism used in Bottke et al. (2005b) may or may not end up reflecting reality, but that is not the salient point. Their model results instead serve as a reasonable proxy for scenarios where a large population of small bodies on planet-crossing orbits early in solar system history batters the surviving main belt population. This may include the removal of primordial main belt asteroids onto planet-crossing orbits via interactions with migrating giant planets (e.g., Walsh et al. 2011) or early giant-planet instabilities (e.g., Clement et al. 2018; Nesvorný et al. 2018). It is even possible that the Bottke et al. (2005b) model results are fairly consistent with a primordial low-mass asteroid belt bombarded by populations introduced into the terrestrial planet region by planet formation processes. In terms of our model results, all these small-body sources provide an additional source of early collisional evolution that sets the stage to explain the current main belt SFD.

2.3.2. Initial Conditions and Model Constraints for CoDDEM

The initial main belt population entered into CoDDEM is divided into two components that are tracked simultaneously: a small component of main belt asteroids that will survive the dynamical excitation event ($N_{\rm rem}$) and a much larger component that will be excited and ejected from the main belt ($N_{\rm dep}$). Thus, our initial population is $N = N_{\rm rem} + N_{\rm dep}$. We can use this procedure because we know in advance the dynamical fate of each population via the dynamics simulations described in Bottke et al. (2015b). The two populations undergo comminution with themselves and with each other. When $N_{\rm dep} = 0$, CoDDEM tracks the collisional and dynamical evolution of $N_{\rm rem}$ alone for the remaining simulation time.

The size and shape of our initial size distribution were determined by running different initial populations through CoDDEM-like codes, then testing the results against the constraints described in Section 4 (Bottke et al. 2005a, 2005b). The size distribution that provided the best fit for $N_{\rm rem}$ followed the observed main belt for bodies with $D_{\rm ast} > 200$ km, an incremental power-law index of -4.5 for bodies with $110 < D_{\rm ast} < 200$ km, and an incremental power-law index of -1.2 for bodies with $D_{\rm ast} < 110$ km (Bottke et al. 2005b). The initial shape of the $N_{\rm dep}$ population is always the same as $N_{\rm rem}$, and its size is set to $N_{\rm dep} = 200\, N_{\rm rem}$. Additional starting condition details can be found in Bottke et al. (2005a, 2005b).

For constraints in Bottke et al. (2005b), our model main belt SFD at the end of 4.6 Ga of evolution had to reproduce the wavy-shaped main belt SFD for $D_{\rm ast} > 1$ km. To determine its value, we converted the absolute magnitude H distribution of the main belt described by Jedicke et al. (2002), who combined observations of bright main belt asteroids with renormalized results taken from the Sloan Digital Sky Survey (Ivezić et al. 2001), into a size distribution. This was accomplished using the relationship (Fowler & Chillemi 1992; Appendix in Pravec & Harris 2007)

$$D_{\rm ast}(\text{km}) = 1329 \times 10^{-H/5}\, p_v^{-1/2} \qquad (3)$$

and a representative visual geometric albedo $p_v = 0.092$. The shape of the main belt SFD is shown as the large dots in
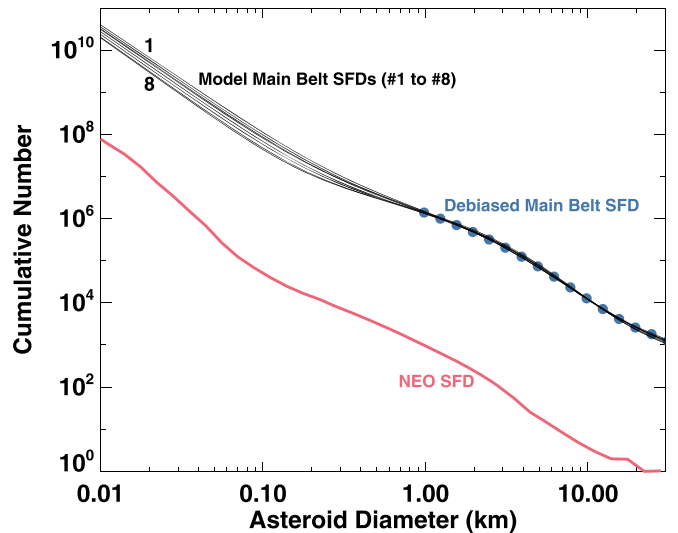

Figure 1. Collisional evolution model results for the main asteroid belt, based on the assumptions and model results of Bottke et al. (2005b). The model SFDs #1–8 are assigned an index number corresponding to the asteroid disruption laws Q_D^* #1–8 shown in Figure 2 (i.e., SFD #1 was produced by Q_D^* #1, and so on). SFD #1 was designed to match the one used in Bottke et al. (2005b). The blue dots represent the debiased main belt SFD as discussed in Bottke et al. (2005a, 2005b). For reference, the red line shows the NEO SFD as defined by Harris & D'Abramo (2015). As shown in Figure 2, the higher index numbers correspond to lower minimum values for Q_D^*. This allows more asteroids to disrupt between $0.1 < D_{\rm ast} < 1$ km, which in turn means the power-law slope of the SFD becomes shallower in that range. The upturn in slope occurs at larger sizes for low index numbers ($\sim$0.5 km for #1) and smaller sizes for high index numbers ($\sim$0.2 km for #8).

Figure 1. This SFD is in general agreement with the diameter-limited survey produced by WISE (Masiero et al. 2011), though their study is only complete in the outer main belt to asteroids larger than $D_{\rm ast} > 5$ km. It also has had some success matching crater SFDs on asteroids (e.g., Marchi et al. 2015), though we will return to this issue below.

There have been many additional attempts to estimate the shape of the main belt SFD since Bottke et al. (2005a, 2005b). We only mention a few of these examples here. Gladman et al. (2009) used a pencil beam survey of main belt asteroids and their likely colors to generate their SFD. Test fits of their SFD against crater SFDs on Vesta, however, have not been as successful as those derived from Bottke et al. (2005a, 2005b; Marchi et al. 2012a). Ryan et al. (2015) used the Spitzer space telescope to target known objects, find their diameters, and eventually generate a main belt SFD. Their results are similar to Gladman et al. (2009) in many respects. Accordingly, their SFD would likely also have similar problems matching constraints.

A potential issue with the results from Gladman et al. (2009) and Ryan et al. (2015) is how their methods treat observational selection effects near the detection limit of main belt surveys. In an absolute magnitude-limited survey, it is easier to detect high-albedo S-type asteroids than low-albedo C-type asteroids. This bias is pervasive through the catalog of known main belt objects. Studies employing this catalog may be overemphasizing S types at the expense of C-types, which are numerous in the outer main belt. This effect was demonstrated by Masiero et al. (2011), who showed that nearly all of the main belt asteroids discovered by WISE were low albedo. Up to that

point, these bodies had been missed by telescopes looking in visual wavelengths.

Finally, a formulation of the main belt SFD by Minton et al. (2015) indicated that it should change slope close to $D_{ast} \sim 3.5$ km. We point out that this break is discordant with the shape of the inner main belt SFD determined by the diameter-limited WISE survey, which shows no change in slope at that size (Masiero et al. 2011). We also see no change in slope at $D_{ast} \sim 3.5$ km in the observed NEO SFD (Harris & D'Abramo 2015; Stokes et al. 2017; Figure 1); recall that the main belt is the primary source for NEOs, so a change in slope in the parent size distribution should probably be seen in the daughter size distribution as well.

A second set of constraints for Bottke et al. (2005a, 2005b) was provided by asteroid families, particularly those that are potentially too large to be dispersed by the Yarkovsky effect over the age of the solar system. Using hydrocode simulations from Durda et al. (2007) to estimate the amount of material in families located below the observational detection limit, Bottke et al. (2005a, 2005b) suggested that ~20 families have been produced by the breakup of $D_{ast} > 100$ km asteroids over the past ~3.5 Ga. Although there have been recent attempts to update this number (e.g., see the review of this issue in Bottke et al. 2015a), we believe that the distribution used by Bottke et al. (2005b) is still reasonable. Here we adopt the same constraint; we assume that the size distribution bins centered on $D_{ast} = 123.5$, 155.5, 195.7, 246.4, 310.2, and 390.5 km experienced 5, 5, 5, 1, 1, and 1 breakups over the past 3.5 Ga, respectively. Our testing procedure also gives us some margin, so assuming that additional large asteroids were disrupted over the past 3.5 Ga can be considered reasonable as well.

To quantify the fit between the model and observed population, we follow the methods described in Bottke et al. (2005a, 2005b). Our first metric compares the shape of the model main belt SFD to a small envelope of values surrounding the observed main belt SFD (defined as N_{MB}):

$$\psi_{SFD}^2 = \sum_D \left(\frac{N_{REM}(D) - N_{MB}(D)}{0.2 \, N_{MB}(D)} \right)^2. \quad (4)$$

We assume that our model is a good fit if it lies within 20% of the observed main belt between 0.98 and 390.5 km (across 27 incremental bins) as defined by Bottke et al. (2005a; see also Jedicke et al. 2002). As discussed in Bottke et al. (2005a), the 20% value was determined experimentally via comparisons between model results and data. Tests indicate that $\psi_{SFD}^2 < 20$ provides a reasonable match between model and data, with $\psi_{SFD}^2 < 10$ indicating a very good fit. The second metric is a standard χ^2 test where the fit between the model and observed families, χ_{FAM}^2, is better than 2σ (i.e., probability >5%).

2.3.3. Testing Different Asteroid Disruption Laws

In Bottke et al. (2005b), a range of Q_D^* functions was input into CoDDEM to see which ones would most consistently reproduce (i) the observed main belt SFD, (ii) the number and distribution of large-asteroid families, and (iii) the approximate shape of the NEO SFD known at that time (Section 2.2). Given that collisional evolution is a stochastic process, each run, defined by a set of initial conditions, was tested 100 times with

different random seeds. Success or failure for the trials was determined by our testing metrics (Section 2.2).

This method to compare our model results to observations has limitations, in that it assumes that the actual main belt SFD is a byproduct of our most successful Q_D^* function. We do not know whether this is true. It is possible that the actual main belt is an outlier compared to expectations from a given collisional evolution scenario, with its properties coming from a number of stochastic breakup events. For this paper, we will assume that is not the case and that our main belt is average in a statistical sense. We consider this approach to be reasonable given the available information that exists on the main belt.

The best-fit Q_D^* function in Bottke et al. (2005b) was similar to the one defined by the hydrocode modeling results of Benz & Asphaug (1999) and the Q_D^* function Test #1 (hereafter Q_D^* #1) shown in Figure 2 (see also Table 1). It has the shape of a hyperbola, with the Q_D^* function passing through a normalization point $(Q_{D_{LAB}}^*, D_{LAB}) = (1.5 \times 10^7 \text{ erg g}^{-1}, 8 \text{ cm})$, a value determined using laboratory impact experiments (e.g., Durda et al. 1998; Figure 2). Other Q_D^* functions in the literature have approximately the same convergence point for small target sizes, namely 10^7 erg g^{-1}, with materials tested ranging from hard rocks to sand to small glass microspheres (e.g., Holsapple & Housen 2019).

The minimum Q_D^* value ($Q_{D_{min}}^*$) for Q_D^* #1 was found near 1.5×10^6 erg g^{-1} at $D_{min} = 0.2$ km. This combination yielded the model main belt SFD #1 shown in Figure 1 (hereafter model SFD #1). Model SFD #1 has an inflection point near $D_{ast} = 0.5$ km, which we will show below is modestly inconsistent with asteroid crater constraints.

For our work here, we choose to modify Q_D^* #1 enough to match our new constraints (asteroid craters) without sacrificing the fit we had in Bottke et al. (2005b) to our original constraints (shape of the main belt SFD at large sizes, prominent asteroid families). In practice, this means changing the Q_D^* #1 hyperbola by (i) lowering $Q_{D_{min}}^*$ while keeping D_{min} near 0.2 km, (ii) allowing the hyperbola to recover at larger sizes so it matches Q_D^* #1 as closely as possible for $D_{ast} > 100$ km, and (iii) forcing the hyperbola to pass through the normalization point $(Q_{D_{LAB}}^*, D_{LAB})$. The change in (i) will help us disrupt additional bodies of size $0.1 < D_{ast} < 0.5$ km, which in turn will slide the inflection point shown in model SFD #1 near $D_{ast} = 0.5$ km to smaller sizes.

Our new Q_D^* functions are defined by the following equations:

$$Q_D^*(R) = aR^\alpha + bR^\beta, \quad (5)$$

$$a = \frac{Q_{D_{LAB}}^*}{R_{LAB}^\alpha} \frac{1}{1 - \frac{\alpha}{\beta} \left(\frac{R_{LAB}}{R_{min}} \right)^{\beta - \alpha}}, \quad (6)$$

$$b = -\frac{\alpha}{\beta} a R_{min}^{\alpha - \beta}. \quad (7)$$

Here, $R = D/2$ and $R_{LAB} = D_{LAB}/2$. The parameters for our different Q_D^* functions, and their rate of success against our main belt testing metrics are given in Table 1.

We show our model SFDs #1–8 in Figure 1. These test runs, corresponding to Q_D^* #1–8 (Figure 2; Table 1), indicate that decreasing $Q_{D_{min}}^*$ helps lower the critical inflection point to smaller values. Moreover, in comparison to our baseline Q_D^* #1 and model SFD #1, we find that most of our new Q_D^* functions produce a comparable fraction of successful outcomes, as displayed in Table 1. Only Q_D^*#7 and Q_D^*#8
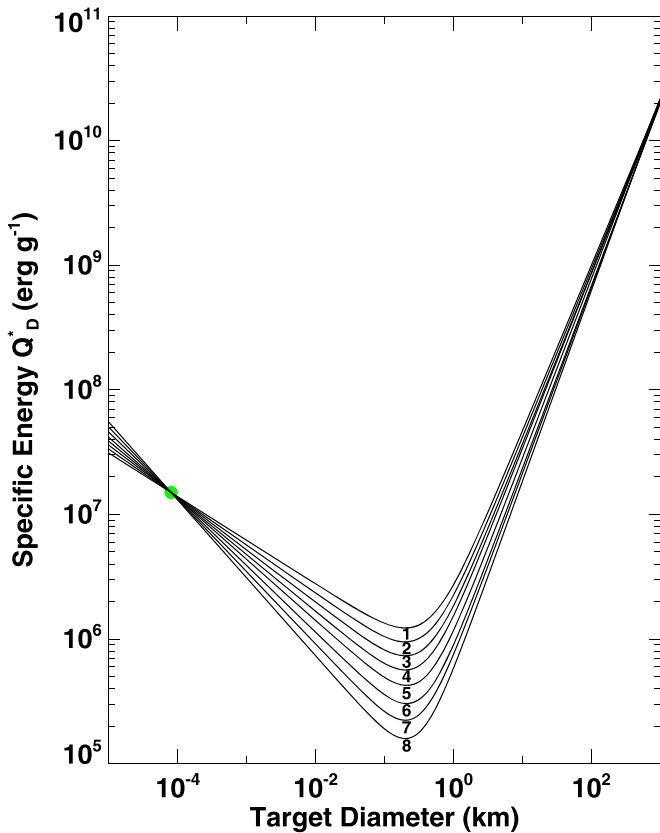
Figure 2. The asteroid disruption laws used in our collisional evolution model runs. Each disruption law Q_D^* is assigned an index number #1–8, and they produce the model main belt SFDs shown in Figure 1 (i.e., SFD #1 was produced by Q_D^* #1, and so on). The parameters needed to generate the curves can be found in Table 1. Disruption law Q_D^* #1 matches the one used in Bottke et al. (2005b). The green dot is a normalization point determined from laboratory impact experiments. It is defined as $(Q_{D_{LAB}}^*, D_{LAB}) = (1.5 \times 10^7 \, \mathrm{erg \, g^{-1}}, \, 8 \, \mathrm{cm})$ (e.g., Durda et al. 1998) The minimum Q_D^* value $(Q_{D_{min}}^*)$ for all of the functions is near $D_{min} = 0.2$ km.

Table 1
The Parameters Used to Define the Eight Q_D^* Asteroid Disruption Functions Tested in This Paper, and How They Fared against Constraints

Test #	D_{min} (km)	α	β	% Trials with $\psi_{SFD}^2 < 20$ and $\chi_{FAM}^2 > 2\sigma$	% Trials with $\psi_{SFD}^2 < 10$ and $\chi_{FAM}^2 > 2\sigma$
1	0.2	−0.35	1.33	37	21
2	0.2	−0.385	1.35	36	30
3	0.2	−0.42	1.37	41	28
4	0.2	−0.455	1.405	47	26
5	0.21	−0.49	1.44	34	23
6	0.21	−0.535	1.465	33	22
7	0.2	−0.58	1.49	20	2
8	0.2	−0.625	1.53	12	0

Note. The parameters in columns 2 to 4 are D_{min}, defined as the location of the minimum Q_D^* value and the two variables α and β, which are applied in Equations (5)–(7) to derive Q_D^*. Columns 5 and 6 describe the number of trials out of 100 test runs that match both of our main belt constraints. The metric ψ_{SFD}^2, defined by Equation (4), describes how well the model main belt SFD compares to the observed main belt SFD. The metric χ_{FAM}^2 is a χ^2 test where the fit between the model and observed families (for parent bodies $D_{ast} > 100$ km) is better than 2σ (i.e., probability >5%).

produce less than satisfying outcomes. They cannot be ruled out, but they should not be considered the top choices.

The power-law slopes of the SFDs for $D_{ast} < 0.1$ km in Figure 1 range from $q = -2.6$ cumulative for SFD #1 to $q = -2.7$ for SFD #8. These outcomes match predictions from O'Brien & Greenberg (2003), who show that the slope of the Q_D^* function in the strength regime, defined using the α parameter in Table 1, yields these approximate values for the α range shown there (i.e., −0.35 to −0.63). Our results also match observational constraints of the main belt SFD from Heinze et al. (2019), who used Dark Energy Camera observations of main belt asteroids and digital tracking methods to find a slope of $-2.575 < q < -2.825$.

The cumulative power-law slope between the inflection points in Figure 1, located between $D_{ast} \sim 0.2$–0.5 km and 2–3 km, is shallower than the q values above. If we measure the slope for all of our model SFDs between 0.5 and 1.5 km, we find values that go from $q = -1.5$ for SFD #1 to $q = -1.2$ for SFD #8. Heinze et al. (2019) report a cumulative slope in this range of $q = -1.31 \pm 0.01$, a value that matches Yoshida & Nakamura (2007; $q = -1.29 \pm 0.02$) but slightly disagrees with Yoshida et al. (2003; $q = -1.2$). If we assume the preferred slope in this part of the main belt SFD is indeed $q = -1.3$, the best match comes from SFD #6, with $q = -1.3$.

The intriguing matches between our SFDs and observational data are necessary but not sufficient proof that our Q_D^* functions reflect reality. For example, Holsapple & Housen (2019) point out that asteroid disruption scaling laws with α parameters more negative than −0.5 are inconsistent with those inferred from materials tested to date. They instead argue that slopes in the strength regime of −0.2 to −0.3 provide the best matches with scaling law theory. Taken at face value, the best match to α parameters of −0.2 to −0.3 comes from our baseline Q_D^* #1, which yields model SFD #1 within CoDDEM. As we will show below, however, this SFD does not reproduce crater SFDs on many different asteroids as well as other choices.

There are different ways to potentially resolve this paradox beyond simply assuming that our collisional evolution model is inaccurate. The first possibility would be that YORP spin-up is indeed a major factor in the disruption of small asteroids (i.e., Scenario 2 from Section 2.2) and that the demolition of small asteroids from this effect is needed in combination with Q_D^* #1 to get the correct SFD. In other words, our steeper α parameter is compensating for the lack of YORP disruption in our model.

A second possibility is that existing impact studies have not yet accounted for the unusual material properties found on some small asteroids. For example, in Hayabusa2's Small Carry-on Impactor (SCI) experiment, a 2 kg copper plate was shot into the surface of the kilometer-sized carbonaceous chondrite-like asteroid Ryugu at $2 \, \mathrm{km \, s^{-1}}$, where it made a semicircular crater with a rim to rim diameter of 17.6 ± 0.7 m (Arakawa et al. 2020). This outcome was a surprise to many impact modelers, in that Ryugu's surface acted like it had the same strength as cohesionless sand upon impact (i.e., the crater formed in the gravity-dominated regime). Related studies suggest that the boulders on Ryuyu have estimated porosities as large as 55% (Grott et al. 2019). Put together, these results may indicate that modified asteroid disruption laws are needed to accommodate how carbonaceous chondrite-like asteroids with Ryugu-like properties behave in a disruption event.

The stage is now set to test our eight bounding model asteroid SFDs (Figure 1) against observed crater SFDs on asteroids observed by spacecraft.

3. Crater Scaling Laws for Asteroids (Component 2)

To determine the crater retention age of a given asteroid surface, we need to know the crater scaling law that turns projectiles into craters. Typical crater scaling laws require a range of projectile quantities (e.g., size, mass, impact velocity, impact angle, composition, internal structure) and target quantities (e.g., target gravity, surface composition, structure and density, target interior structure and density, effects of surface and internal porosity). Unfortunately, many of these quantities are unknown for observed asteroids. Our ability to calibrate crater scaling laws is also somewhat limited, given that most test data come from laboratory shot experiments, conventional explosions, or nuclear bomb detonations. The energies involved in making observed asteroid craters is typically orders of magnitude higher than the energies used to generate our crater scaling law constraints, even those from nuclear blasts.

3.1. Holsapple & Housen Crater Scaling Law

A common crater scaling law used in asteroid studies is similar to the Holsapple & Housen (2007) formulation of the Pi-group scaling law (e.g., used by Marchi et al. 2015; see also Tatsumi & Sugita 2018):

$$D_t = kd\left[\frac{gd}{2V_P^2}\left(\frac{\rho}{\delta}\right)^{2\nu/\mu} + \left(\frac{Y}{\rho V_P^2}\right)^{(2+\mu)/2}\left(\frac{\rho}{\delta}\right)^{\nu(2+\mu)/\mu}\right]^{-\mu/(2+\mu)}.$$
(8)

Here, the transient crater diameter, defined by D_t, can be found by using the impactor properties (impactor diameter d, velocity perpendicular to the surface V_p, bulk density δ) together with the target properties (density of target material ρ, strength of target material Y, surface gravity g).

For planets and large asteroids, the input of surface gravity g into such crater scaling law equations is straightforward; the combination of their largely spherical shapes and relatively slow spin rates means accelerations across their surfaces are similar. For smaller asteroids, however, the calculation of an effective surface gravity can be complicated by irregular shapes and centrifugal forces.

As an example, consider (243) Ida. Its elongated shape ($59.8 \times 25.4 \times 18.6$ km) and rapid spin period ($P = 4.63$ hr) lead to a wide range of surface accelerations (0.3–1.1 cm s^{-2}; Thomas et al. 1996). Therefore, when applying this scaling law to Ida, we follow the lead of Schmedemann et al. (2014) and choose a single representative g value from this range (i.e., 0.7 cm s^{-2}) as input into our crater scaling laws. We follow suit for the other target asteroids in this paper, whose g values, along with a corresponding reference, are given in Table 2.

Additional parameters (k, ν, μ) account for the nature of the target terrain (i.e., whether it is hard rock, cohesive soil, or porous material). Common parameters for hard rocks are $k = 0.93$, $\nu = 0.4$, and $\mu = 0.55$, and for cohesive soils are $k = 1.03$, $\nu = 0.4$, and $\mu = 0.41$ (e.g., Marchi et al. 2012b, 2015).

The yield strength Y of different asteroid target materials is unknown, but we can bracket possibilities using reference values, which range from lunar regolith ($Y = 1 \times 10^5$ dynes cm^{-2}; 3×10^5 dynes cm^{-2} at 1 m depth) to dry soil ($Y = 3 \times 10^6$ dynes cm^{-2}) to dry desert alluvium ($Y = 7 \times 10^5$ dynes cm^{-2}) to soft dry rock/hard soils ($Y = 1.3 \times 10^7$ dynes cm^{-2}) to hard rocks and cold ice ($Y = 1.5 \times 10^8$ dynes cm^{-2}) (Holsapple & Housen 2007). In general, when yield strength increases, the craters formed from projectiles are smaller, which translates into an older surface for a given crater SFD.

We also account for the collapse of the transient crater, such that the final crater size is $D_{\text{crater}} = \lambda D_t$. The value λ is $\geqslant 1$, and it is usually determined empirically. A common value for λ is 1.2, but smaller and larger values can also be found in the literature.

In terms of the final crater size, our tests show that larger values for λ can be counteracted by increasing Y; the two trade off of one another. To keep things simple when asteroid parameters are largely unknown and to limit the amount of interpretation needed for our results, we decided to apply $\lambda = 1.2$ and vary Y for our results. Hence, we assume that

$$D_{\text{crater}} = 1.2\, D_t.$$
(9)

3.2. Ivanov Crater Scaling Law

Another commonly used asteroid scaling law, reformulated from Schmidt & Housen (1987), comes from Ivanov et al. (2001; see corrected version in Schmedemann et al. 2014). It has the form

$$\frac{D_t}{d(\delta/\rho)^{0.43}(V_p \sin\alpha)^{0.55}} = \frac{1.21}{[(D_{\text{SG}}+D_t)g]^{0.28}}.$$
(10)

Here, the yield strength and related parameters from Schmidt & Housen (1987) have been substituted in favor of a term that accounts for the strength-to-gravity transition on an asteroid surface (D_{SG}). For the work here, D_{SG} is defined relative to the lunar value, with $D_{\text{SG}} = D_{\text{SG}}^{\text{Moon}}(g_{\text{Moon}}/g)$, $D_{\text{SG}}^{\text{Moon}} = 0.3$ km, and $g_{\text{Moon}} = 1.62$ m s^{-2} (Schmedemann et al. 2014). The input values for g and D_{SG} are given in Table 2. Note that with the exception of Ceres and Vesta, whose D_{SG} values are near 2 km, all asteroids listed in Table 2 have D_{SG} values larger than the craters examined in this paper.

The impact angle of the projectile, α, is assumed to be 45°, the most probable impact angle for projectiles hitting a surface (Shoemaker 1962).

For large craters on big asteroids like Ceres, it is assumed in the Ivanov scaling law that the craters undergo collapse following the equation:

$$D_{\text{crater}} = \frac{D_t^{\eta+1}}{D_{\text{SC}}^{\eta}}.$$
(11)

Here, $\eta = 0.15$ and D_{SC} is defined as the final rim diameter where simple craters transition into complex craters, which is assumed to be 10 km on Ceres (Hiesinger et al. 2016).

To verify that our coded versions of Equations (10) and (11) function correctly for the results presented below, we reproduced the lunar and asteroid crater production functions shown in Figure 3 of Schmedemann et al. (2014; i.e., their normalized crater production curves for the Moon, Vesta (versions 3 and 4), Lutetia, Ida, and Gaspra). In this situation, input parameters were taken from their paper.

A general comment should also be made about this scaling law versus the Holsapple & Housen (2007) formulation. Both are based on the same general Pi-scaling theory and have a similar heritage (e.g., Schmidt & Housen 1987). The difference is that the Holsapple & Housen (2007) scaling law as shown in

Table 2
Compilation of Asteroid Surface Gravities and Strength-to-Gravity Transition Diameter Values Used for the Crater Scaling Laws in This Paper

Asteroid/Region Name	Effective Surface Gravity (cm s^{-2})	Strength-to-Gravity Transition Diameter D_{SG} (km)	Reference
Ceres (Kerwan Basin)	28	1.75	Hiesinger et al. (2016)
Vesta (Rheasilvia Basin)	25	1.94	Russell et al. (2012)
Lutetia (Achaia Region)	4.7	49	Patzold et al. (2011)
Mathilde	0.96	51	Thomas et al. (1999)
Ida	0.7	69	Thomas et al. (1996)
Gaspra	0.5	97	Thomas et al. (1994)
Eros	0.4	120	Thomas et al. (2002)

Equation (8) has free parameters for the various strength parameters that can be selected to match our best understanding of asteroid materials, whereas the Ivanov et al. (2001) scaling law in Equation (10) has those parameters built in. Presumably, one could select material parameters for the Holsapple & Housen (2007) scaling law to make it closer to the Ivanov et al. (2001) scaling law, and one could reformulate the Ivanov et al. (2001) scaling law to have additional options as well. Therefore, the differences between the scaling laws are essentially choices in how asteroids are predicted to behave.

3.3. Empirical Crater Scaling Law

A new element in this work is to use empirical methods to derive the appropriate asteroid scaling laws. Our method can be explained using two thought experiments.

For the first one, we consider a cumulative projectile and crater SFD defined as "broken" power laws: two power laws with different slopes that either meet at an inflection point or join each other over a slow bend (often called a "knee"). For this example, we assume that the projectile and crater SFDs are not congruent. If one wanted to glean insights into the nature of the crater scaling law, the first thing to do would be to compare the inflection points or knees between the projectile and crater SFDs. Assuming that the crater scaling law is not pathological, these locations must correspond to one another. Their connection yields the relationship between the diameter of the projectile D_{ast} and the diameter of the final crater D_{crater}. We call this ratio

$$f = \frac{D_{crater}}{D_{ast}} \quad (12)$$

and use it throughout the paper. It is the simplest possible crater scaling law. In this example, there is only one value for *f*, but it can still be a powerful constraint if one desires to test crater scaling laws and impact models.

For the second thought experiment, we again assume that we have broken power laws for projectile and crater SFDs but that their shapes are congruent. By mapping the shape of the projectile SFD onto the crater SFD, one can empirically obtain the crater scaling law *f* for all sizes where data exist. In our idealized situation, no other information is needed; the myriad crater scaling parameters for projectile and target properties are folded into the factor *f*.

When we started this project, we assumed that the first thought experiment was most likely to be applicable. As we show below, however, the projectile and crater SFDs used here are in fact excellent matches to the second thought experiment. This suggests that we can calculate empirical crater scaling laws for a wide range of crater sizes on different asteroids, provided their crater SFDs have a knee or that we have

sufficient alternative constraints to rule out other possible scaling laws. As we will show, this method leads to powerful insights about the craters formed on different asteroids.

Using *f* values, one could presumably constrain more sophisticated crater scaling laws that describe how a given impact outcome is affected by different projectile and target quantities. The difficulty would be to overcome the degeneracy between the variables, such as the trade-off between impact velocity, projectile size, etc. We do not perform such work here, but it would be an interesting follow-up project.

4. Collision Probabilities between Target and Main Belt Asteroids (Component 3)

Two additional components are needed to model the collisional evolution of individual asteroids and interpret their crater histories: the intrinsic collision probabilities P_i and mean impact velocities V_{imp} of our target asteroids against the main belt population. There are many published formalisms to calculate these parameters that yield comparable results; a short list includes Öpik (1951), Wetherill (1967), Kessler (1981), Farinella & Davis (1992), Bottke et al. (1994), Vedder (1998), Manley et al. (1998), Dell'Oro et al. (2001), and Vokrouhlický et al. (2012). In this paper, we use the methodology of Bottke et al. (1994).

For cratering events, the P_i parameter can be defined as the likelihood that a given projectile will hit a target with a given cross-sectional area over a unit of time. In most such cases, the size of the projectile is small enough to be ignored. For each pair of bodies, it can be considered to be the product of two combined probabilities:

1. The probability that two orbits, with orbit angles that uniformly precess on short timescales, are close enough to one another that a collision can take place. It is the calculation of the volume of the intersection space of the pair of orbits.
2. The probability that both bodies will be at their mutual orbital-crossing location at the same time.

Our first task is to identify an appropriate projectile population that can hit our target asteroids. At that point, we compute individual P_i and V_{imp} values for all of the bodies on crossing orbits with the target. The (*a, e, i*) values of each pair are entered into the collision probability code, with the integral examining and weighting all possible orientations of the orbits, defined by their longitudes of apsides and nodes. This approximation is valid because secular perturbations randomize these values over $\sim 10^4$ yr timescales.

The most difficult part of this task is finding the appropriate impactor population. Consider that most asteroid craters observed to date have been produced by projectiles smaller

Table 3
The Intrinsic Collision Probabilities (P_i) and Impact Velocities (V_{imp}) for Main Belt Asteroids Observed by Spacecraft

Ast. #	Asteroid/Region Name	Proper a (au)	Proper e	Proper i (deg)	N_{cross}	P_i (10^{-18} km^{-2} yr^{-1})	V_{imp} (km s^{-1})
1	Ceres (Kerwan Basin)	2.7670963	0.1161977	9.6474113	642 (out of 681)	3.455	4.860
4	Vesta (Rheasilvia Basin)	2.3615127	0.0987580	6.3923416	372 (out of 681)	2.878	4.710
21	Lutetia (Achaia Region)	2.4352603	0.1292457	2.1461887	491 (out of 681)	3.763	4.379
243	Ida	2.8616140	0.0456271	2.0883834	582 (out of 682)	4.037	3.720
253	Mathilde	2.6477821	0.2189155	6.5350556	666 (out of 681)	3.723	5.237
951	Gaspra	2.2097211	0.1475680	5.0786877	327 (out of 682)	2.635	4.924
2867	Steins	2.3635361	0.1082622	9.3526096	392 (out of 682)	2.785	5.154

Note. The first column is the asteroid number. The second column is the name of the asteroid, with the name of the region examined in parentheses where applicable. The proper semimajor axis a, eccentricity e, and inclination i values were taken from the Asteroids Dynamic Site, AstDyS (https://newton.spacedys.com/astdys/). The comparison population of 682 asteroids with $D_{ast} \geqslant 50$ km was taken from Farinella & Davis (1992), and N_{cross} describes the number of these bodies on crossing orbits with the target asteroid.

than the observational limit of the main belt (roughly $D_{ast} \sim 1$–2 km). Moreover, the catalog of main belt objects suffers from observational selection effects, particularly as one approaches the observation limit. This makes it difficult to find a completely nonbiased sample of main belt bodies for collision probability calculations.

Most asteroids discovered to date have been found by surveys limited in absolute magnitude (H). In general, for a given H value, it is easier to detect high-albedo S-type asteroids than low-albedo C-type asteroids. Any study employing this catalog needs to worry about overemphasizing S types at the expense of C types, particularly in the outer main belt where C types dominate the population.

To mitigate against these problems, it is common to use a complete population of main belt asteroids as a statistical proxy for the population of smaller projectiles. For example, Bottke et al. (1994) used 682 asteroids with $D_{ast} \geqslant 50$ km as defined by Farinella & Davis (1992) for their collision probability calculations. The use of this sample is imperfect because family SFDs may be important at small asteroid sizes, but it may be the most reasonable approximation that we can make at this time, as we show below.

As a test, we also experimented with using the WISE diameter-limited catalog of main belt objects. The WISE catalog is incomplete, yet using it leads to results that are interesting in many ways. Masiero et al. (2011) showed that the ratio of the number of outer to inner main belt asteroids becomes larger as one goes from $D_{ast} \geqslant 50$ km to $D_{ast} \geqslant 10$ km and then decreases again as one goes to $D_{ast} \geqslant 5$ km. The latter effect occurs because the power-law slope of the inner main belt between $5 < D_{ast} < 10$ km is slightly steeper than that of the outer main belt over the same size range. The outer main belt appears to become observationally incomplete for $D_{ast} < 5$ km, so we perform no calculations beyond this point.

This change in population has little effect on the collision probabilities of asteroids residing in the outer main belt, but it can be important for those in the inner main belt. As a demonstration of this effect, we selected (951) Gaspra for a series of P_i tests against the WISE catalog.

Using Gaspra's proper (a, e, i) values of (2.20974 au, 0.1462, 4°.77253) (Table 3), we calculated a mean P_i value for WISE asteroids on Gaspra-crossing orbits of 5.67, 5.15, and 5.39×10^{-18} km^{-2} yr^{-1} for bodies of $D_{ast} \geqslant 50$, 10, and 5 km. Little change is seen between the values.

If we then fold in the population not on crossing orbits, which is needed to derive the approximate impact flux on Gaspra, the values change to 2.67, 1.74, and 2.11 $\times$

10^{-18} km^{-2} yr^{-1}, with 252 out of 535, 2289 out of 6754, and 15,044 out of 38,437 on crossing orbits. The low value for $D_{ast} > 10$ km is notable, in that it is only 65% of the value for $D_{ast} \geqslant 50$ km. The mean P_i value then partially recovers for $D_{ast} \geqslant 5$ km because the inner main belt has a steeper SFD than the outer main belt. If we assume this trend holds to $D_{ast} \geqslant 2$ km, it seems likely that the mean P_i value for Gaspra will once again approach that derived for $D_{ast} \geqslant 50$ km. New work on debiasing the WISE asteroid catalog is needed to confirm this hypothesis.

Given these trends and considerations, we argue that a reasonable compromise is to continue to use the 682 asteroids with $D_{ast} \geqslant 50$ km discussed in Farinella & Davis (1992) and Bottke et al. (1994) for our collision probability calculations of main belt bodies. Table 3 shows our results for all main belt asteroids observed by spacecraft. We obtained their proper (a, e, i) elements from the Asteroids Dynamic Site, AstDyS, which is located at https://newton.spacedys.com/astdys/.

5. Results for Main Belt Asteroids and Near-Earth Asteroids Larger than 10 km

In this section, we examine the crater histories of the following asteroids observed by spacecraft: Vesta, Ceres, Lutetia, Mathilde, Ida, and Gaspra, which are all main belt asteroids, and Eros, a near-Earth asteroid. All have average diameters larger than 10 km. We start with main belt asteroids that have the largest size range of craters and work down to Gaspra, the smallest main belt asteroid in this list. Eros is actually larger than Gaspra, but we address it last to discuss the prospective relationship between Eros, Gaspra, and the Flora asteroid family.

While this list is long, it is not comprehensive. We avoid modeling certain asteroid terrains where crater saturation is prevalent, such as those on the main belt asteroid Steins and the northern hemisphere of Vesta (Marchi et al. 2015; see also Marchi et al. 2012a). To be cautious, we also decided to bypass sub-kilometer craters in the crater SFD of Ceres, in part because they were potentially influenced by secondary cratering. Our analysis of those terrains is left for future work.

Finally, there are many proposed crater counts and crater retention ages for the asteroids or features discussed below. We focus here on published craters and ages that are most germane to testing our scaling laws and methods. For the interested reader who wants to know more, including a list of references about the craters found on these worlds, a good place to start would be to examine these papers: Chapman (2002),
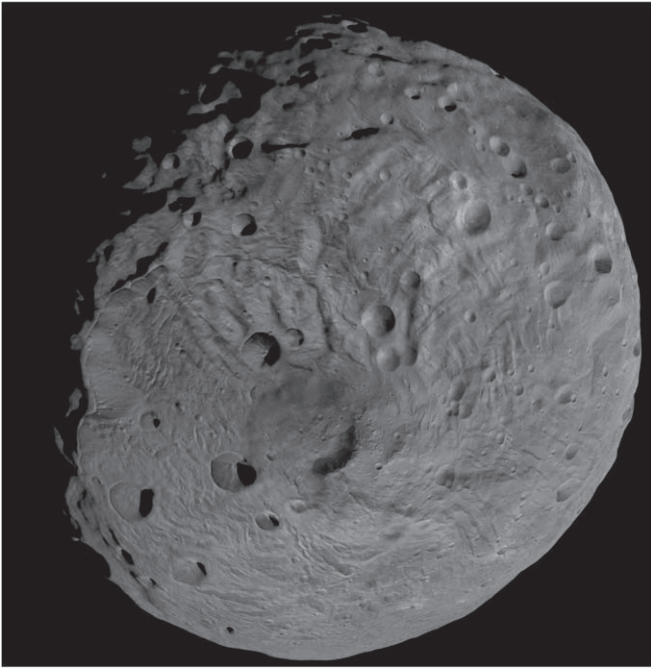
Figure 3. The south pole of the V-type asteroid Vesta, which is dominated by the 505 km diameter basin Rheasilvia. The image was obtained by the framing camera on NASA's Dawn spacecraft, a distance of about 1700 miles (2700 km). The feature at the lower center of the image contains Rheasilvia's central peak. The image resolution is about 260 m per pixel. Craters between a few kilometers to tens of kilometers can be seen superposed on Rheasilvia's surface. Courtesy of NASA/JPL-Caltech.

O'Brien et al. (2006), Schmedemann et al. (2014), and Marchi et al. (2015).

5.1. Rheasilvia Basin on Vesta

(4) Vesta is the second largest main belt asteroid. It is located in the middle of the inner main belt with proper orbital elements of $(a, e, i) = (2.36 \text{ au}, 0.099, 6°4)$. NASA's Dawn spacecraft imaged its surface at varying spatial resolutions and verified that Vesta had differentiated into a metallic core, silicate mantle, and basaltic crust. Some key physical parameters for Vesta include dimensions of 572.6 km × 557.2 km × 446.4 km, a bulk density of $3.456 \pm 0.035 \text{ g cm}^{-3}$, and a surface gravity of 0.25 m s^{-2} (Russell et al. 2012).

Here we reexamine the superposed crater SFD on or near Vesta's Rheasilvia basin, a 500 km diameter impact structure that defines the shape of Vesta's southern hemisphere (e.g., Schenk et al. 2012; Figure 3). We choose this region for our modeling work for two reasons: Rheasilvia is young enough that crater saturation is not an issue, and it is broad enough that it is covered by a large range of crater diameters ($0.15 < D_{crater} < 35$ km; Marchi et al. 2015).

The craters identified and used here are located on Rheasilvia's floor and ejecta blanket; their properties are reported in Marchi et al. (2015; see also Marchi et al. 2014 for earlier counts). Their work indicated that a plausible age for Rheasilvia was ~1 Ga (Marchi et al. 2012a). Model components that went into this age include (i) the main belt SFD described by Bottke et al. (2005b) (SFD #1 in Figure 1), (ii) an intrinsic collision probability between main belt asteroids and Vesta of $P_i = 2.8 \times 10^{-18} \text{ km}^{-2} \text{ yr}^{-1}$, and (iii) the Holsapple & Housen (2007) scaling law for cohesive soils ($Y = 2 \times 10^7 \text{ dynes cm}^{-2}$).

Their estimated crater retention age for Rheasilvia is comparable to the $^{40}\text{Ar}/^{39}\text{Ar}$ ages of feldspar grains in the brecciated howardite Kapoeta, which were reset by a thermal event between 0.6 and 1.7 Ga ago (Lindsay et al. 2015). Lindsay et al. suggested that the source of the heating event was the formation of the Rheasilvia basin 1.4 ± 0.3 Ga ago. They also pointed out that this age is similar to other $^{40}\text{Ar}/^{39}\text{Ar}$ ages found among the HED (howardite–eucrite–diogenite) meteorites. A range of ages between 0.6 and 1.7 Ga seems plausible given these data.

Note that $^{40}\text{Ar}/^{39}\text{Ar}$ ages between 3.5 and 4.1 Ga have also been identified in eucrites. These ages are older than the crater retention ages found for Rheasilvia by Schenk et al. (2012) and Marchi et al. (2013). Using their own crater counts and comparing their model to craters with a more limited dynamic range than those works, Schmedemann et al. (2014) argued that Rheasilvia had a crater retention age that matched those ancient values. We will address this issue below.

The Rheasilvia basin-forming event also ejected numerous fragments onto escape trajectories, and these bodies likely comprise Vesta's color-, spectral- and albedo-distinctive asteroid family (e.g., Parker et al. 2008; Masiero et al. 2015; Nesvorný et al. 2015). Using a collisional evolution model, Bottke (2014) found that the Vesta family's steep SFD, composed of bodies of $D_{ast} < 10$ km, showed no indication of a change produced by collisional grinding. On this basis, they estimated that the Vesta family has an 80% probability of being <1 Ga old. The orbital distribution of the family members, and how they have likely been influenced by the Yarkovsky thermal forces, also suggests an age of ~1 Ga (Spoto et al. 2015), though we caution that the high ejection velocity of the family members makes it difficult to precisely determine the family's dynamical age (e.g., Nesvorný et al. 2015).

The combined crater sets of Rheasilvia presented in Marchi et al. (2015) yield 48 craters between $0.15 < D_{crater} < 35$ km (Figure 4). Two knees are seen in the crater SFD: one near $D_{crater} \sim 2$ km and a second near $D_{crater} \sim 20$ km. The smaller of the two knees is likely related to the inflection points seen between $0.2 < D_{ast} < 0.6$ km in the main belt SFDs shown in Figure 1. The origin of the larger knee will be discussed below.

5.1.1. Empirical Scaling Law Derived by Fitting Model and Observed Crater SFDs (Rheasilvia)

To compare the shape of Vesta's crater SFD to the impactor SFDs shown in Figure 4, we defined two parameters: (i) the crater scaling relationship factor $f = D_{crater}/D_{ast}$ and (ii) the age of the Rheasilvia surface T_{ast}. The number of model craters forming per square kilometer on the surface of the asteroid, $N_{model\text{-}crater}$ ($>D_{crater}$), as a function of time T_{ast} is given by the equation

$$N_{model\text{-}crater}(>D_{crater}) = \frac{P_i \, T_{ast} \, N_{model\text{-}ast}(> D_{ast})}{4\pi}. \quad (13)$$

The number of model asteroids larger than a given size D_{ast} is given by $N_{model\text{-}ast}$ ($>D_{ast}$), which can be found in Figure 1.

The quality of the fit between the observed crater SFD on Rheasilvia (Figure 4) and those modeled is defined using chi-squared methods:

$$\chi^2 = \sum_{i=1}^{M} \frac{(N_{model\text{-}crater}(> D_i) - N_{obs\text{-}crater}(> D_i))^2}{N_{obs\text{-}crater}(> D_i)}. \quad (14)$$

Here, $D_i = 1, \ldots, M$, stands for the diameters of observed and model craters on a given asteroid surface. To obtain normalized

Table 4
Compilation of Results Where Model and Observed Crater SFDs were Compared to One Another

Asteroid Name	M (# Crater Data Points)	Empirical Fit: Best-fit SFD	χ^2_{MB} Best Fit	SFDs That Fit Within 1σ	HH Scaling: Best-fit SFD	χ^2_{MA} Best Fit	SFDs That Fit Within 1σ	Ivanov Scaling: Best-fit SFD	χ^2_{IV} Best Fit	SFDs That Fit Within 1σ
Ceres-KB	22	8	2.84	6–7	8	4.61	7	8	9.44	⋯
Vesta-RB	48	5	22.32	4,6–8	7	19.34	6	8	70.51	⋯
Lutetia-AR	17	7	1.97	3–6, 8	7	2.24	5–6, 8	8	4.00	7
Mathilde	12	2	2.67	1,3–6	4	2.60	1–3,5	8	4.98	3–7
Ida	16	8	1.17	1–7	6	1.39	1–5, 7–8	8	1.93	1–7
Gaspra	14	1	1.94	2–8	1	1.93	2–8	1	1.85	2–8
Eros	12	2	3.72	1,3–8	1	3.85	2–7	8	2.27	1–8

Note. The index numbers 1–8 corresponds to the eight Q_D^* asteroid disruption functions and eight model main belt SFDs (Figures 1–2; Table 1). The results are given for the three different crater scaling laws discussed in Section 3. The second column is M, the number of crater data points on the asteroid or asteroid region in question (see Equation (14)).
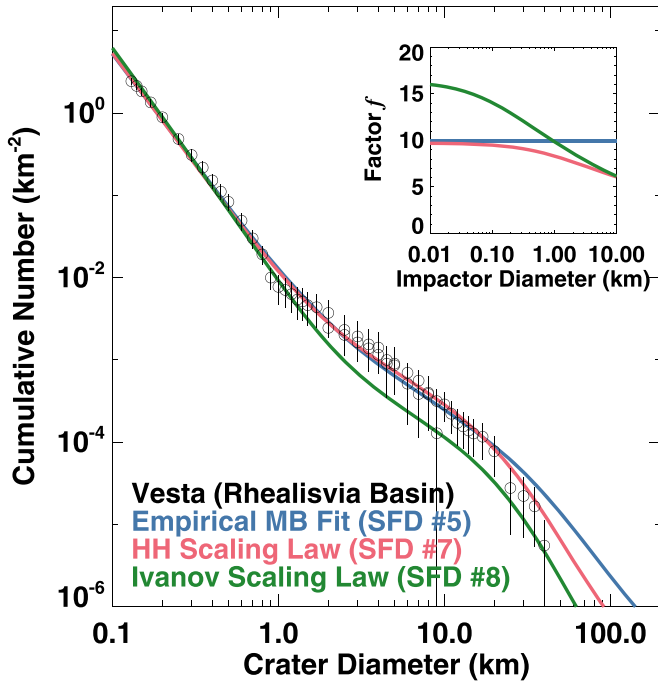
Figure 4. A comparison between the observed crater SFDs found on the floor and ejecta blanket of Vesta's Rhealsivia basin and various crater models. The observed crater counts are from Marchi et al. (2015). The best-fit model crater SFDs for three different crater scaling laws are shown with the colored lines: the main belt empirical fit in blue (Section 5.1.1), the HH crater scaling law fit in red (Section 5.1.2), and the Ivanov crater scaling law in green (Section 5.1.3). The numbers in parentheses correspond to the index number of the model main belt SFD applied to produce the model crater SFD (Figure 1). See Section 5.1.1 for a discussion of the error bars. The inset figure shows the ratio $f = D_{crater}/D_{ast}$ for the different crater scaling laws as a function of the impacting asteroid's diameter. The best-fit model crater SFD is the HH scaling fit, though the main belt empirical fit matches everything but the very largest craters. The Ivanov scaling fit produces a model crater SFD that is lower than the observed data for $D_{crater} > 1.5$ km.

χ^2 values, one should divide them by the value M, yielding the value we define here as χ^2_{norm}. In this case, there were 48 Rheasilvia craters, so $M = 48$ (Table 4).

By creating an array of (f, T_{ast}) values $5 < f < 25$, incremented by 0.1, and $0.01 < T_{ast} < 5$ Ga, incremented by 0.01 Ga, we were able to test all plausible fits between model and observed crater data. These values also allow us to

calculate confidence limits of 68% (1σ) and 95% (2σ) relative to our best-fit case that can be used to estimate error bars.

An additional issue with fitting a model SFD to a crater SFD is that the smallest craters in N ($>D_{crater}$), which have the most data and the smallest error bars but also are closest to the observation limit, tend to dominate the χ^2 values. To mitigate against this effect, we multiplied the error bars of N ($>D_{crater}$) by a function γ that increases the error bars of the smaller craters according to

$$\gamma = (w - 1)\frac{\log_{10}\left(\frac{D_{crater}}{D_{crater}^{max}}\right)}{\log_{10}\left(\frac{D_{crater}^{min}}{D_{crater}^{max}}\right)} + 1. \tag{15}$$

Here, we set w to 3–5 for the asteroid craters in this paper, with D_{crater}^{min} and D_{crater}^{max} defined by the minimum and maximum crater sizes in a given set, respectively.

Using the P_i value in Table 3, our best-fit case was found for SFD #5. It yielded $\chi^2_{MB} = 22.32$ (Table 4). SFDs #4–8 yielded values within 1σ of this best-fit case. Our best-fit f value was 9.90, with 1σ of -1.40 and $+1.00$, whereas our best-fit crater retention age for Rheasilvia was $T_{ast} = 0.85$ Ga, with 1σ errors of -0.23 and $+0.24$ Ga (Table 5). The visual fit to the crater data in Figure 4 is good except for $D_{crater} > 20$ km craters. It is possible that the mismatch in this range stems from small number statistics.

5.1.2. Housen & Holsapple Crater Scaling Fit (Rheasilvia)

We also examined how our main belt SFDs compared to Rheasilvia's superposed craters using the Holsapple & Housen (2007) formulation of the Pi-group crater scaling law (Equations (8) and (9)). Hereafter, we call this the HH crater scaling law.

Following the procedure used by Marchi et al. (2015) and applying his chosen parameters for Equations (8) and (9), we assumed that Vesta's surface could be treated like it had the same material properties as cohesive soils ($k = 1.03$, $\nu = 0.4$, $\mu = 0.41$). We assumed that the projectile density was 2.5 g cm^{-3} and Vesta's surface density was 3.0 g cm^{-3}. After some trial and error, we found that the lowest χ^2_{MB} values were generated from $Y = 2 \times 10^7$ dynes cm^{-2}. We use this value for all of the asteroids discussed below. The values of P_i and V_{imp} are found in Table 3.

Table 5
Best-fit Empirical Scaling Law Fit Values for f (Equation (12)) and Crater Retention Ages for Different Main Belt Asteroid Surfaces Using Different Crater Scaling Laws

Asteroid Name	Empirical Fit factor f	Empirical Fit: Age for Best Fit (Ga)	HH Scaling: Age for Best Fit (Ga)	Ivanov Scaling: Age for Best Fit (Ga)
Ceres-KB	8.20 [−1.40, +1.00]	0.91 [−0.17, +0.17]	0.70 [−0.02, +0.03]	0.47 [−0.01, +0.02]
Vesta-RB	9.90 [−1.40, +1.00]	0.85 [−0.23, +0.24]	1.24 [−0.06, +0.06]	0.37 [−0.02, +0.01]
Lutetia-AR	10.30 [−4.90, +3.60]	2.57 [−2.02, +1.64]	3.07 [−0.41, +0.41]	1.24 [−0.16, +0.16]
Mathilde	10.00 [−3.40, +1.90]	3.70 [−1.30, +1.52]	2.85 [−0.50, +0.50]	0.85 [−0.15, +0.15]
Ida	10.90 [−2.70, +2.90]	2.52 [−1.98, +0.94]	2.91 [−0.43, +0.43]	1.17 [−0.17, +0.16]
Gaspra	10.10 [−3.70, +3.80]	0.74 [−1.74, +0.41]	0.73 [−0.07, +0.07]	0.17 [−0.01, +0.01]
Eros	10.90 [−3.00, +3.00]	2.03 [−2.01, +0.86]	2.10 [−0.29, +0.28]	1.40 [−0.19, +0.18]

Note. The ages in the last three columns are given in units of billions of years (Ga). These values correspond to the best-fit cases, but other fits may be within 1σ of these results (Table 4). The main text gives the preferred values, which take into account additional constraints.

Our best-fit came from SFD #7, which yielded $\chi^2_{\mathrm{MA}} = 19.34$ (Table 4). This value indicates that our fit here is modestly superior to the empirical scaling law results in Section 5.1.1. The reason is that their f value decreases for larger projectiles, allowing SFD #7 to match Rheasilvia's craters with $D_{\mathrm{crater}} > 20$ km.

Our apparent success for large crater sizes, however, may be an issue. Existing numerical hydrocode simulations indicate that the 500 km Rheasilvia basin formed from the impact of a 37–60 km diameter projectile (Ivanov & Melosh 2013; Jutzi et al. 2013), which corresponds to $f = 8.3$–13.5. These latter values are a good match to the f values predicted by our empirical scaling law results (Figure 4, Table 4).

If f indeed decreases substantially for large craters, as shown by the red curve in the inset figure within Figure 4, it would imply that much larger impactors—perhaps $D_{\mathrm{ast}} > 100$ km—would be needed to make Rheasilvia. We find this to be an unlikely scenario. We discuss this issue further in Section 5.1.4.

Our best-fit crater retention age for this set of parameters is $T_{\mathrm{ast}} = 1.24$ [−0.06, +0.06] Ga (Table 5). This value matches the ages of Marchi et al. (2012a) and the $^{40}\mathrm{Ar}/^{39}\mathrm{Ar}$ age constraints from Lindsay et al. (2015), but it is modestly older than the empirical fit results in Section 5.1.1. The reasons are that (i) this scaling law yields f values that are consistently lower than the empirical main belt best-fit results of $f = 9.9$, which increases the surface age, and (ii) SFD #7 is shallower at small asteroid sizes and therefore has fewer small projectiles; few projectiles mean older ages.

5.1.3. Ivanov Crater Scaling Fit (Rheasilvia)

The last scaling law investigated was that from Ivanov et al. (2001) (Equations (10) and (11)). Our input parameters for this equation were given in Section 5.1.2. The best fit is from SFD #8, but χ^2_{IV} in this case ended up as 70.51, a value indicative of a poor fit. The reason is that this scaling law produces larger f values than the others tested for impactors of $D_{\mathrm{ast}} < 0.1$–0.2 km. To fit the smallest craters on Rheasilvia, the production function must substantially undershoot the craters with $D_{\mathrm{crater}} > 1$ km, as shown in Figure 4.

The best-fit crater retention age is $T_{\mathrm{ast}} = 0.37$ [−0.02, +0.01] Ga, a value that is considerably younger than the two previous test cases. It falls outside the $^{40}\mathrm{Ar}/^{39}\mathrm{Ar}$ age range of the Kapoeta feldspar grains (0.6–1.7 Ga; Lindsay et al. 2015). It also does not match constraints on Vesta family's age from dynamics (Spoto et al. 2015). As before, the reason has to do with the large f values applied here; if smaller projectiles make larger craters, the surface has to be younger.

Our crater retention ages are different from those of Schmedemann et al. (2014), who use the same scaling law to get 3.5 ± 0.1 Ga (though some surfaces have reported ages of 1.7–1.8 Ga; see their Table 6). Only a minor portion of this difference can be attributed to their use of different collision probabilities or impact velocities; their values are nearly the same as the ones we show in Table 3. Similarly, in our tests of their work, we find that their derived main belt SFD is similar to our SFD #8 in Figure 1.

The main reason that Schmedemann et al. (2014) report a crater retention age for Rheasilvia different from our work is that they focus on comparing their crater production function to crater sizes between several kilometers and several tens of kilometers in diameter. As our Figure 4 shows, if one ignored all craters smaller than a few kilometers, the best-fit curve for the Ivanov scaling law would shift to substantially higher values, with f values that are closer to those of the HH scaling law and the empirical main belt fit scaling law. These effects would in turn yield substantially older crater retention ages.

There may be valid reasons why one should ignore fitting a crater production function model to small craters on a given surface, and it is possible that one can obtain reasonable results by only looking at the largest craters on a surface. Nevertheless, where practical, it is better to compare a crater model across an entire size range of craters rather than a subset. For this reason, we argue that this crater scaling law does not perform as well at modeling Vesta's crater SFD in Figure 4 as the other choices.

5.1.4. What Projectile Sizes Make the Largest Basins on Vesta?

In Section 5.1.2, we asserted that we favor $f \sim 10$ to make the largest basins on Vesta. One reason is that these values are consistent with hydrocode simulations, where the 500 km Rheasilvia basin formed from the impact of a 37–60 km diameter projectile (Ivanov & Melosh 2013; Jutzi et al. 2013). A second reason is that it matches f values predicted by our empirical scaling law results (Figure 4, Table 4). A third reason comes from the following calculation (see also Bottke et al. 2015a).

The two largest basins on Vesta are Rheasilvia and Veneneia, with diameters of ~500 and ~400 km, respectively. Veneneia is partially buried by Rheasilvia, so its estimated crater retention age is >2 Ga (Schenk et al. 2012). Both formed after the emplacement of Vesta's basaltic crust, which solidified within a few million years of solar system formation (e.g., Hopkins et al. 2015). In the following calculation, we will assume these basins were produced by $f = 5$, which would require impacts from $D_{\mathrm{ast}} \geqslant 90$ km and 100 km bodies, or

$f = 10$, which would require impacts from $D_{ast} \geqslant 40$ km and 50 km bodies. If we assume the main belt had approximately the same population of large asteroids over the last 4.5 Gyr as it has today, such that we can use the SFD in Figure 1 over this interval, the population of $D_{ast} \geqslant 40$, 50, 90, and 100 km asteroids in the main belt is 860, 680, 270, and 220, respectively. Using $P_i = 2.8 \times 10^{-18} \, km^{-2} \, yr^{-1}$, the probability that these projectiles will collide with Vesta over 4.5 Gyr is 0.79, 0.65, 0.30, and 0.25 for $D_{ast} \geqslant 40$, 50, 90, and 100 km, respectively.

Accordingly, for $f = 5$, the probability that both Rheasilvia and Veneneia will form on Vesta is $0.30 \times 0.25 = 7\%$, while for $f = 10$, the probability is $0.79 \times 0.65 = 51\%$. The latter value is seven times higher than the former. This does not mean the real scaling law must be $f \sim 10$, but it is fair to say that $f \sim 10$ makes it easier to match constraints.

5.1.5. Summary (Rheasilvia)

Our results for Vesta allow us to make some initial observations about how to interpret crater SFDs on asteroids.

1. Results for the empirical fit and HH crater scaling laws indicate that the Rheasilvia formation event probably took place between ∼0.6 Ga and ∼1.3 Ga ago. This result is consistent with dynamical, collisional evolution, and meteorite constraints.
2. If an asteroid's crater SFD has a knee near $D_{crater} \sim 2$ km, it indicates that an f value near ∼10 will allow it to match the main belt SFD. If f values are substantially smaller or larger than 10, one can only fit the small craters in the SFD at the expense of missing the larger ones, or vice versa.
3. Main belt asteroid SFDs that remain shallow between ∼0.2–$0.3 < D_{ast} < 2$–3 km, results that are represented by SFDs #4 to #8 in Figure 1, appear to be the most successful at matching constraints on Vesta.
4. Using the Holsapple & Housen (2007) formulation of the Pi-group scaling law, we find that input parameters for cohesive soils appear to allow us to best match observations.
5. Scaling laws that have f values substantially smaller than 10 for craters of $D_{crater} \sim 20$ km on Rheasilvia are needed to match data, but an extrapolation of this trend would make it difficult to produce Rheasilvia and Veneneia basins. Our interpretation is that this may make $f \sim 10$ a reasonable choice for all of the observed crater data on or near the Rheasilvia basin.

5.2. Ceres's Kerwan Basin

(1) Ceres, with dimensions of 965.2 ± 2.0 km $\times$ 961.2 ± 2.0 km $\times$ 891.2 ± 2.0 km, is the largest asteroid in the main belt (Park et al. 2016). It is located near the outer edge of the central main belt, with proper orbital elements of $(a, e, i) = (2.77$ au, 0.12, $9°.6)$. It is classified as a C-type asteroid, and observations from the DAWN spacecraft indicate that it is a volatile-rich rocky body. Studies based on DAWN spacecraft data have provided us with many critical parameters for Ceres, including its bulk density of $2.160 \pm 0.009 \, g \, cm^{-3}$ and a surface gravity of $0.28 \, m \, s^{-2}$ (Russell et al. 2016). The mineralogy and geochemistry of Ceres, as constrained by Dawn observations, appear consistent with the bulk composition of CM/CI carbonaceous chondrites (McSween et al. 2018).

Figure 5. The largest crater on C-type asteroid Ceres is the Kerwan basin. It is ∼284 km in diameter (Williams et al. 2018) and has a relaxed polygonal shape. The center of the basin is located at $10°.8$ south latitude and $123°.9$ east longitude. The image was taken during Dawn's survey phase from an altitude of 4400 km. Courtesy of NASA/JPL-Caltech.

The nature of the craters on Ceres suggests that its surface may be intermediate in strength between that of Vesta and Rhea, the icy satellite of Saturn (Russell et al. 2016). The lack of crater relaxation observed for smaller craters, however, indicates that the crust may be deficient in ice and could be a mechanically strong mixture of rock, carbonates or phyllosilicates, ice, and salt and/or clathrate hydrates (Fu et al. 2017). Curiously, Ceres is missing very large craters ($D_{crater} > 280$ km) and is highly depleted in craters of diameter 100–150 km compared to expectations from the shape of the impacting main belt SFD (Marchi et al. 2016). Their absence could suggest the viscous relaxation of long-wavelength topography, perhaps via a subsurface zone of low-viscosity weakness (Fu et al. 2017).

To glean insights into the nature of Ceres's crust, we examine the superposed crater SFD associated with Ceres's Kerwan basin (Figure 5). Geologic mapping work indicates that Kerwan is the oldest, largest (undisputed) impact crater on Ceres ($D_{crater} \sim 284$ km; Williams et al. 2018). The derived age of the basin depends on the superposed crater counts and the crater age model used (see the crater SFDs from Williams et al. 2018), but craters counted in the smooth unit of Kerwan, which range from approximately $5 < D_{crater} < 100$ km, yield ages of 550 ± 90 Ma and 720 ± 100 Ma (Hiesinger et al. 2016). With that said, none of the model crater SFDs shown in Figure 8 of Hiesinger et al. (2016) appear to reproduce the shape of the crater SFD, and the above ages seem to be determined by best fits to the largest craters.

Here we compare our model crater SFDs to craters counted by coauthor S. Marchi. They have approximately the same crater SFD as Hiesinger et al. (2016). The crater counts have been slightly updated and are shown in Figure 6. The observed inflection point in these crater SFD occurs near $D_{crater} \sim$ 20 km, approximately the same size as seen for Vesta's Rheasilvia basin (Figure 4). Accordingly, our prediction is that
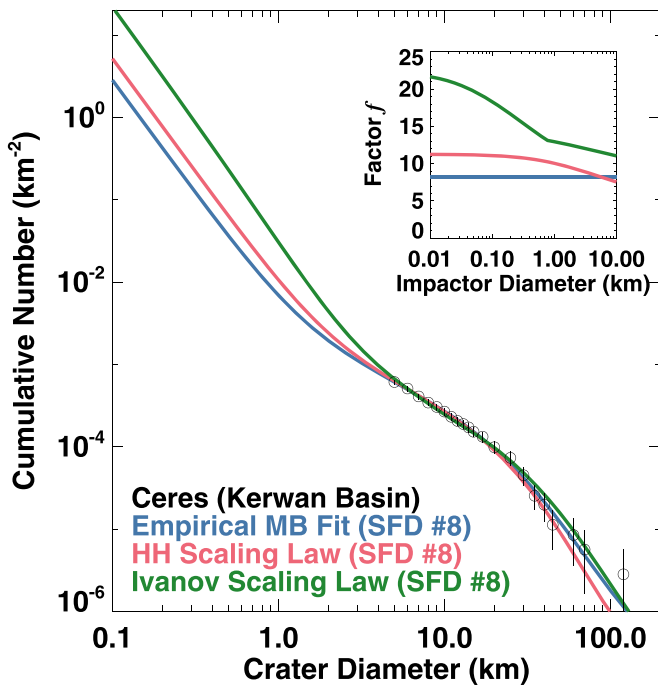
Figure 6. A comparison between the observed crater SFDs found on or near the Kerwan basin on Ceres and various crater models. The observed crater counts are from coauthor S. Marchi. Plot components are as in Figure 4. The best-fit model crater SFD is the empirical main belt fit (Table 3). The predicted ages for the Kerwan basin are ~0.8–0.9 Ga from the empirical main belt fit and the HH scaling law. The Ivanov scaling law predicts an age of ~0.5 Ga, smaller than the other two scaling laws because its f values in the inset figure are much higher.

the Kerwan and Rheasilvia basins should have similar crater scaling laws.

5.2.1. Empirical Scaling Law Derived by Fitting Model and Observed Crater SFDs (Kerwan)

Using our empirical main belt fit method and a P_i value of $3.455 \times 10^{-18}\,\mathrm{km}^{-2}\,\mathrm{yr}^{-1}$ (Table 3), we found that our best fit comes from SFD #8, which yielded $\chi^2_{MB} = 2.84$ (Table 4). Both SFDs #6 and 7 yielded values within 1σ of this best-fit case.

Our best-fit f value was 8.20 [−1.40, +1.00], and our best-fit crater retention age was $T_{ast} = 0.91$ [−0.17, +0.17]. The latter value is modestly higher than those in Hiesinger et al. (2016), even though our collision probability P_i value is higher than their value of $2.84 \times 10^{-18}\,\mathrm{km}^{-2}\,\mathrm{yr}^{-1}$. The reason is because SFD #8 has fewer small bodies than the SFD in Bottke et al. (2005b; SFD #1), which was used in their "asteroid-derived" model. Visually, the empirical main belt crater model reproduces the crater data reasonably well.

If we were to choose a more probable main belt SFD according to Table 1, such as SFD #6, our best-fit f value is 8.8 [−1.70, +1.20] and our best-fit crater retention age T_{ast} is 0.86 [−0.18, +0.18] Ga.

5.2.2. Housen & Holsapple Crater Scaling Fit (Kerwan)

Our comparison between model and data using the Holsapple & Housen (2007) formulation of the Pi-group scaling law also produced a reasonable match with Rheasilvia

craters (Figure 4). As with our Vesta runs, we assumed that Ceres's surface had the strength of cohesive soils ($k = 1.03$, $\nu = 0.4$, $\mu = 0.41$), with projectile and target surface density set to 2.5 and 1.5 g cm^{-3}, respectively. The yield strength was $Y = 2 \times 10^7$ dynes cm^{-2}, and the values of $_{Pi}$ and V_{imp} are found in Table 3. This scaling law yielded a best fit using SFD #8, with $\chi^2_{MA} = 4.61$, modestly higher than the empirical main belt fit of $\chi^2_{MB} = 2.84$. Here, the slight mismatch stems from the model crater SFD missing the craters with $D_{crater} > 40$ km. The best-fit crater retention age in this circumstance is $T_{ast} = 0.70$ [−0.02, +0.03] Ga, fairly close to the main belt fit result (Table 5).

5.2.3. Ivanov Scaling Law Fit (Kerwan)

The fit using the Ivanov crater scaling law is only modestly better than the HH scaling law case, with $\chi^2_{IV} = 9.44$. The f values are larger here across the board than the other two scaling law cases, with crater sizes increasing substantially for $D_{ast} < 1$ km. The best-fit crater retention age here is $T_{ast} = 0.47$ [−0.01, +0.02] Ga, younger than the previous two test cases (Table 5).

With this said, there are indications in other Kerwan crater databases not investigated in this paper that the slope of the observed crater SFD indeed becomes substantially steeper for craters with $D_{ast} < 1$ km, as predicted by the Ivanov scaling law (e.g., Williams et al. 2018). If so, the crater SFD on Kerwan is radically different from the one observed in Vesta's Rheasilvia basin. It seems unlikely that the main belt SFD changed over the timescales in question, so this mismatch between Vesta and Ceres implies that the f-value function is different for sub-kilometer craters on the two worlds.

Finally, we note that it is plausible that the observed difference between sub-kilometer craters on Kerwan and Rheasilvia is because secondary craters are pervasive across Ceres for $D_{crater} < 2$–3 km.

5.2.4. Summary (Kerwan)

As with the Rheasilvia basin on Vesta, the best-fit matches in Table 4 come from the empirical main belt fit and the HH scaling law fit. As before, our results favor the high-number SFDs, with the best fit coming from #8, a value that is modestly disfavored from probability studies (Table 1). If we use a more probable SFD, such as SFD #6 (Table 1), the empirical scaling law $f \sim 9$, with errors that overlap with our $f \sim 10$ solution for the Rheasilvia basin (Table 5). The age of the Kerwan basin favored by our results is ~0.8–0.9 Ga.

5.3. Lutetia's Achaia Region

(21) Lutetia is an M-type asteroid with dimensions of 121 ± 1 km $\times$ 101 ± 1 km $\times$ 75 ± 13 km (Sierks et al. 2011; Figure 7). It is located in the inner main belt and has proper orbital elements of $(a, e, i) = (2.43$ au, 0.13, 2°.1$)$. The flyby of Lutetia by ESA's Rosetta mission yielded a bulk density of 3.4 ± 0.3 g cm^{-3} (Sierks et al. 2011). The composition of Lutetia is unknown, though it is thought to be related to enstatite chondrites or possibly the metal-rich CH carbonaceous chondrites (Coradini et al. 2011; Moyano-Cambero et al. 2016).

Marchi et al. (2012b) examined craters on the oldest observed surface imaged by Rosetta, a flat and uniform region
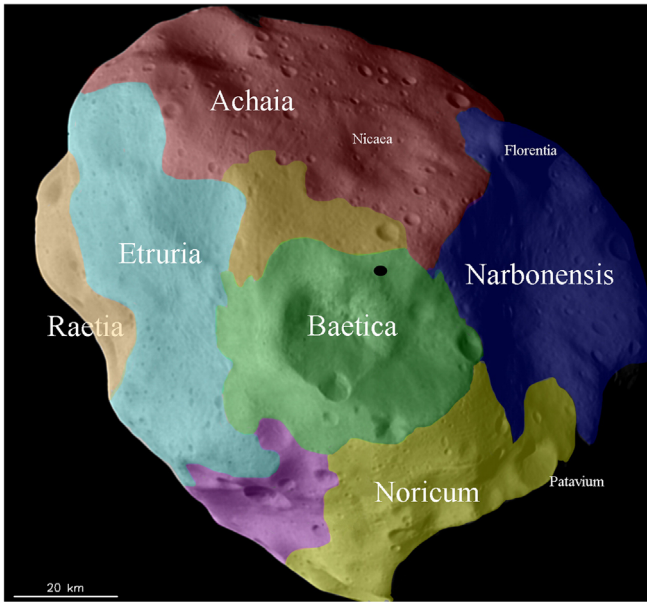
Figure 7. ESA's Rosetta mission observed the M-type asteroid Lutetia during a flyby. The colors represent different regions of Lutetia as defined by geologic mapping. The oldest part of the asteroid, and the one investigated in the paper, is the heavily cratered Achaia region. This image was published in Thomas et al. (2012), who adapted it from Massironi et al. (2012). Copyright Elsevier.

called Achaia (Figure 7). The craters on Achaia range in size from $\sim 1 < D_{crater} < 50$ km (Figure 8), a large-enough dynamic range that they potentially sample both inflection points in our main belt SFD (Figure 1).

5.3.1. Empirical Scaling Law Derived by Fitting Model and Observed Crater SFDs (Achaia)

Our main belt fit method, combined with a P_i value of 3.763×10^{-18} km^{-2} yr^{-1} (Table 3), yields a best fit for SFD #7 with $\chi^2_{MB} = 1.97$ (Table 4). This value is the best of the three scaling laws tested for this case. SFDs #3–#8 also yield results within 1σ of this best-fit case. Our best-fit f value was 10.30 [-4.90, $+3.60$], similar to results from Vesta and Ceres. Our best-fit crater retention age is $T_{ast} = 2.57$ [-2.02, $+1.64$] Ga. This mean value is lower than the ~ 3.6 Ga age estimate from Marchi et al. (2012b) but overlaps within errors. Visually, our main belt fit curve hits both inflection points and is a good visual fit to the data.

5.3.2. Housen & Holsapple Crater Scaling Fit (Achaia)

Using the HH scaling law, the same yield strength as above, P_i and V_{imp} in Table 3, and projectile and target surface densities of 2.5 and 3.0 g cm^{-3}, respectively, we obtain a comparable but slightly worse fit, with $\chi^2_{MA} = 2.24$ for SFD #7. Other SFDs within 1σ of the best-fit case are #5–8. The crater retention age from this fit is $T_{ast} = 3.07$ [-0.41, $+0.41$] Ga, similar to the age found in Marchi et al. (2012b). The empirical main belt and HH crater scaling curves in Figure 8 are fairly similar to one another. The difference in age is produced by modest differences in the f function, with the HH scaling curve having f values between 7 and 9, somewhat lower than the main belt fit of $f \sim 10$.
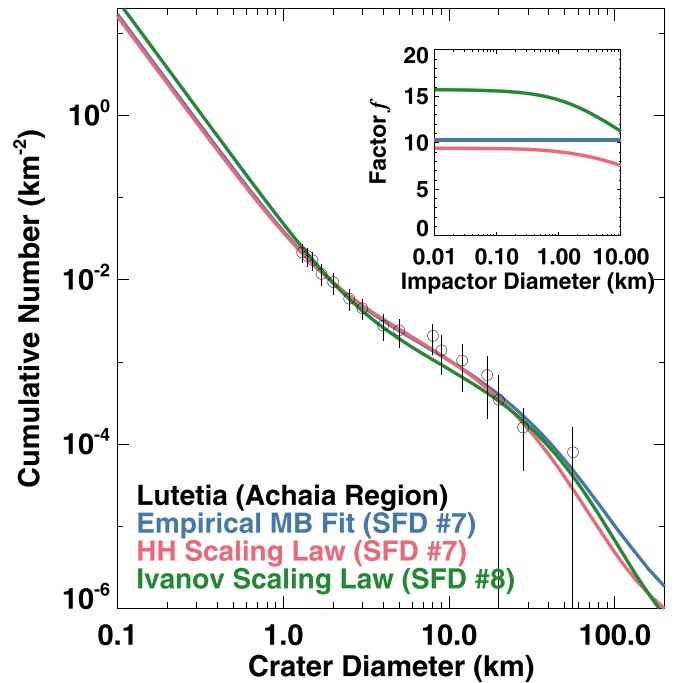

Figure 8. A comparison between the observed crater SFDs found on the Achaia region of Lutetia and various crater models. The observed crater counts are from Marchi et al. (2012b). Plot components are as in Figure 4. The best-fit model crater SFD is the empirical main belt fit and the HH scaling law (Table 3), both of which have f values near 9 or 10 for the majority of observed craters. The predicted mean age of the Achaia region from the empirical main belt fit and HH scaling law model is ~ 2.5–3.5 Ga.

5.3.3. Ivanov Scaling Law Fit (Achaia)

The Ivanov scaling law produces the poorest fit, with $\chi^2_{IV} = 4.00$ for SFD #8 (Table 4). As with the Rheasilvia region on Vesta, the typical f value near 15 for smaller projectiles is higher than those found for either of the other two scaling laws (Figure 8). This large value causes the best-fit case to undershoot crater data between $3 < D_{crater} < 15$ km. It also leads to a younger age for Achaia, with $T_{ast} = 1.24$ [-0.16, $+0.16$] Ga.

Schmedemann et al. (2014) report that their fit to Lutetia's large and degraded craters, which have diameters between 2 and 25 km, yields a crater retention age of 3.5 ± 0.1 Ga. We suspect that the difference in age between the two calculations is caused by our use of craters between 1 and 3 km in Figure 8. These craters drive our fit. If small craters were ignored, the best fit for the Ivanov scaling law curve would slide upward, which in turn would correspond to an older age.

5.3.4. Summary (Achaia)

In all three cases, the best-fit matches seem to come from high-number SFDs, a common theme for all of the crater SFDs discussed up to this point. The main belt fit with $f \sim 10$ and the HH scaling law fit are preferred from the chi-squared metric over the Ivanov scaling law fit, probably because the latter's model crater SFD is lower than the observed crater data for middle-sized craters in Figure 8. The crater retention age of the Achaia region has a wide range of possible ages, but a reasonable value for this terrain is ~ 3–4 Ga.
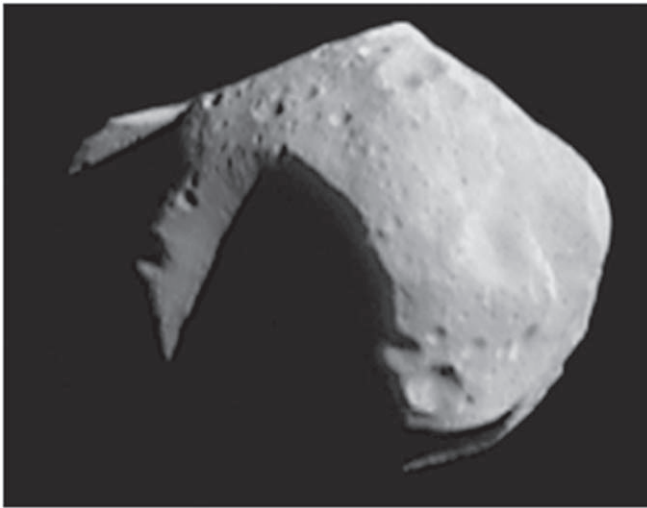
Figure 9. Mathilde is a large C-type main belt asteroid. The part of the asteroid shown is 59 by 47 km across. It was imaged by the NEAR spacecraft from a distance of 2400 km. The surface exhibits many large craters, some of which are partially shadowed. Courtesy of NASA/JPL/JHUAPL.

5.4. Mathilde

(253) Mathilde was the first C-type asteroid imaged by spacecraft (Figure 9). NASA's Near Earth Asteroid Rendez-vous—Shoemaker mission (NEAR) flew by it in 1997 en route to Eros. It is located in the middle of the central main belt, with proper orbital elements of $(a, e, i) = (2.65$ au, $0.22, 6°.5)$. Its physical dimensions are $66\,km \times 48\,km \times 46\,km$, and it has an estimated bulk density of $1.3 \pm 0.2\,g\,cm^{-3}$ (Veverka et al. 1997, 1999). Mathilde is not in an asteroid family (Nesvorný et al. 2015), and thus, its surface may have borne witness to the early days of main belt history.

Mathilde, Bennu, and Ryugu are all C-complex bodies and thus are thought to have physical properties similar to carbonaceous chondrite meteorites. Accordingly, the crater history of Mathilde may provide us with the most direct insights into the crater scaling laws that govern Bennu and Ryugu. There are different schools of thought about how cratering should work on Mathilde. The flyby images that we have of Mathilde are dominated by its two largest craters, Ishikari (29.3 km) and Karoo (33.4 km; Figure 9). There appears to be little ejecta surrounding these craters (Chapman et al. 1999; Veverka et al. 1999). Housen et al. (1999) suggested that the apparent absence of deep ejecta blankets indicates the cratering process is dominated by the effects of porous materials. In such media, craters form more by compaction than excavation, and what little ejecta is produced goes back into the central cavity (Housen & Holsapple 2003; Housen et al. 2018).

The final size of the crater made into such a target, however, is unclear. Kinetic impact energy transfer can be inefficient in a porous target, and this may result in craters that are not much larger than those formed in targets with large yield stresses. Alternatively, the low strength nature of the target may make it easy for an impact to push material out of the way (e.g., comparable to impacts onto sand targets; O'Brien et al. 2006), and this could result in larger craters per projectile diameter than those found on S-type asteroids.

To glean insights into this issue, it is useful to examine Mathilde's crater SFD. Here we adopt the cumulative crater
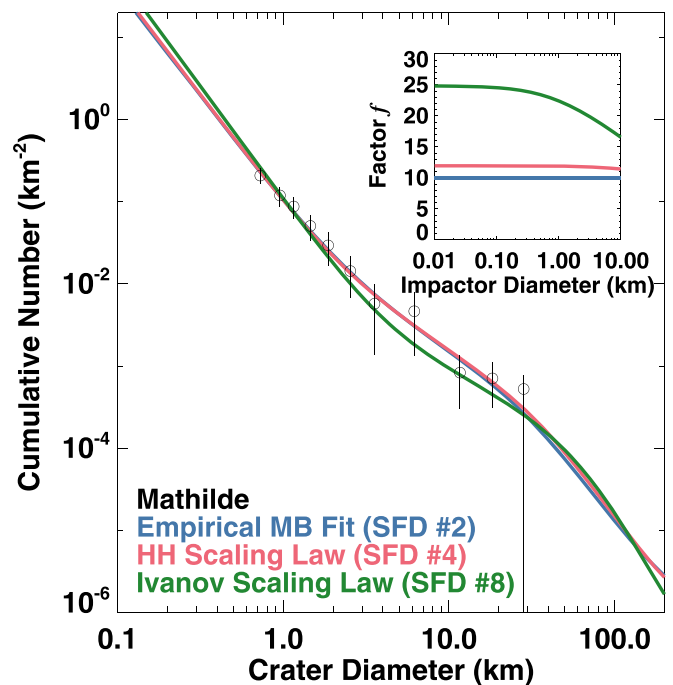

Figure 10. A comparison between the observed crater SFDs found on the C-type asteroid Mathilde and various crater models. The observed crater counts are from O'Brien et al. (2006), who reformulated them from Chapman et al. (1999). Plot components are as in Figure 4. The HH crater scaling law fit in red largely overlaps the main belt empirical fit in blue. The best-fit model crater SFDs are the empirical main belt fit and the HH scaling law (Table 3). They both yield f values near 10–12 for the majority of observed craters and crater retention ages of ∼2 to >4 Ga. Many other SFDs fit the data within 1σ of the best-fit cases (Table 3). If we apply higher-number SFDs to make our model crater SFD, the crater retention ages derived from the empirical main belt fit and the HH scaling law approach the age of the solar system.

counts and errors of O'Brien et al. (2006), who converted their data from Figure 3 of Chapman et al. (1999; Figure 10). Given how far crater counting tools have advanced in two decades, Mathilde would seem to be a ripe target for a reexamination.

It is plausible that the Mathilde data are in saturation at smaller crater sizes, as suggested by Chapman et al. (1999), but the cumulative power-law slope of the data for $D_{crater} < 2\,km$ is close to $q = -2.6$, like those of the Rheasilvia basin (Vesta) and the Achaia region (Lutetia) (Figures 4, 8). Our expectation is that a crater SFD in saturation would instead have a cumulative slope of $q = -2$ (e.g., Melosh 1989), a value that is possible within error bars but does not appear to be the true solution. Here, we will assume that Mathilde's observed crater SFD is not in saturation.

A relatively recent calculation of the crater retention age of Mathilde was made by O'Brien et al. (2006). They made the following assumptions: (i) the intrinsic collision probability P_i for Mathilde was $2.86 \times 10^{-18}\,km^{-2}\,yr^{-1}$ (a factor of 0.77 lower than our value from Table 3), (ii) the main belt SFD followed the estimate made by O'Brien & Greenberg (2005), (iii) Mathilde's craters could be produced by the Pi-group crater scaling relationship, provided that the target acted like loose sand, and (iv) sandblasting by small impactors, a potential crater erasure mechanism, was active on Mathilde (e.g., Greenberg et al. 1994, 1996). Their crater scaling law for Mathilde is shown in their Figure 2. For their impactors of 0.1 to 1 km diameter, their value for f was approximately 20–40.

O'Brien et al. (2006) report that the population of kilometer-scale and smaller craters becomes saturated at a constant level

near 1 Ga ago, but that the best crater retention age for the large craters is ~4 Ga. We will instead assume below that Mathilde's crater SFD follows a production population and that crater erasure mechanisms are not needed to explain observations.

5.4.1. Empirical Scaling Law Derived by Fitting Model and Observed Crater SFDs (Mathilde)

Assuming $P_i = 3.723 \times 10^{-18} \, \mathrm{km}^{-2} \, \mathrm{yr}^{-1}$ (Table 3), we obtain a best fit for SFD #2 with $\chi^2_{MB} = 2.67$ (Table 4). We find that SFDs #1–6 all have χ^2_{MB} within 1σ of this best-fit case. Our best-fit value for f is 10.00 [−3.40, +1.90], and best-fit crater retention age was $T_{ast} = 3.70$ [−1.30, +1.52]. If we were to adopt SFD #6, these values change to $f = 12.2$ [−2.0, +2.3], with T_{ast} becoming 3.61 [−1.31, +0.94] Ga. Here, the smaller number of projectiles in SFD #6 is compensated by having each projectile make a modestly larger crater.

5.4.2. Housen & Holsapple Crater Scaling Fit (Mathilde)

The parameters listed in Holsapple & Housen (2007) for the highly porous case are essentially the same as those used for cohesive soils. It is argued in their paper that their experimental craters were governed predominantly by some compressive strength, so strength-scaled laws would apply. Accordingly, their scaling is almost identical to that used for other asteroids and assumes that compressive strength is the relevant measure.

Assuming a target density of $1.3 \, \mathrm{g \, cm}^{-3}$, we obtain a best fit of $\chi^2_{MA} = 2.60$ for SFD #4. The f value of the scaling law is close to $f = 12$ for the projectile sizes used here (Figure 10). SFDs #1–#5 are 1σ of the best-fit case, and they yield ages of $2.2 < T_{ast} < 3.4$ Ga. If we include error bars, the age range expands to $1.8 < T_{ast} < 4$ Ga.

5.4.3. Ivanov Scaling Law Fit (Mathilde)

The Ivanov scaling law leads to a best fit of $\chi^2_{IV} = 4.98$ for SFD #8 (Table 4). Its f values are substantially higher than the other two cases, and they yield a crater retention age of $T_{ast} = 0.85$ [−0.15, +0.15] Ga. This outcome shows the implications of having projectiles make much larger craters on Mathilde relative to other scaling laws; the surface age of the body becomes young enough that one needs to invoke a special event to explain why the surface is young. As stated above, Mathilde has no asteroid family, and its big craters formed apparently without damaging one another. This makes it more difficult to argue that impacts have reset the surface relatively recently (i.e., over the past billion years).

5.4.4. Summary (Mathilde)

The crater SFD for Mathilde is murky enough that it is difficult to identify which fits are best. Until stronger evidence becomes available, it seems reasonable to adopt the simplest solutions.

Accordingly, if we apply a high-number SFD to our crater model, one that also provides a good fit to the other asteroid terrains investigated so far (i.e., SFD #6, which for Mathilde yields results that are within 1σ of the best-fit case for both the empirical main belt fit case and the HH scaling law case), our results suggest that $f \sim 10$–12 provides a good solution to the entire crater SFD. In turn, those results suggest that Mathilde's

crater retention ages go back to the earliest days of solar system history. Arguments in favor of this interpretation come from Mathilde's lack of an asteroid family. Some might argue that the porous nature of C-type asteroids makes them less likely to produce families, but numerous C-type families have been identified across the main belt (e.g., Masiero et al. 2015; Nesvorný et al. 2015), including those likely to have produced Bennu and Ryugu (Bottke et al. 2015b).

If our interpretation is valid, it obviates the need for crater erasure mechanisms that affect the observed craters smaller than several kilometers (e.g., O'Brien et al. 2006). It would also argue that projectiles hitting carbonaceous chondrite-like materials do not necessarily lead to substantially larger craters than those made on other asteroids (e.g., Ceres craters; see Section 3.2). If Mathilde's crater scaling laws produced $f \gg 10$, it would lead to a crater retention age for Mathilde that would be younger than ~1 Ga. Given the lack of evidence on Mathilde for any surface reset event, we argue that a young crater retention age for Mathilde seems unlikely.

5.5. Ida

The second asteroid observed by the Galileo spacecraft was (243) Ida, an S-type asteroid that is also a member of the Koronis asteroid family (Figure 11). It is located in the outer main belt, with proper orbital elements of $(a, e, i) = (2.86 \, \mathrm{au}, 0.05, 2°.1)$. Its physical dimensions are $59.8 \, \mathrm{km} \times 25.4 \, \mathrm{km} \times 18.6 \, \mathrm{km}$ (Belton et al. 1996). The best estimate of Ida's bulk density comes from Petit et al. (1997), who used the orbit of Ida's satellite Dactyl to obtain a value of $2.6 \pm 0.5 \, \mathrm{g \, cm}^{-3}$.

The age of the Koronis family, and likely that of Ida, can be computed using dynamical models. By tracking how Koronis family members have drifted in semimajor axis by the combined Yarkovsky and YORP effects, it has been estimated that the family's age is ~2–3 Ga (Bottke et al. 2001; Brož et al. 2013; Spoto et al. 2015; see also Nesvorný et al. 2015). Error bars on this value could take it to 4 Gyr as well.

There are also multiple Koronis family members (including Ida) whose spin vectors have been modified enough by the YORP effect, some to be caught in spin–orbit resonances (Vokrouhlický et al. 2003). Large family members with prograde spins in so-called "Slivan states" have nearly identical periods (7.5–9.5 hr), obliquities between $42°$ and $50°$, and pole longitudes confined in a tight interval between $25°$ and $75°$. Vokrouhlický et al. (2003) estimated that the time needed for the observed bodies with $20 < D_{ast} < 40 \, \mathrm{km}$, starting with spin periods $P = 5$ hours, to reach their Slivan state status was ~2–3 Ga. Accordingly, our expectation is that Ida's crater retention age should be close to this value.

Modeling Ida's crater history is challenging because many smaller crater sizes appear to be near or in saturation equilibrium (Chapman et al. 1996a reviewed in Chapman 2002 and Marchi et al. 2015). There are ways to deal with crater saturation using specialized codes (e.g., Marchi et al. 2012a), but they also involve making assumptions about the nature of the saturation process; this issue will be discussed in a follow-up paper.

As a work-around, we examine the crater counts provided by Figure 5 of Chapman et al. (1996a; Figure 12). Their crater SFD between $0.6 < D_{crater} < 10 \, \mathrm{km}$ has a similar shape to those seen on Vesta and Lutetia for the same size range (Figures 4 and 8). Only the craters with $D_{crater} < 0.6 \, \mathrm{km}$ seem

Figure 11. Ida and Gaspra to the same scale. Gaspra (right) was imaged at a range of 5300 km, and Ida (left) was imaged from 3000 to 3800 km, both by the Galileo spacecraft. Gaspra's dimensions are 18.2 km × 10.5 km × 8.9 km, and Ida's are 59.8 km × 25.4 km × 18.6 km (Belton et al. 1992, 1996). Both bodies are S-type asteroids that are members of asteroid families: Gaspra is part of the Flora family, which may be 1.3 Ga old, and Ida is part of the Koronis family, which is 2–3 Ga old (Bottke et al. 2001; Vokrouhlický et al. 2003, 2017; Brož et al. 2013; Nesvorný et al. 2015; Spoto et al. 2015). Courtesy of NASA/JPL/USGS.
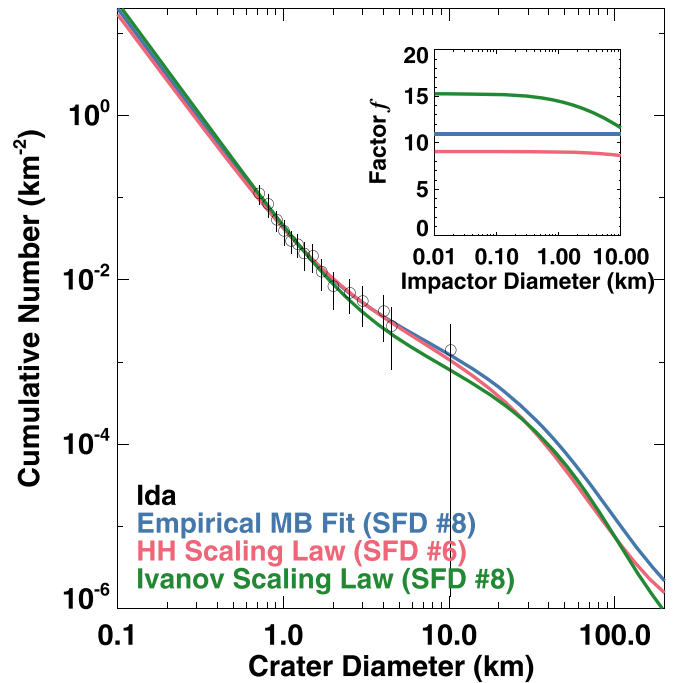

Figure 12. A comparison between the observed crater SFDs found on the S-type asteroid Ida, a member of the Koronis family, and various crater models. The observed crater counts are from Figure 5 of Chapman et al. (1996). Plot components are as in Figure 4. The best-fit model crater SFD is the empirical main belt fit, but both the HH scaling law and the Ivanov scaling law yield comparable fits (Table 3). The empirical main belt fit scaling law and the HH scaling law are our preferred solutions, with the inset showing that both have $f \sim 9$–11.

to have the -2 cumulative power-law diagnostic of saturation (e.g., Melosh 1989; see also Marchi et al. 2012a). Our main belt model will be applied to Ida's craters with $D_{crater} > 0.6$ km.

5.5.1. Empirical Scaling Law Derived by Fitting Model and Observed Crater SFDs (Ida)

Using a P_i value of 4.037×10^{-18} km^{-2} yr^{-1} (Table 3), we obtain a best fit for SFD #8 with $\chi^2_{MB} = 1.17$ (Table 4). All of the other SFDs also fit within 1σ of this best-fit case, a byproduct of the limited number of large craters in our crater SFD. As in the case for Lutetia's Achaia region, the empirical main belt fit case is the best of the three scaling laws tested.

Our best-fit f value is 10.90 [-2.70, $+2.90$], and our best-fit crater retention age is $T_{ast} = 2.52$ [-1.98, $+0.94$] Ga. The f value is similar to our results in previous runs, not a surprise given the location of the knee in Ida's crater SFD at $D_{crater} \sim 2$ km. If we apply a more probable main belt SFD, such as SFD #6 (Table 1), the best-fit f value moves to 10.00 [-3.40, $+3.00$], and our best-fit crater retention age is $T_{ast} = 2.36$ [-2.36, $+2.37$] Ga. The lower error bar is a formal number and should not be taken literally. Both crater retention ages for Ida are consistent with the estimated dynamical ages of the Koronis family. Visually, our main belt fit curve hits both inflection points and provides a good visual match to the data.

5.5.2. Housen & Holsapple Crater Scaling Fit (Ida)

For the HH scaling law case, we applied the same yield strength as before, P_i and V_{imp} values from Table 3, and projectile and target surface densities of 2.5 and 2.6 g cm^{-3}, respectively. Our best-fit case was for SFD #6, which yielded $\chi^2_{MA} = 1.39$ (Table 4). As in the empirical main belt fit case, all SFDs are within 1σ of the best-fit case. The crater retention age from our best fit is $T_{ast} = 2.91$ [-0.43, $+0.43$] Ga, which again is a reasonable match with the dynamical age of the

Koronis family. The f functions for this scaling law are slightly lower than the main belt fit, but this is balanced against a different best-fit choice for the main belt SFD.

5.5.3. Ivanov Scaling Law Fit (Ida)

The Ivanov scaling law yields a best fit of $\chi^2_{IV} = 1.93$ for SFD #8, which is within 1σ of the other two scaling laws (Table 4). It produces f values near 15 for smaller projectiles, though, and this leads to a crater retention age of $T_{ast} = 1.17$ [-0.17, $+0.16$] Ga, much younger than from the other scaling laws. This value is outside the range estimated from dynamical models for the age of the Koronis family, though see the caveats discussed earlier in this section.

Schmedemann et al. (2014) applied the Ivanov scaling law model and a main belt SFD similar to SFD #8 to crater counts found over a limited region of Ida. They assumed that the P_i value for the impactors was 3.6×10^{-18} km^{-2} yr^{-1}, while their impact velocities were 3.3 km s^{-1}. Both values are about 90% of our values in Table 3. In this region, crater spatial densities were found to be roughly a factor of 2 higher than those in Chapman et al. (1996a; Figure 12). Their best fit to these craters, most of which were between 1 and 2 km in diameter, yielded an age of 3.4–3.6 Ga. Other surfaces with fresher craters suggested ages of ~2.1 Ga when their model was fit to data from craters between 0.5 and 1 km in diameter.

5.5.4. Summary (Ida)

The main belt fit scaling law with $f \sim 10$, along with the HH scaling law, is our preferred solution, with main belt SFD solutions within high numbers favored from our fits. They

produce mean crater retention ages of Ida near 2.5–2.9 Ga. These values are consistent with the model-derived dynamical age of the Koronis family, with Ida as a family member. The saturated crater regions on Ida do exist, however, and they could suggest an age for Ida older than 3 Ga. This would be tolerable given errors on existing family and dynamical constraints.

5.6. Gaspra

(951) Gaspra was the first asteroid ever observed by spacecraft (Figure 11). The data returned by NASA's Galileo flyby in 1991 provided scientists with their first glimpse of what an S-type asteroid look likes up close. Gaspra has dimensions of 18.2 km × 10.5 km × 8.9 km and a mean diameter of 12.2 km (Thomas et al. 1994). It is a prominent member of the Flora family that dominates the innermost region of the main asteroid belt (Nesvorný et al. 2015). The proper orbital elements of Gaspra are $(a, e, i) = $ (2.21 au, 0.15, 5°1).

Constraints on the age of Gaspra can be inferred from the evolution of the Flora family, which was formed from the catastrophic disruption of an asteroid of $D_{\mathrm{ast}} > 150$ km in the orbital region adjacent to the ν_6 secular resonance (Durda et al. 2007; Vokrouhlický et al. 2017). Vokrouhlický et al. (2017) used collisional and dynamical models to track the evolution of Flora family members immediately after the family-forming event. They found that test Flora family members can reproduce the observed semimajor axis, eccentricity, and inclination distributions of the real family after 1.35 ± 0.3 Ga of evolution, assuming that family members have bulk densities near 2.70 ± 0.54 g cm^{-3} (e.g., Scheeres et al. 2015 see also Dykhuis et al. 2014).

This dynamical age is consistent with the ^{40}Ar/^{39}Ar ages of LL chondrite grains returned from (25143) Itokawa by the Hayabusa spacecraft: 1.3 ± 0.3 Ga (Nakamura et al. 2011; Park et al. 2015; see also Terada et al. 2018). Flora family members have spectra consistent with those of LL-type chondrites (Vernazza et al. 2008; de León et al. 2010; Dunn et al. 2013), and dynamical models indicate that Flora is perhaps the most probable source for Itokawa (Bottke et al. 2002; Granvik et al. 2016, 2018). We will discuss Itokawa in more detail below, but the correspondence of these ages suggests that Gaspra should likely have a crater retention age comparable to 1.3 ± 0.3 Ga. In our modeling work below, we assign Gaspra a bulk density of 2.7 g cm^{-3}.

The population of Gaspra's craters has been reported and modeled by several groups (e.g., Belton et al. 1992; Greenberg et al. 1994; Chapman et al. 1996b; Chapman 2002; O'Brien et al. 2006; Marchi et al. 2015). Numerous craters were identified between $0.16 < D_{\mathrm{crater}} < 1.9$ km that followed a cumulative power-law slope of −2.6. This size limit means Gaspra does not sample the knee in the crater SFDs observed near $D_{\mathrm{crater}} \sim 2$ km on Vesta, Lutetia, Ida, and others. A possible exception may be the mysterious facets on Gaspra, one or more of which may be ancient craters with $D_{\mathrm{crater}} > 2$ km (e.g., Greenberg et al. 1994; Thomas et al. 1994; O'Brien et al. 2006). None of these pseudo-craters has been verified, so we do not include them in our analysis.

More recently, Gaspra's crater SFD was reassessed using the Small Body Mapping Tool (SBMT; Runyon & Barnouin 2015; Ernst et al. 2018). The SBMT allows images to be wrapped onto an asteroid shape model, which is helpful for calculating
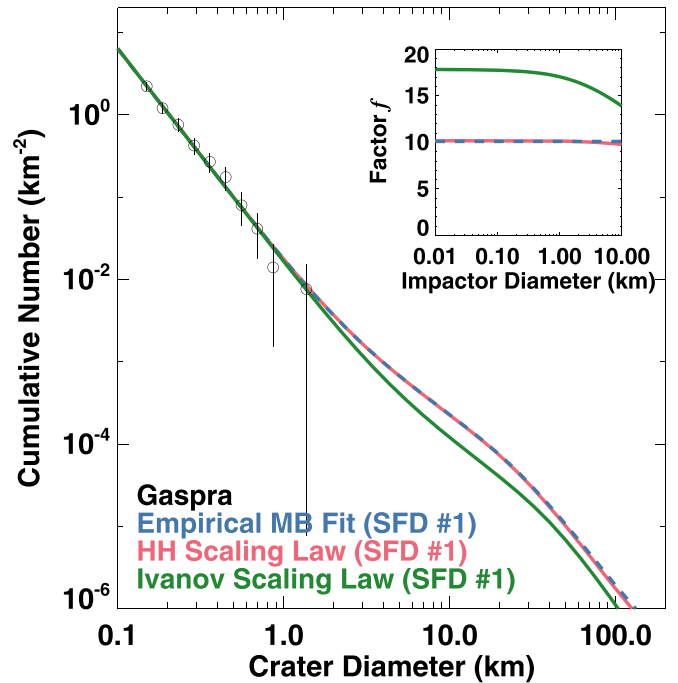

Figure 13. A comparison between the observed crater SFDs found on the S-type asteroid Gaspra, a member of the Flora family, and various crater models. The observed crater counts are from Runyon & Barnouin (2015). Plot components are as in Figure 4. The HH crater scaling law fit in red overlaps the main belt empirical fit in blue. All of our best-fit models favor SFD #1 (Table 3), but all yield crater retention ages that are substantially lower than the age constraints from the Itokawa samples and our estimated dynamical age of the Flora family. We prefer SFD #5 or #6, which yields results within 1σ of the best-fit case, yet yields mean crater retention ages between ∼1.1 and ∼1.4 Ga, values that are close to Gaspra's estimated age of 1.35 ± 0.3 Ga from additional constraints (Figure 18). For these latter runs, our preferred value of f is ∼10.

surface areas when the body is irregular. They counted 712 craters of $0.05 < D_{\mathrm{crater}} < 1.3$ km within an area of 119.6 km^2 (Figure 13). A rollover in their counts occurs for $D_{\mathrm{crater}} < 0.17$ km, which they attribute to limitations of image resolution. Overall, the shape of their crater SFD was similar to that of Chapman et al. (1996b), with the power-law slope of −2.6 reproduced. The normalization of the counts, however, was lower, probably because SBMT can more easily derive the irregular area of Gaspra's observed surface. In our modeling work, we use these new counts for Gaspra.

5.6.1. Empirical Scaling Law Derived by Fitting Model and Observed Crater SFDs (Gaspra)

Assuming $P_i = 2.635 \times 10^{-18}$ km^{-2} yr^{-1} (Table 3), we obtain a best fit for SFD #1 with $\chi^2_{\mathrm{MB}} = 1.94$ (Table 4). Although this fit appears to favor lower-number SFDs, the other SFDs all have χ^2_{MB} within 1σ of this best-fit case. The reason for this behavior is that Gaspra's observed crater SFD is effectively a power law, which is relatively easy for most models to fit. All of the main belt SFDs from Figure 1 show power-law slopes of $q \sim -2.6$ cumulative for their smallest craters, which matches the slope of Gaspra's craters (Chapman et al. 1996b).

Our best-fit crater retention age for SFD #1 was $T_{\mathrm{ast}} = 0.74$ [−1.71, +0.41] Ga, nearly a factor of 2 lower than Gaspra's expected age from constraints. Negative ages when the error

bars are included are not meant to be taken literally. Given the similarity of our results for the different SFDs, the fact that the other asteroids favor high-number SFDs, and that Table 1 favors SFDs #5 and #6, we find it interesting that our model results for SFDs #5 and #6 yield mean ages between $1.18 < T_{ast} < 1.38$ Ga, all very close to our constrained age for Gaspra of 1.35 ± 0.3 Ga. For these latter runs, our preferred value of f is 10.

5.6.2. Housen & Holsapple Crater Scaling Fit (Gaspra)

Using the Holsapple & Housen (2007) scaling law and the same input parameters as Ida, expect for gravity, we obtain a best fit of $\chi^2_{MA} = 1.93$ for SFD #1. As before, all SFDs are within 1σ of the best-fit case, with SFDs #5 and #6 yielding mean ages of $1.12 < T_{ast} < 1.32$ Ga and a spread of $1.01 < T_{ast} < 1.46$ Ga when errors are included. The f value of the scaling law is near identical to the main belt fit's estimate of $f = 10$.

5.6.3. Ivanov Scaling Law Fit (Gaspra)

The Ivanov scaling law provides the best fit of the three cases, with $\chi^2_{IV} = 1.85$ for SFD #1 (Table 4). Here SFDs #2–#8 are within 1σ of the best fit. Its higher f values for smaller projectiles, however, yield an age for SFDs #5 and 6 between $0.25 < T_{ast} < 0.29$ Ga. These values are outside our age range derived from Flora and Itokawa constraints.

Schmedemann et al. (2014) applied the Ivanov scaling law model and a main belt SFD similar to SFD #8 to crater counts found over a limited region of Gaspra. They assumed a P_i value for their impactors of 3.54×10^{-18} km^{-2} yr^{-1}, and their impact velocities were 4.69 km s^{-1}. Both values are modestly higher than our values in Table 3. They identified a steep crater SFD similar to that reported in Chapman et al. (1996b) that yielded a crater retention age of 0.27 ± 0.068 Ga. This value is similar to our prediction for the Ivanov scaling law of $0.25 < T_{ast} < 0.29$ Ga.

5.6.4. Summary (Gaspra)

All of our best-fit models favor SFD #1, but the crater retention ages produced by our fits are substantially different from age constraints from Itokawa samples and our estimated dynamical age of the Flora family. We also argue that SFD #1 is largely disfavored according to the crater SFDs of other main belt asteroids. The higher-number SFDs, however, produce results within 1σ of this best-fit case, with our preferred SFDs, namely #5 or #6, producing ages that are a good match to the Gaspra's additional age constraints (approximately 1.3 Ga). If we use those runs, our main belt scaling law fit results yield $f \sim 10$, the same values as for the asteroids discussed above.

5.7. Eros

We are now ready to consider the crater retention age of (433) Eros, the largest NEO observed by spacecraft. It was the primary target of NASA's NEAR mission and has a record of large craters that share commonalities with those of the main belt asteroids investigated above.

Eros has dimensions of 34.4 km × 11.2 km × 11.2 km and a bulk density of 2.67 ± 0.03 g cm^{-3} (Thomas et al. 2002; Figure 14). It is classified as an S-type asteroid, and its spectral characteristics suggest that it is similar to L- or LL-type
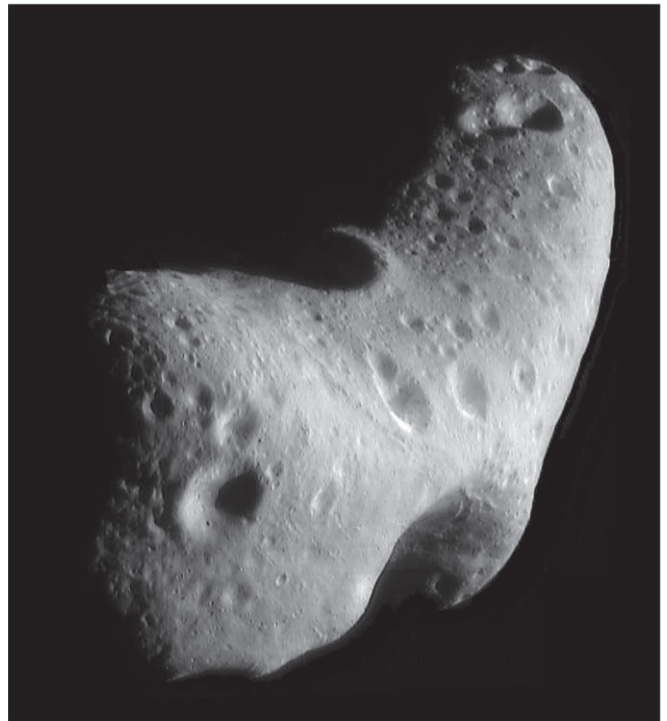

Figure 14. Eros is an S-type near-Earth asteroid. It has dimensions of 34.4 km × 11.2 km × 11.2 km (Thomas et al. 2002). This view of Eros's northern hemisphere is a mosaic of six NEAR spacecraft images taken from an orbital altitude of about 200 km. The Psyche crater (5.3 km across) is located at the 12 o'clock position in the middle of the saddle-shaped region, and the Himeros crater (11 km) can be seen on the opposite side of Eros at the 5 o'clock position. Courtesy NASA/JPL/JHUAPL.

ordinary chondrites (e.g., Trombka et al. 2000; Foley et al. 2006; Dunn et al. 2013; Peplowski et al. 2015; Peplowski 2016). Recent spectral modeling work by Binzel et al. (2019) agrees with this assessment; they find probabilities of 2%, 24%, and 74% that Eros is an H, L, and LL chondrite, respectively. Their interpretation is that Eros is most likely an LL chondrite.

All of these characteristics make Eros something of a mini-Ida. Ida is an S type with a similar bulk density and shape, but it is only half the size (Section 5.5). A difference between the two is Eros's orbit; it currently crosses the orbit of Mars with $(a, e, i) = (1.458$ au, $0.223, 10°83)$. This classifies it as an Amor-type NEO; it cannot currently strike Earth, but its unstable orbit may put it in position to do so in the future (Michel et al. 1996).

Objects as large as Eros have little Yarkovsky mobility (e.g., Bottke et al. 2006b). For Eros-like bodies to escape the main belt and reach an Eros-like orbit, it is helpful if they are initially located in the innermost main belt region. Here, a forest of overlapping Mars and three-body resonances creates a diffusive environment for asteroids (e.g., Morbidelli & Nesvorný 1999; Nesvorný et al. 2002; Nesvorný & Roig 2018). Alternatively, they need to have been created by a large-asteroid disruption event occurring on the brink of a prominent resonance (e.g., Zappalà et al. 1997). Either way, dynamical models suggest that Eros likely spent hundreds of millions of years to many billions of years to escape the main belt. Only the last few millions to tens of millions of Eros's lifetime have been spent on planet-crossing orbits collisionally decoupled from the main belt population (e.g., Bottke et al. 1996, 2002). Based on this,

we predict that most craters on Eros were derived from main belt impactors and that we can model Eros's cratering history in the same manner as the main belt asteroids discussed above.

According to the NEO model of Granvik et al. (2018), Eros was derived from the Hungaria region (44%), the innermost region of the main belt (47%), or 3:1 resonance (9%). Given that the Hungarias currently have a paucity of Eros-sized S-type asteroids, we can probably reject that region as a source for Eros. Doing so increases the probabilities that Eros came from the innermost main belt and the 3:1 resonance to 84% and 16%, respectively. These results match those of Bottke et al. (2002), whose NEO model did not include the Hungarias; they found that Eros has an 80% chance of coming from the inner main belt and 20% from the 3:1 resonance.

Given that Eros likely has an LL chondrite-like composition, it is natural to once again consider the Flora family as a possible source, especially given our results for Gaspra in Section 5.6. Some have also postulated that Eros may be derived from the Maria asteroid family, which disrupted on the brink of 3:1 resonance with Jupiter (Zappalà et al. 1997, 2001).

Many regions on Eros appear to be close to crater saturation, with only the largest craters escaping this fate (Chapman 2002; Robinson et al. 2002). The full database of Eros craters was provided to us by P. Thomas, who did the original mapping of Eros with M. Berthoud. The database is only likely to be complete for $D_{crater} > 0.2$ km (P. Thomas 2020, personal communication). We estimate that the onset of saturation equilibrium takes place for $D_{crater} < 0.6$ km, as determined when the power-law slope of the craters at small sizes moves to a $q = -2$ cumulative index value. For this reason, as with Ida, we will only examine the craters of $D_{crater} > 0.6$ km (Figure 15).

As an aside, we point out that seismic shaking appears to have reduced the spatial density of craters with $0.2 < D_{crater} < 0.5$ km from the vicinity of the 7.6 km Shoemaker crater (Thomas & Robinson 2005), and that some mechanism —perhaps impact-induced seismic shaking—also erased craters with $D_{crater} < 0.1$ km (Richardson et al. 2004). The issue of small crater erasure on asteroids is a fascinating one, but work on this topic is beyond the scope of this paper.

5.7.1. Empirical Scaling Law Derived by Fitting Model and Observed Crater SFDs (Eros)

Given our limited information on the origin of Eros, we assume for now that Eros's original orbit was in the Flora asteroid family within the inner main belt. Accordingly, we assign it a starting orbit similar to Gaspra and give it a P_i value of 2.635×10^{-18} km^{-2} yr^{-1} (Table 3). Our results indicate that we obtain our best fit using SFD #2, yielding $\chi^2_{MB} = 3.72$ (Table 4). All of the other SFDs also fit within 1σ of this best-fit case. Our best-fit f value was 10.90 [-3.00, $+3.00$], and our best- fit crater retention age is $T_{ast} = 2.03$ [-2.01, $+0.86$] Ga. If we were to instead adopt SFD #5 and #6, these mean values would change to $f = 11.90$–12.20 and $T_{ast} = 2.32$–2.55 Ga.

5.7.2. Housen & Holsapple Crater Scaling Fit (Eros)

Using the HH scaling law, a target density of 2.67 g cm^{-3}, and the same input parameters as for Gaspra and Ida, except for gravity, we obtain a best fit of $\chi^2_{MA} = 3.85$ for SFD #1. SFDs #2–#7 are within 1σ of the best-fit case. Collectively, they
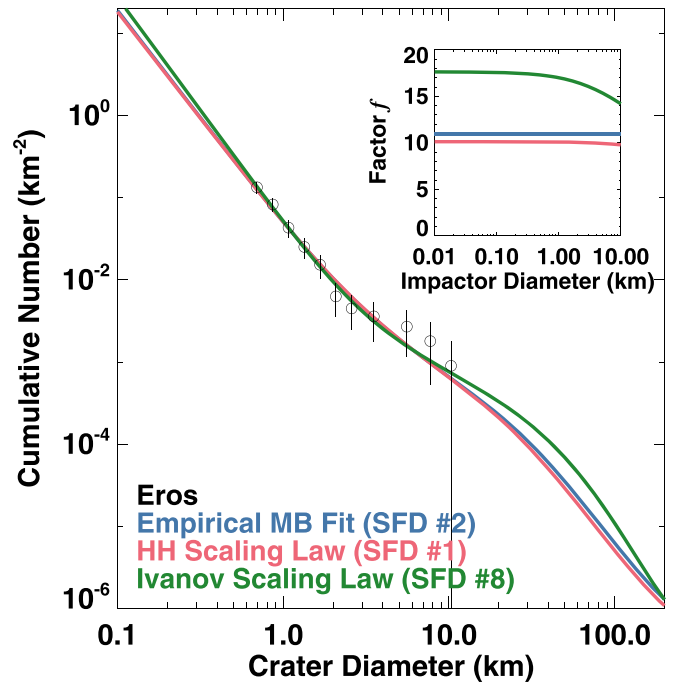

Figure 15. A comparison between the observed crater SFDs found on the S-type asteroid Eros, a near-Earth asteroid, and in various crater models. The observed crater counts are from P. Thomas and are discussed in Robinson et al. (2002). Craters that are in probable saturation (i.e., those with $D_{crater} < 0.6$ km) are not shown. Plot components are as in Figure 4. The HH crater scaling law fit in red largely overlaps the main belt empirical fit in blue. The best-fit model crater SFD here is the Ivanov scaling law fit, though all of the fits are fairly comparable (Table 3). See text for discussion of the crater retention age of Eros and possible source families.

yield mean ages between $2.1 < T_{ast} < 4.5$ Ga. The typical f values of this scaling law are close to $f \sim 10$ for the projectile sizes used here (Figure 15). For SFDs #5 and #6, the mean ages are between $3.34 < T_{ast} < 3.81$ Ga.

5.7.3. Ivanov Scaling Law Fit (Eros)

The Ivanov scaling law provides the best fit of the three cases, with $\chi^2_{IV} = 2.27$ for SFD #8 (Table 4). Its higher f values yield an age of $T_{ast} = 1.4$ [-0.19, $+0.18$] Ga (Table 5).

5.7.4. Interpretation of Eros's Crater Record

Our best-fit mean crater retention ages from the main belt fit and the Marchi scaling law results are between 2.3 and 3.8 Ga. These values are substantially older than the estimated age of the Flora family (i.e., 1.35 ± 0.3 Ga; Section 5.6). One could dispute this, given that the best-fit Ivanov scaling law's crater retention age is $T_{ast} = 1.4$ [-0.19, $+0.18$] Ga. The counter-arguments are that Eros has notably higher crater spatial densities than Gaspra for similar-sized craters and Gaspra is a Flora family member (Figures 13 and 15). Accordingly, we rule out Eros as a Flora family member on this basis.

It has also been postulated that Eros could come from the Maria family, located adjacent to the J3:1 resonance at high inclinations (Zappalà et al. 1997, 2001). As reported above, the odds of asteroids from J3:1 reaching an Eros-like orbit are $\sim$20%, less likely than the inner main belt but not unreasonably low. Several published dynamical ages for the Maria family have suggested that it is $\sim$2 Ga (e.g., Spoto et al. 2015;

Aljbaae et al. 2017) or possibly 3 ± 1 Ga (Brož et al. 2013). The collision probability of main belt asteroids with (170) Maria is $P_i = 2.923 \times 10^{-18}\,\mathrm{km}^{-2}\,\mathrm{yr}^{-1}$, about 1.1 times the value used for the above age calculation. Multiplying our ages by this factor gives 2.2–4.1 Ga. These crater retention ages are in the same ballpark as the dynamical age estimates for Maria, given uncertainties.

The problem is that the Binzel et al. (2019) spectral model predicts that (170) Maria has probabilities of 75%, 23%, and 2% of being an H, L, and LL chondrite, respectively. Given that Eros is likely an LL chondrite, it would appear that Maria can be ruled out as a candidate family on the basis of its spectral signature.

Accordingly, at this time, we have no independent constraints on the age of Eros. Given the comparable qualities of the fits in Figure 15, we cannot use its crater SFD as a measure of which crater scaling law is preferred.

With that said, our crater studies above indicate that the empirical main belt and HH scaling law fits are preferred over the Ivanov scaling law fit. This suggests that the most likely scenario is that Eros was formed from the breakup of an asteroid in the inner main belt ~2.3–3.8 Ga ago. The family has yet to be identified. If Eros came from a parent body that disrupted in the inner main belt, the reason that the family has not been found is plausibly because it disrupted in a highly diffusive region of this zone. Given the complicated network of resonances that exist in the inner main belt, we find it interesting but perhaps not surprising that an Eros precursor might avoid leaving behind clues to its existence after such a long time period. Less likely but still possible is that Eros came from the breakup of a body near the 3:1 resonance or from the Hungaria asteroid region. Additional work on this issue is warranted.

6. Near-Earth Asteroids Smaller than 10 km

Armed with the insights gleaned from Section 3, we now consider the crater retention ages of smaller NEOs observed by spacecraft: (25143) Itokawa, (4179) Toutatis, (101955) Bennu, and (162173) Ryugu. It is challenging to model the cratering history of any of these bodies for several reasons.

First, these NEOs have experienced an erasure process that eliminated craters smaller than many tens of meters to possibly up to hundreds of meters. We do not examine erasure mechanisms in this paper, but it has been suggested that impact-induced seismic shaking or perhaps regolith mobility driven by thermal cycling may be responsible for this deficit (e.g., Richardson et al. 2004; Marchi et al. 2015). Accordingly, only the largest craters on NEOs may stretch back to deep time.

To make progress in our work below, we avoid craters that may have been affected by crater erasure mechanisms. We define this as the crater diameter size range on the SFD plots discussed below where the observed and model crater SFDs diverge from one another. For Itokawa, Toutatis, Bennu, and Ryugu, this occurs for crater diameters smaller than ~100 m, ~250 m, ~150 m, and ~70–150 m, respectively.

Second, the dynamical histories of NEOs are uncertain. If we do not know where these asteroids came from in the main belt, it is difficult to predict how their collision probabilities and impact velocities varied with time. To make progress in our work below, we estimate the likely source regions and dynamical pathways followed by the bodies using our

knowledge of main belt families, asteroid spectral signatures, and asteroid dynamics.

Third, as discussed in the introduction, the crater scaling laws that should be employed on asteroids that are a few hundred meters to several kilometers in diameter are uncertain. For the work below, we focus our attention on two possibilities:

1. Option 1. The crater retention ages of small asteroids, based on their largest craters, are long. For NEOs, they potentially provide a record of each world's traverse from their main belt starting orbit to the resonance that pushed them onto a planet-crossing orbit (e.g., Bottke et al. 2002, 2006b). In some cases, they may even reach back to the time of their parent body's disruption event.
2. Option 2. The crater retention ages of small asteroids are short. For NEOs, the largest craters may only tell us about the last part of their journey in the main belt and perhaps the few millions to tens of millions of years it took to obtain their current orbits.

Impact experiments and numerical hydrocode modeling work have suggested that f values for small asteroids could be much higher than those derived from our Section 3 work, with values of 20, 40, or even 100 possible, depending on the physical properties of the target (e.g., Tatsumi & Sugita 2018).

As an example, consider the recent numerical hydrocode impact experiments of Davison et al. (2019). They created a Bennu-like target with a basalt equation of state that was 20% porous and hit it with a 0.7 m diameter projectile at $7\,\mathrm{km\,s}^{-1}$. When the strength of the target was set to 0.1, 1, 10, and 100 kPa, the simulations yielded crater diameters of 37, 22, 14, and 8.9 m, respectively, which translates into f values of 53, 32, 20, and 13, respectively. The unresolved issue is what strength value is appropriate to modeling the largest craters on Bennu.

If the low strength values are correct, Option 2 is preferred and our spacecraft-observed NEOs should have young crater retention ages. Option 2 might even be the expected outcome, given the estimated short timescales needed to spin small asteroids up to mass shedding via YORP.

On the other hand, our modeling results above indicate that $f \sim 10$ values can explain most main belt crater SFDs on $D_{\mathrm{ast}} > 10$ km asteroids (with the possible exception of $D_{\mathrm{crater}} < 2$–3 km craters on Ceres). This suggests that Option 1 may be viable.

It is interesting to consider that craters on Vesta ($D_{\mathrm{ast}} \sim 530$ km) and Gaspra ($D_{\mathrm{ast}} \sim 12$ km) can be fit with $f \sim 10$ for $D_{\mathrm{crater}} > 0.1$–0.2 km, even though they are very different in size (i.e., the ratio of the diameter of Vesta to that of Gaspra is 44). The diameter ratio between Gaspra and our spacecraft-observed NEOs, which are $0.3 < D_{\mathrm{ast}} < 2.5$ km, ranges from 5 to 40. This raises the possibility that the largest NEOs in our Section 4 sample might follow the same trend.

With all of these issues in mind, we start our investigation with Itokawa.

6.1. Itokawa

(25143) Itokawa, an Apollo-type S (IV)-type NEO, was the target of JAXA's Hayabusa mission (Figure 16). Itokawa appears to be a rubble-pile asteroid, with an elongated shape (dimensions of $0.535\,\mathrm{km} \times 0.294\,\mathrm{km} \times 0.209\,\mathrm{km}$) and an estimated bulk density of $1.9 \pm 0.13\,\mathrm{g\,cm}^{-3}$ (Fujiwara et al. 2006). It has two main components covered with rocks and
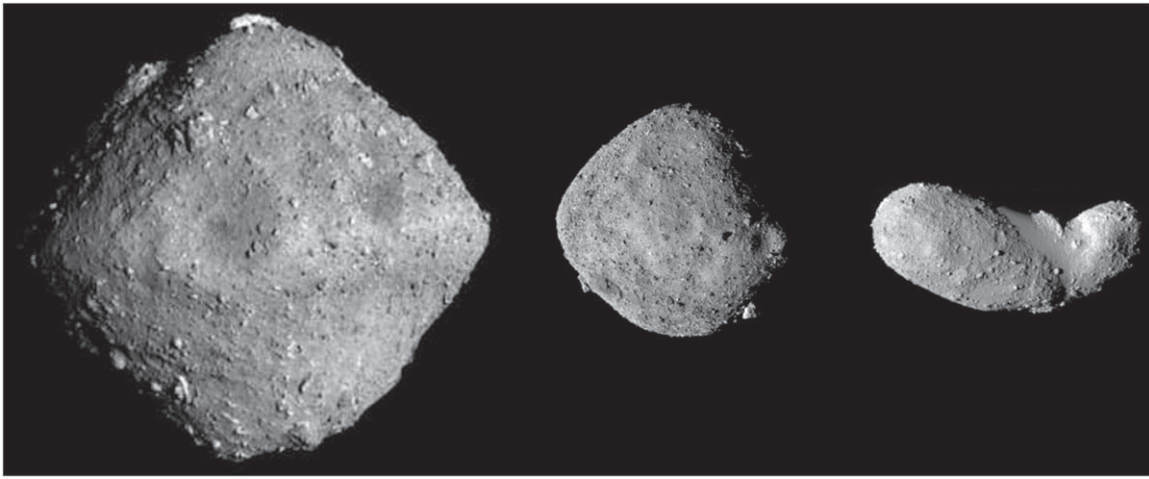
Figure 16. Three near-Earth asteroids observed by spacecraft that are smaller than 1 km. Ryugu (left) is a Cb-type asteroid with a mean diameter of 896 m and a bulk density of 1.19 ± 0.02 g cm^{-3} (Watanabe et al. 2019). Its spectral signatures are consistent with thermally and/or shock-metamorphosed carbonaceous chondrite meteorites (Kitazato et al. 2019). Bennu (center) is a B-type asteroid with a mean diameter of 492 m and a bulk density of 1.190 ± 0.013 g cm^{-3} (Lauretta et al. 2019). Its composition is similar to aqueously altered CM-type carbonaceous chondrites. Itokawa (right) is an S-type asteroid with dimensions of 0.535 km $\times$ 0.294 km $\times$ 0.209 km and an estimated bulk density of 1.9 ± 0.13 g cm^{-3} (Fujiwara et al. 2006). Grains from Itokawa indicate that it has the composition of an LL-type ordinary chondrite. Images courtesy of NASA/JAXA.

boulders, and it seems likely that it was reassembled from debris produced by the disruption of the Itokawa parent body.

Hayabusa rendezvoused with Itokawa in 2005 and returned numerous grains from this body to Earth in 2010. An analysis of Itokawa samples showed this asteroid has a composition similar to LL ordinary chondrites, results that were consistent with its spectroscopic signature (Nakamura et al. 2011). Three grains yield ^{40}Ar/^{39}Ar shock degassing ages of 1.3 ± 0.3 Ga (Park et al. 2015), whereas seven phosphate grains dated using the U–Pb system provide reset ages of 1.51 ± 0.85 Ga (Terada et al. 2018). The interpretation is that a large, possibly catastrophic impact event affected the Itokawa precursor 1.3–1.4 Ga ago.

Dynamically, it can be shown that Itokawa, which currently resides on a fairly Earth-like orbit with $(a, e, i) = (1.324$ au, 0.280, 1°621), most likely came from the innermost region of the main belt. The NEO models of Bottke et al. (2002) and Granvik et al. (2018) suggest that the odds of Itokawa having this provenance are ~86%–100%.

The most prominent S-type family in the inner main belt is Flora, which formed from the catastrophic collision of a parent body larger than 150 km in diameter (e.g., Durda et al. 2007). As discussed in Section 5.6, dynamical models suggest that the age of the Flora family is 1.35 ± 0.3 Ga (Vokrouhlický et al. 2017; see also Dykhuis et al. 2014). This age is consistent with the sample reset ages of the Itokawa samples and the inferred crater retention age of Gaspra from Section 5.6. Finally, Itokawa is an excellent match with the LL-like spectral signature of Flora itself (e.g., Reddy et al. 2014; Binzel et al. 2019).

Putting these clues together, we predict that Itokawa was produced by the disruption of the Flora parent body, and that it was once a member of the Flora asteroid family. A likely evolution scenario is that after formation, Itokawa resided near ~2.2 au until it drifted inward far enough due to Yarkovsky thermal forces to escape from the main belt via ν_6 secular resonance (perhaps near 2.14 au).

We can use this concept to calculate Itokawa's mean collision probability and impact velocity with the rest of the main belt population. In Figure 17, we show P_i values (and report mean V_{imp} values) for Itokawa model asteroids encountering the 682 main

belt asteroids with $D_{ast} \geqslant 50$ km discussed in Section 4. The model asteroids were assigned semimajor axes of 2.14–2.2 au and proper eccentricity and inclination values similar to Gaspra's, a Flora family member (Table 3). They yield a mean value of $P_i = 2.401$ (± 0.11) $\times$ 10^{-18} km^{-2} yr^{-1} and $V_{imp} = 4.98$ (± 0.04) km s^{-1}. For reference, Gaspra's P_i value of 2.635×10^{-18} km^{-2} yr^{-1} is 1.1 times that of Itokawa's. We do not model the portion of Itokawa's orbit where it was collisionally decoupled from the main asteroid belt; dynamical models suggest that this portion of its evolution was short compared to its journey within the main belt region (e.g., Bottke et al. 2015b).

Our prediction is that if Option 1 is correct, the largest craters in Itokawa's crater SFDs, which are plotted per square kilometer, should lie on top of our model fit to Gaspra's crater SFD in Figure 13, provided we compensate for Itokawa's slightly smaller net collision probability value (i.e., the ratio of collision probabilities for Gaspra and Itokawa is 1.1, so we need to multiply $N_{obs\text{-}crater}$ ($> D_i$) for Itokawa by this value). Using craters derived from the work of Hirata et al. (2009; see also Marchi et al. 2015), we tested this idea in Figure 18. The plot shows that Itokawa's craters with $D_{crater} \sim 0.1$ km—those that presumably are least likely to have been affected by crater erasure—appear to be an extension of the crater SFD found on Gaspra. This result fulfills the predictions of Option 1, though it does not prove it. Given the available information at this time, it can only be considered an interesting coincidence.

For the moment, let us assume that Option 1 is true. Doing so knocks down several additional "logical dominos" and forces us to make several additional predictions that can help us interpret the other NEOs observed by spacecraft:

1. The crater retention age derived from the largest craters on Itokawa is the same age as the Flora family–forming event that took place approximately 1.35 ± 0.3 Ga ago.
2. Despite Itokawa's small size, a crater scaling law of $f \sim 10$ allows us to reasonably estimate its crater retention age.
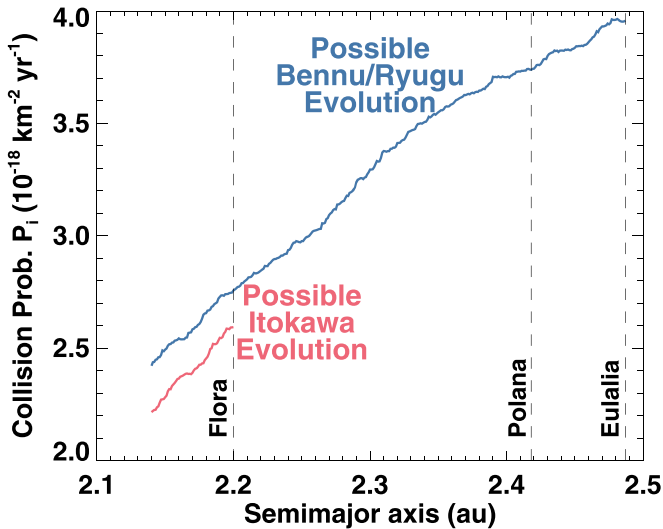3. Given that our preferred scaling law appears to work reasonably well for asteroids larger than 10 km with a

Figure 17. The model collision probabilities of Itokawa, Bennu, and Ryugu as they evolved inward toward the Sun across the main belt due to the Yarkovsky effect. For Itokawa (red), we assumed that it started at 2.2 au, the center of the Flora family, and then migrated to 2.14 au where it escaped the main belt via the ν_6 secular resonance. Our Itokawa model asteroids were assigned proper eccentricity and inclination values similar to Gaspra (Table 2). The collision probabilities P_i were calculated with 682 main belt asteroids with $D_{ast} > 50$ km (Section 2.6). The mean values of all red points are $P_i = 2.401$ (± 0.11) $\times 10^{-18}$ km^{-2} yr^{-1} and $V_{imp} = 4.98$ (± 0.04) km s^{-1}. For Bennu and Ryugu (blue), we assumed that they started at 2.487 au and 2.4 au, the centers of the Eulalia and New Polana families, respectively. The model asteroids were given eccentricities and inclinations of 0°.1 and 3°, respectively. The rest of the method was the same as with Itokawa. The mean P_i value for Bennu and Ryugu starting in either the Eulalia and New Polana families was $(3.3 \pm 0.46) \times 10^{-18}$ km^{-2} yr^{-1} and $(3.1 \pm 0.39) \times 10^{-18}$ km^{-2} yr^{-1}, respectively, and their mean impact velocities V_{imp} were 4.72 (± 0.10) km s^{-1} and 4.67 (± 0.12) km s^{-1}, respectively.

variety of sizes and taxonomic types, and now appears to work for the largest craters on the smallest NEO investigated in our sample (i.e., ~0.3 km; Itokawa), it seems plausible that it will work in similar ways on NEOs such as Toutatis, Bennu, and Ryugu.

4. Despite the fact that YORP spin-up timescales are thought to be fast on Itokawa and other small worlds (see, e.g., the detected spin-up strength in Lowry et al. 2014, and in Vokrouhlický et al. 2015 for other small near-Earth asteroids), the effects of YORP spin-up apparently did not lead to the erasure of craters of $D_{crater} \sim 0.1$ km.

At the moment, though, all we have is an interesting coincidence, and Option 2 must still be considered viable. With these ideas in mind, we move to Toutatis, which is much closer in size to Gaspra than Itokawa.

6.2. Toutatis

(4179) Toutatis is an S-type NEO that is currently residing within the 3:1 mean motion resonance with Jupiter (Figure 19). Its osculating orbit of $(a, e, i) = (2.53$ au, 0.63, 0°.45) places it on an Earth-crossing orbit. The Chinese mission Chang'e-2 flew by Toutatis in 2012 and reported dimensions of 4.354 km × 1.835 km × 2.216 km (Bu et al. 2015; see also Huang et al. 2013). These values largely confirmed estimates made from shape models derived using radar data (Ostro et al. 1995, 1999; Hudson et al. 2003; Takahashi et al. 2013). The estimated bulk density of Toutatis is between 2.1 and
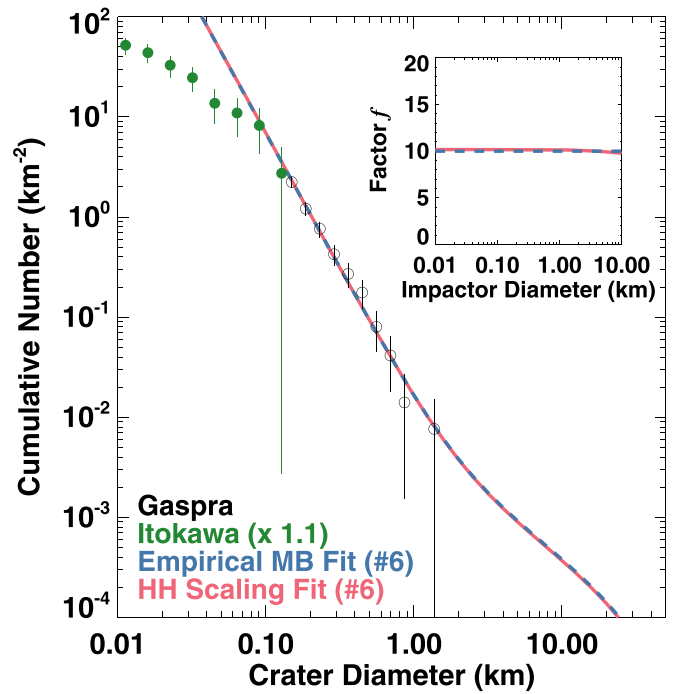

Figure 18. A comparison between craters found on Itokawa and Gaspra and various crater models. Plot components are as in Figure 4. Gaspra is a member of the Flora family, and its crater counts are the black open circles (Figure 13). Its estimated crater retention age is ~1.3 Ga. Itokawa is currently an NEO, but it was probably a member of the Flora family in the past. Itokawa's crater SFD (Hirata et al. 2009; green dots) has been multiplied by the ratio of the collisional probabilities between Gaspra and Itokawa (Figure 17 and Section 6.1). Within errors, the crater spatial densities of Gaspra and the largest craters on Itokawa appear to be the same. If the largest craters on Itokawa were made with the same crater scaling law as Gaspra, they could represent the same crater retention age. The smaller craters on Itokawa have been strongly affected by a crater erasure mechanism (e.g., Richardson et al. 2004). The model crater SFDs are discussed in Figure 13. Here the empirical main belt fit curve (blue line) represents a crater retention age of ~1.38 Ga, whereas the HH scaling fit is ~1.32 Ga (red line).

2.5 g cm^{-3} (Ostro et al. 1999; Birlan 2002). This value is between Itokawa's bulk density (1.9 $\pm$ 0.13 g cm^{-3}) and that of Eros (2.67 $\pm$ 0.03 g cm^{-3}). This could mean that Toutatis has an internal structure somewhere between a classical rubble pile (possibly like Itokawa) and a fractured or possibly shattered object with coherent fragments (i.e., Richardson et al. 2002).

The source of Toutatis is unknown. Given the available information, it is certainly possible that Toutatis is simply a background object that recently escaped the main belt. If we assume that Toutatis was once part of a prominent family, however, we can deduce a plausible parent from the available clues.

We start with spectra. Reddy et al. (2012) found that the spectral signature of Toutatis is most similar to undifferentiated L chondrites, though it lies close to various boundaries between H and L chondrites. The model described by Binzel et al. (2019) suggests a similar result, with probabilities of 46%, 46%, and 8% of Toutatis being an H, L, and LL chondrite, respectively. From these data, we can probably rule out LL chondrite source families in favor of H and L chondrite families.

Next, we consider the results of dynamical models. The NEO model of Granvik et al. (2016, 2018) indicates that

Figure 19. Toutatis is an S-type near-Earth asteroid with dimensions of 4.354 km × 1.835 km × 2.216 km (Bu et al. 2015; see also Huang et al. 2013). It was imaged by the Chang'e-2 spacecraft during a flyby that had a closest approach distance of 770 ± 120 meters (Huang et al. 2013). Courtesy of CNSA.

Toutatis has chances of 22%, 53%, 15%, and 9% of coming from the ν_6 secular resonance near 2.2 au, the 3:1 mean motion resonance with Jupiter, the 5:2 mean motion resonance with Jupiter, and being a Jupiter-family comet, respectively. There are no known Jupiter-family comets that look like S-type asteroids, so we can rule out that possibility at this time. Using the NEO model of Bottke et al. (2002), we find chances of 11%, 18%, 33%, and 39% of coming from the ν_6 secular resonance; the intermediate source Mars region, mostly in the inner main belt; the 3:1 resonance; and outer main belt sources (e.g., 5:2 resonance); respectively. These two models mostly agree with one another, though the outer main belt source is substantially higher in Bottke et al. (2002). Typically, NEOs in these models are favored to come from the inner main belt, which dominates the production of all NEOs, so the higher values found for the 3:1 and 5:2 resonances are intriguing.

We are now ready to consider the observed craters on Toutatis's surface, which range from $40 < D_{\mathrm{crater}} < 530$ m (Huang et al. 2013; Jiang et al. 2015; Figure 20). Craters smaller than a few hundred meters appear to have been depleted by some kind of crater erasure mechanism, like those seen on other small asteroids observed by spacecraft (e.g., Eros, Steins, Itokawa, Ryugu, Bennu; Marchi et al. 2015; Sugita et al. 2019; Walsh et al. 2019). If we only consider the largest craters, we find that their spatial densities are comparable to those on Ida or Eros (Figures 12, 15). Accordingly, depending on the assumed collision probability P_i, and assuming Option 1 is valid, the crater retention age of Toutatis based on the largest craters is likely to be on the order of several billion years.

This result helps our deductive process because there are not many prominent S-type families in the main belt that are old enough to be plausible sources for Toutatis. If we only consider age to be a discriminant, the candidate families include Flora, Maria, Eunomia, and Koronis. Flora can be eliminated because it has an LL-type composition. The Maria family is a possibility; as discussed above, it is adjacent to the 3:1

resonance, it may be >2 Ga old, and the Binzel et al. (2019) model suggests that (170) Maria is most likely to resemble an H chondrite. The Eunomia family appears to be in the LL camp, though L chondrites cannot be ruled out (Vernazza et al. 2014). It is also adjacent to the 3:1 resonance. Finally, there is the Koronis family located next to the 5:2 resonance. The Binzel et al. (2019) model indicates that (158) Koronis, like Toutatis, has comparable odds of being an H or L chrondrite. This apparent similarity could indicate that the Koronis family is a good spectral match with Toutatis.

Additional clues to the origin of Toutatis may come from its inclination, which is very low (0°.45). In general, asteroids evolving into the 3:1 resonance from high-inclination sources such as the Maria or Eunomia families (proper inclinations >12°) have difficulty reaching such low inclinations. Instead, it is much easier to reach a low-inclination orbit by starting with a low-inclination source such as the Koronis family (proper inclinations ~1°–3°). However, Koronis family members evolving into the powerful 5:2 resonance at 2.8 au are less likely to obtain a Toutatis-like semimajor axis unless they are perturbed by Earth during an encounter. This result is reflected in the dynamical results above. Still, the fact that Toutatis is currently on the Earth-crossing line may be a hint that such an event or events took place.

To further quantify our dynamical arguments, we used results from the Granvik et al. (2018) numerical runs to determine how often test asteroids from the Maria/Eunomia and Koronis families reach the (a, e, i) orbit of Toutatis. For the former, we examined the evolution of 1759 test asteroids that reached the 3:1 resonance from starting orbits of $a > 2.5$ au, $0.05 < e < 0.18$, and $11° < i < 16°$. These objects reached resonance in the simulation via Yarkovsky drift forces. We found that 17 of these bodies passed within $\Delta a = 0.03$ au, $\Delta e = 0.03$, and $\Delta i = 1°$ of the (a, e, i) orbit of Toutatis (i.e., 2.53 au, 0.63, 0°.45).

For the Koronis family, we tracked the evolution of 274 test asteroids that entered into 5:2 resonance from starting orbits of $a > 2.5$ au, $0.0 < e < 0.10$, and $0° < i < 3°$. Here, nine test asteroids met our threshold. If we assume that the strength of the two sources above was equal, and we normalize the results by the number of test asteroids used, we find that the ratio favoring Koronis as a source for Toutatis over Maria/Eunomia is 3.4 (i.e., $1759/274 \times 9/17$).

Finally, we return to our cratering results in Figure 20 and compare craters on Toutatis to the Koronis family member Ida. We find it appealing that Toutatis crater counts are a good match to an extrapolation of the model crater SFD from Ida, though we cannot rule out a coincidence.

Putting the evidence together, we postulate that on the basis of spectral, dynamical, and cratering evidence, Toutatis is a lost member of the Koronis family. If Option 1 is correct, the crater retention age of Toutatis based on its largest craters should be the same as Ida, approximately 2–3 Ga.

6.3. Bennu and Ryugu

For our final test, we examine the crater histories of the NEOs Bennu and Ryugu, the targets of the OSIRIS-REx and Hayabusa2 sample return missions, respectively. They share a number of similarities, so we discuss them in tandem. The constraints discussed below mainly come from Lauretta et al. (2019), Hamilton et al. (2019), Sugita et al. (2019), and Watanabe et al. (2019):
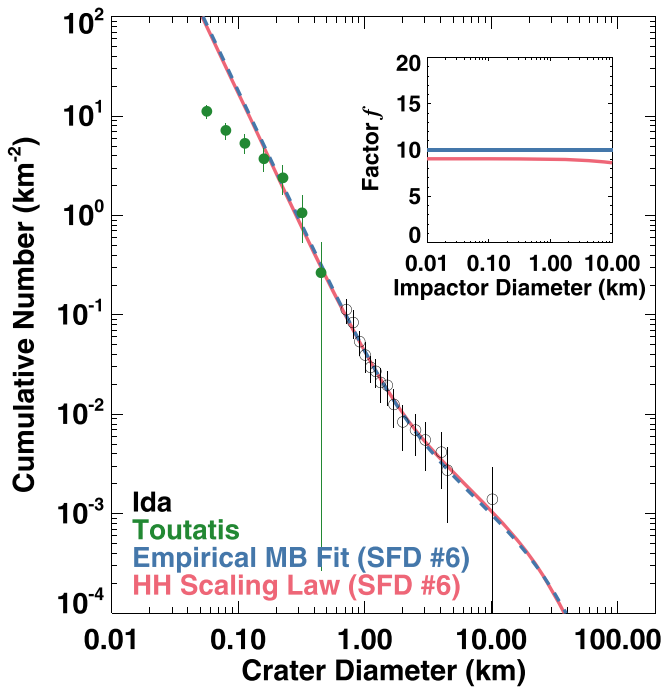
Figure 20. A comparison between craters found on Toutatis and Ida and various crater models. Plot components are as in Figure 4. Ida is a member of the Koronis family, and its crater counts are the black open circles (Figure 12). Its estimated crater retention age is ~2.5 Ga. Toutatis is currently an NEO, but its orbit and spectral signature can be plausibly linked to the Koronis asteroid family. The largest craters on Toutatis (Huang et al. 2013; Jiang et al. 2015; green circles) are aligned with those of Ida's crater SFD. If the largest craters on Toutatis were made with the same crater scaling law as Ida, they could represent the same crater retention age. The smaller craters on Itokawa have been strongly affected by a crater erasure mechanism (e.g., Marchi et al. 2015). The empirical main belt fit curve (blue line) represents a mean crater retention age of ~2.4 Ga, whereas the HH scaling fit is ~2.9 Ga (red line).

1. They both have top-like shapes. Ryugu's dimensions are $1.04 \times 1.02 \times 0.88$ km, while those of Bennu are $0.506 \times 0.492 \times 0.457$ km. This makes Ryugu about twice and eight times as large as Bennu from a diameter and volume perspective, respectively.
2. Both asteroids have a composition similar to primitive carbonaceous chondrites (e.g., CM or CI chondrites). The bodies are spectrally different, but in modest ways: Bennu is taxonomically classified as a B-type asteroid, whereas Ryugu is considered a Cb-type asteroid. Bennu's composition is akin to aqueously altered CM-type carbonaceous chondrites, whereas Ryugu's spectral signature is consistent with thermally and/or shock-metamorphosed CMs.
3. They have the same bulk densities and geometric albedos: $1.19 \, \text{g cm}^{-3}$ and ~4.5%, respectively.
4. Both Bennu and Ryugu appear to be rubble-pile asteroids, with the definition given by Richardson et al. (2002). Their surfaces are a jumble of rocks and boulders that were likely produced in the aftermath of a family-forming event.
5. Their orbital parameters are similar to those of Earth and each other: Bennu's (a, e, i) is (1.126 au, 0.204, 6°.035), and Ryugu's is (1.190 au, 0.1902, 5°.884).
6. The most likely candidate families to produce these bodies are Eulalia and New Polana, located in the inner main belt at low inclinations near the 3:1 mean motion

resonance with Jupiter (J3:1) at 2.5 au (e.g., Campins et al. 2010; Walsh et al. 2013; Bottke et al. 2015b). Bottke et al. (2015b) argue that the New Polana and Eulalia families having an approximate ~70% and ~30% probability of producing Bennu and Ryugu, respectively. The dynamical ages of the New Polana and Eulalia families are modestly different from one another: the former is 1400 [+150, −150] Ma, whereas the latter is 830 [+370, −100] Ma (Bottke et al. 2015b).

7. Both Bennu and Ryugu have obliquities that are nearly 180°: Bennu's is 177°.6, and Ryugu's is 171°.64. This orientation, a probable outcome of YORP evolution (e.g., Bottke et al. 2006b; Vokrouhlický et al. 2015), indicates that both objects were migrating inward via the Yarkovsky effect when they escaped the main belt (e.g., Bottke et al. 2015b).
8. Given the location of the New Polana and Eulalia families between ~2.4 and 2.49 au, the strongest likelihood is that both Bennu and Ryugu drifted inward across the inner main belt from these starting orbits. A likely departure zone from the main belt was through the ν_6 secular resonance that defines the innermost boundary of the inner main belt. At low inclinations, the ν_6 resonance escape zone is near 2.15–2.2 au (Bottke et al. 2002). From there, they reached their current orbits via planetary encounters and interactions with resonances. Given the short lifetime of most NEOs (e.g., a few million to a few tens of millions of years; Bottke et al. 2002; Granvik et al. 2018), Bottke et al. (2015b) predicted tht both Bennu and Ryugu escaped the main belt relatively recently compared to their long transit across the inner main belt.

To glean insights into the crater retention ages of Bennu and Ryugu, it is useful to compare their crater SFDs to an asteroid whose age and crater history are arguably well constrained. Here we choose Gaspra, a member of the Flora family, as our reference surface (Section 5.6; Figures 11 and 13). The reasons why are as follows: Gaspra is located near the likely escape route of Bennu and Ryugu from the main belt, and Gaspra's crater retention age of 1.3 ± 0.3 Ga is both close to the estimated family ages of Eulalia and New Polana and is arguably well defined (i.e., it is consistent with sample ages from Itokawa and the likely age of the Flora family; see Sections 5.6 and 6.1). Here we will superpose the crater SFDs of Bennu and Ryugu on Gaspra's and examine the similarities and differences.

For the comparison to be meaningful, we will assume that the crater scaling laws for Bennu and Ryugu are approximately the same as that of Gaspra. This may be incorrect, with the worlds having different diameters (0.5 and 1.0 km versus 12.2 km) and compositions (primitive carbonaceous chondrite versus LL chondrite), but for the moment we accept this premise. We return to this issue in Section 5.

Second, we need to scale the Bennu–Ryugu crater SFDs for the different collision probabilities that they experienced compared to Gaspra over their orbital histories. As discussed above, Bennu and Ryugu probably came from the low-inclination Eulalia or New Polana families. Accordingly, Bennu and Ryugu probably started with semimajor axes of $2.4 < a < 2.48$ au and inclinations $i \sim 2°–3°$. Next, they would have slowly migrated inward across the inner main belt until they escape out of the ν_6 resonance. To account for this

evolution, we ran collision probability simulations of test asteroids with $(a, e, i) = (2.14–2.48$ au, 0.1, $3°)$ against our asteroid population with $D_{ast} > 50$ km using the methodology discussed in Bottke et al. (1994; Figure 17). We ignore the small portion of time that Bennu and Ryugu were on planet-crossing orbits. If we assume that Bennu and Ryugu had a starting orbit in the Eulalia family, the mean P_i value for their evolution is $(3.3 \pm 0.46) \times 10^{-18}$ km^{-2} yr^{-1}. If we instead assume that they started in the New Polana family at 2.4 au, the mean P_i for their evolution is $(3.1 \pm 0.39) \times 10^{-18}$ km^{-2} yr^{-1}.

The collision probability of Gaspra, $P_i = 2.635 \times 10^{-18}$ km^{-2} yr^{-1}, is 0.8–0.85 times that of Bennu/Ryugu. If we want to compare the crater SFD of Gaspra to that of Bennu and Ryugu, we need to multiply $N_{obs-crater}$ ($>D_i$) for Bennu and Ryugu by one of these values. This will allow us to visually determine whether Bennu and Ryugu are younger or older than Gaspra in a relative sense. If Bennu and Ryugu's crater SFD is lower on a cumulative plot than Gaspra's, its crater retention age is younger than 1.3 ± 0.3 Ga, whereas if it is higher, it is older. Our results are shown in Figures 21 and 22.

We find that Ryugu's craters with $D_{crater} > 0.15$ km (Sugita et al. 2019) appear to be a good fit with Gaspra's craters and the model production crater population (Figure 21). Taken at face value, this would suggest that Ryugu's retention age for these craters is in the range of 1.3 ± 0.3 Ga. This result is interesting because the dynamical ages of Ryugu's postulated source families, New Polana and Eulalia, also match these values (i.e., 1400 [+150, −150] Ma, 830 [+370, −100] Ma, respectively; Bottke et al. 2015b).

Bennu's largest craters (Walsh et al. 2019) also appear to produce a comparable fit, though there is room for interpretation based on the SFD of craters with $D_{crater} > 0.05$ km (Figure 22). Many of Bennu's proposed craters in this size range have subdued topography, which makes it difficult to know whether all of them are valid. In addition, the crater counts from Walsh et al. (2019) are based on data acquired early in the Bennu encounter. Since then, the asteroid has been imaged and the topography measured via lidar to much higher resolution. Additional work on this issue is needed as the crater population is updated using these more recent data.

6.4. Summary

Our results suggest that Option 1 may be valid and that the crater retention ages of NEOs, based on their largest craters, could be surprisingly old. The largest craters on Itokawa, a possible member of the Flora family whose age is ~1.3 Ga, appear to line up with the crater SFD found on Gaspra, a confirmed member of the Flora family. The same can be said for Toutatis, a possible member of the Koronis family (~2–3 Ga), and Ida, a confirmed member of the Koronis family. The largest craters on Bennu and Ryugu also appear to be as ancient as those found on Gaspra, once we account for the different collision probabilities of the impacting population. For each one, this could suggest that some aspects of their surfaces go back as far as the family-forming event that made them. It may be possible to check Option 1 by analyzing the samples returned by the OSIRIS-REx and Hayabusa2 missions.

In Section 7, we will discuss the implications of our findings and whether they make sense given what we know about other modeling and observational data.

7. Discussion

In this paper, we use a new formulation of the main belt size distribution to examine the crater histories of asteroids observed by spacecraft. Some of the key takeaways from our work are as follows.

1. We have used a disruption scaling law that allows asteroids of $D_{ast} \sim 0.2$ km to break up more easily than with the scaling law used by Bottke et al. (2005b; or Benz & Asphaug 1999). It is capable of producing a main belt size distribution that is more consistent with crater constraints than previous work. We find our best results for Q_D^* functions that are higher in number, with #5 and #6 favored when Table 1 probabilities are also considered.

A question that emerges from our research is whether our new asteroid disruption law reflects reality. Unfortunately, it is difficult to assess this issue here without obtaining additional main belt and asteroid constraints. The mismatch between our scaling law and those derived using hydrocode simulations, such as in Benz & Asphaug (1999), may be a clue that our methodology is missing something, that previous scaling laws are missing something, or that everyone is missing something.

In addition to possible issues with methodologies, there may be an issue of how the problem we are investigating is framed. For example, it has been argued that the spin-up of small asteroids by the YORP thermal torques produce frequent mass-shedding events and that this extra source of disruption acts to make the power-law slope of the main belt size distribution shallower than expected between $0.2 < D_{ast} < 2$ km (Penco et al. 2004; Marzari et al. 2011; Jacobson et al. 2014; see discussion in Bottke et al. 2015a). If true, the new asteroid scaling law would essentially replace YORP disruption with impact disruption. From the physics perspective, this works against our collisional evolution model, which does not include this effect, but from the frame of trying to model crater size distributions on asteroids, it may not matter if the two methods yield the same main belt SFD.

It is also conceivable that both processes work together. Laboratory experiments indicate that asteroids spinning near their rotational breakup limit are much easier disrupt by impact than slow-spinning bodies (e.g., Holsapple 2007). This effect was recently studied by Ševeček et al. (2019), who performed a large number of numerical impact simulations with rotating targets using a smoothed particle hydrodynamics code coupled to an N-body code (e.g., see Durda et al. 2004). They found that the critical energy needed to disrupt a target (i.e., the Q_D^* function) changed rapidly when one approaches the critical spin rate of an asteroid. Unfortunately, their study was limited to bodies 10–100 km in diameter, substantially larger than the ~0.2 km bodies whose disruption threshold changes the most in Figure 2. Future work on this issue is needed.

For the moment, let us assume that the YORP effect drives a modest fraction of rubble-pile asteroids with $0.2 < D_{ast} < 2$ km to spin near their disruption limit (e.g., Pravec et al. 2008, 2010) and that this makes them easier to break up by impacts. From a one-dimensional collisional modeling perspective, when their short collisional lifetimes are combined with longer ones from slow rotators, the net effect is that these asteroids are easier to disrupt on average than before. In effect, this rationale can explain the shape of our new asteroid
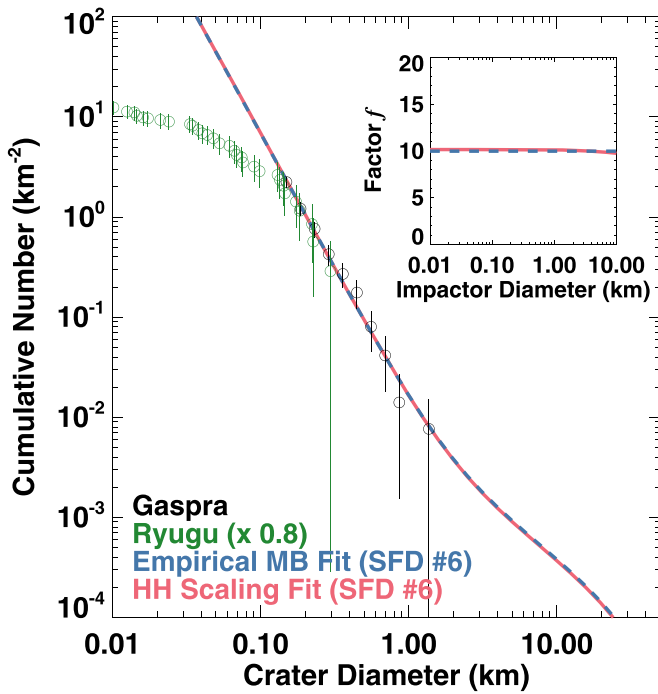
Figure 21. A comparison between craters found on Ryugu and Gaspra and various crater models. Plot components are as in Figure 4. Gaspra is a member of the Flora family, and its crater counts are the black open circles (Figure 13). Its estimated crater retention age is ∼1.3 Ga. Ryugu is currently an NEO, but it is thought to have come from either the New Polana or Eulalia families, with an estimated age of 1.4 [+0.15, −0.15] Ga or 0.83 [+0.37, −0.10] Ga, respectively (Bottke et al. 2015b). Ryugu's crater SFD (Sugita et al. 2019) has been multiplied by the ratio of the collisional probabilities between Gaspra and Ryugu (Figure 17 and Section 6.3). Within errors, the crater spatial densities of Gaspra and the largest craters on Ryugu are similar. If the largest craters on Ryugu were made with the same crater scaling law as Gaspra, they could represent a crater retention age near ∼1.3 Ga. The smaller craters on Ryugu have been strongly affected by a crater erasure mechanism (e.g., Marchi et al. 2015). The model crater SFDs are discussed in Figures 13 and 18.

Figure 22. A comparison between craters found on Bennu and Gaspra and various crater models. Plot components are as in Figure 4. Gaspra crater counts are the black open circles (Figure 13). Its estimated crater retention age is ∼1.3 Ga. Bennu is currently an NEO, but it is thought to have come from the New Polana and Eulalia families (see Figure 21). Bennu's crater SFD (Walsh et al. 2019) has been multiplied by the ratio of the collisional probabilities between Gaspra and Bennu (Figure 17 and Section 6.3). Within errors, the crater spatial densities of Gaspra and the largest craters on Bennu are similar. If the largest craters on Bennu were made with the same crater scaling law as Gaspra, they could represent a crater retention age near ∼1.3 Ga. The smaller craters on Bennu have been strongly affected by a crater erasure mechanism (e.g., Marchi et al. 2015). The model crater SFDs are discussed in Figures 13 and 18.

disruption law, even if our purely collisional model does not account for the physics producing it.

New work will be needed to see how our asteroid disruption law holds up when new constraints become available, more is known about how asteroids disrupt via YORP spin-up, or more is known about the impacts and YORP spin-up working in tandem.

1. Our favored main belt size distribution (#5 or #6) can be successfully fit to the observed crater size distributions found on Ceres (Kerwan basin), Vesta (Rheasilvia basin), Lutetia, Mathilde, Ida, Gaspra, and Eros. Our results indicate that the ratio of crater diameter to projectile diameter f for craters with $D_{crater} > 0.1$ km on these worlds is ∼10. The only exception found so far may be craters smaller than a few kilometers on the 930 km diameter asteroid Ceres.

Our fits between model and crater data indicate that a simple relationship exists between projectiles and crater sizes on asteroids of $D_{ast} > 10$ km. Our test set includes a wide range of asteroid sizes and compositions. Our results also appear broadly consistent with the crater scaling laws of Holsapple & Housen (2007), provided we use certain input parameters (i.e., those suggested by Marchi et al. 2012b for stony asteroids).
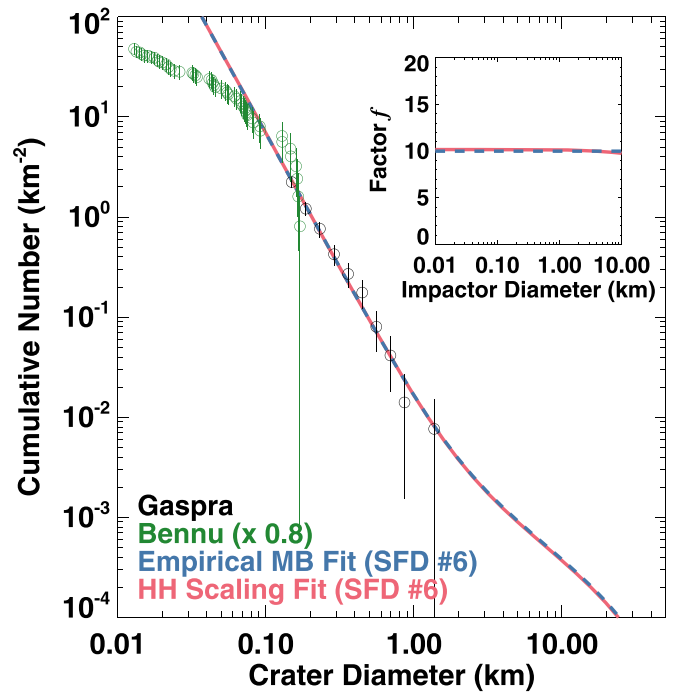
With this said, we add some cautionary notes to this interpretation. The size distribution of craters smaller than a few kilometers on Ceres appears to differ from those on Vesta, with the Ceres SFD having a much steeper power-law slope. If this is not a byproduct of secondary craters, the easiest explanation is that these craters on Ceres are a byproduct of an increasing f value and possibly different material properties for the terrains in question.

It should also be said that our $f \sim 10$ solution for Mathilde's crater SFD is (i) not unique, (ii) based on limited crater data, and (iii) fit to craters that are close to saturation. This situation is unfortunate because Mathilde is the only carbonaceous-chondrite-like asteroid imaged by spacecraft to date that is larger than Ryugu (0.9 km) and smaller than Ceres (930 km). Still, we consider our solution reasonable because $f \gg 10$ scenarios would require some kind of surface reset event within the past billion years that so far lack supporting evidence. The fact that Mathilde has no observed family (Nesvorný et al. 2015) is an argument against the occurrence of such a reset event.

The reasons why the $f \sim 10$ scaling law works as well as it does for many different asteroid sizes and compositions will require additional study, but certain factors probably play a role:

● Most of the asteroids investigated to date probably have comparable material strengths, at least against impact

Table 6
Summary of Results for Asteroids Investigated in This Paper

Asteroid/Region Name	Tax	Asteroid Size (km)	Family	Comments	Sections
Ceres (Kerwan Basin)	Cb	965.2 × 961.2 × 891.2	None	Probable crater retention age of ∼0.8–0.9 Ga based on model fit with craters larger than 2 km	5.2
Vesta (Rheasilvia Basin)	V	572.6 × 557.2 × 446.4	Vesta	Probable crater retention age <1.3 Ga. Age of ∼1 Ga consistent with sample, family constraints	5.1
Lutetia (Achaia Region)	M	121 × 101 × 75	None	Probable crater retention age ∼2.5–3.5 Ga, but surface could be as old as main belt itself.	5.3
Mathilde	C	66 × 48 × 46	None	Probable crater retention age between ∼2.2 Ga and age of the main belt itself.	5.4
Ida	S	59.8 × 25.4 × 18.6	Koronis	Probable crater retention age of ∼2–3 Ga. Consistent with likely dynamical age of the Koronis family.	5.5
Gaspra	S	18.2 × 10.5 × 8.9	Flora	Probable crater retention age of ∼1.3 Ga. Consistent with the likely dynamical age of the Flora family and sample ages from Itokawa.	5.6
Eros	S	34.4 × 11.2 × 11.2	Unknown	Probable crater retention age between ∼2.3 to ∼3.8 Ga. No family has yet been identified as the source.	5.7
Itokawa	S	0.535 × 0.294 × 0.209	Flora	Crater retention age of the largest craters matches the Gaspra and Itokawa sample ages, provided $f \sim 10$.	6.1
Toutatis	S	4.354 × 1.835 × 2.216	Koronis	Crater retention age of the largest craters matches those of Ida and the likely dynamical age of the Koronis family, provided $f \sim 10$.	6.2
Ryugu	Cb	1.04 × 1.02 × 0.88	Eulalia or New Polana	Crater retention age of the largest craters ∼1 Ga, provided $f \sim 10$.	6.3
Bennu	B	0.506 × 0.492 × 0.457	Eulalia or New Polana	Crater retention age of the largest craters ∼1 Ga, provided $f \sim 10$.	6.3

Note. For each asteroid, we list the taxonomic type, its dimensions, its association with a given asteroid family, comments on its probable crater retention age and the age match with auxiliary constraints, and the section of the paper where the asteroid is discussed.

events. They can be considered fractured or shattered versions of the stony meteorites in our collection.

● The collision velocities between asteroids in the main belt do not vary strongly from world to world, with typically mean velocities near $\sim 5\,\mathrm{km\,s^{-1}}$ (Bottke et al. 1994).

● The surface histories of the asteroids investigated here have been dominated by impacts from a main belt SFD whose shape has been in quasi-steady state for billions of years. Although different asteroids disrupt over time, the broad-scale properties of the main belt population have not changed substantially from a collisional evolution perspective over that interval.

The influence of impactors embedded in the early main belt population (e.g., comets implanted in the primordial asteroid belt; Levison et al. 2009; Vokrouhlický et al. 2016) has yet to be detected in the crater histories of main belt asteroids. The reason is probably because few, if any, of the surfaces investigated in this paper go back to the primordial days of the main belt. To explore earlier bombardment eras, we would need to examine the most ancient surfaces on Vesta or other as-of-yet unobserved large asteroids. This remains a fascinating topic for future work.

1. Our derived main belt size distribution, combined with a crater scaling law of $f \sim 10$, can be fit to the largest craters on Itokawa, Toutatis, Bennu, and Ryugu. All of these asteroids are smaller than Gaspra. The match yields a crater retention age on the order of ~ 1 Ga for Itokawa, Bennu, and Ryugu, and ~ 2.5 Ga for Toutatis. These values are consistent with the computed formation ages of their source families (Itokawa from the Flora family, Bennu and Ryugu from the Eulalia or New Polana families, Toutatis from the Koronis family), though that does not prove they actually have these surface ages.

The possibility that the largest craters on these asteroids are ancient matches modeling work (e.g., Walsh et al. 2019), but we still consider it something of a surprise. Therefore, we will discuss this topic further below. Our work shows four out of four examples where the crater retention ages of small asteroids match their predicted family ages. If this is merely a coincidence, it is a good one. With that said, there are other factors to consider here, and they may suggest that the crater retention ages of Itokawa, Toutatis, Bennu, and Ryugu are younger than postulated. We present the arguments and their possible counters below.

7.1. Factor 1. Does Spin-up from YORP Reset the Surfaces of Most Small NEOs?

Over the past decade, it has become increasingly apparent that the YORP thermal torques modify the spin rates and obliquities of asteroids smaller than Gaspra (e.g., reviewed in Bottke et al. 2002, 2006b; Vokrouhlický et al. 2015). They provide the easiest way to explain the spin rate distribution of NEOs and main belt asteroids—which include numerous bodies spinning near fission speeds and other bodies that have almost no rotational angular momentum (e.g., Pravec et al. 2008)—and their obliquity distribution, with small main belt asteroids having preferentially extreme obliquity values (e.g., Hanuš et al. 2013; Ďurech et al. 2018), and many NEOs having values near $\sim 180°$ (e.g., La Spina et al. 2004; Farnocchia et al. 2013). They may also provide a ready explanation for the

spinning top-like shapes of Bennu, Ryugu, and many other asteroids (e.g., Walsh & Jacobson 2015).

Direct measurements of YORP accelerations indicate that they should frequently cause asteroids to undergo mass-shedding events (e.g., Pravec et al. 2010; Jewitt et al. 2015). As a second example, in situ studies of Bennu indicate that its rotation rate is currently accelerating at a rate of $(3.63 \pm 0.52) \times 10^{-6}\,\mathrm{deg\,day^{-2}}$, enough to double Bennu's rotation rate in 1.5 Myr (e.g., Hergenrother et al. 2019; Scheeres et al. 2019), and a similar acceleration was detected for a number of other small NEAs (reviewed in Vokrouhlický et al. 2015).

The implication of these results is that small asteroids can be quite dynamic places. Many should undergo surface changes on timescales that are short compared to our estimated crater retention ages for small NEOs.

A caveat is so-called stochastic YORP, namely that asteroid shape changes driven by mass movement, craters, and mass shedding can cause an asteroid's spin acceleration to undergo a random walk (Statler 2009; Bottke et al. 2015b). This effect may prevent some asteroids from reaching the kinds of rotation speeds that allow for frequent mass-shedding events, or at least considerably delay it, whereas others may enter into mass-shedding events again and again. Another intriguing possibility is that YORP self-regulates itself into a long-lived equilibrium state for the surviving population of bodies, or at least a subpopulation, considerably weakening the YORP effects (e.g., Golubov & Scheeres 2019).

Until this process is better understood, we must leave open the possibility that Itokawa, Toutatis, Bennu, and Ryugu fall into the former class of objects, and that their largest craters are indeed ancient.

There is also the possibility that some top shapes are formed in the family-forming event, with small objects growing through the gravitational reaccumulation of debris (Michel et al. 2019). In this scenario, ejected material grows by the gravitational accretion of nearby bodies, and this leads to more mass being accreted near the equator of the growing rubble-pile asteroid than near the pole. If true, the shapes of Bennu and Ryugu may indeed be ancient, which would lend credence to the idea that they have old retention ages for their largest craters.

7.2. Factor 2. Are Near-Earth Objects Preferentially Long-lived Asteroids?

Our CoDDEM model results allow us to make predictions on the typical collisional lifetime of asteroids based on a choice of our asteroid disruption law (Q_D^*). We find that the sizes of the smallest asteroids in our sample, Itokawa and Bennu, are relatively close to the minimum in the Q_D^* function shown in Figure 2. Accordingly, these bodies should be easier to disrupt on an energy per mass scale by impact events than asteroids that are considerably smaller or larger.

There are feedbacks here, however, with the shallow slope of the main belt SFD between 0.2 and 2 km leading to fewer projectiles for $D_{\mathrm{ast}} < 0.2$ km than estimated by Bottke et al. (2005b). This leads to an average collisional lifetime for Itokawa- and Bennu-sized asteroids on the order of one hundred to a few hundred Myr, comparable to the values estimated in Bottke et al. (2005b). Regardless, these intervals are much shorter than the estimated crater retention ages of Itokawa and Bennu. This mismatch is a potential argument that

the crater retention ages of the largest craters are not on the order of 1 Ga, but instead are much younger.

The counter to this argument is to consider how Itokawa- and Bennu-sized asteroids from a given family escape the main belt after a family-forming event. As a useful example, we refer the reader to the model results from Bottke et al. (2015b). They used numerical simulations to track how Bennu-sized asteroids from the Eulalia, New Polana, and Erigone families evolved in semimajor axis through the coupled Yarkovsky/YORP effects. Their work accounted for the likely collisional lifetime of their model asteroids; those that were disrupted were removed from the simulation. Their goal was to reproduce the distribution of these families in semimajor axis–absolute magnitude (*a*, *H*) space, where the observed families make a quasi-"V" shape.

The setup for the Bottke et al. (2015b) simulations was as follows. They assumed that a large breakup event created a size distribution of asteroids representing the Eulalia, New Polana, and Erigone families. As shorthand, we classify 0.3–1 km bodies as "small," 1–4 km bodies as "modest sized," and objects larger than 4 km as "big." All of these bodies begin to drift inward or outward toward resonances via the Yarkovsky and YORP effects. YORP torques cause the obliquities of the bodies to evolve toward 0° or 180°, where they obtain their maximum semimajor axis drift velocities from the Yarkovsky effect. The smaller fragments migrate more quickly than the modest-sized ones, which in turn move faster than the big ones. This creates a V shape in (*a*, *H*) space, with smaller objects evacuated from the middle of the family (e.g., Figure 18 of Bottke et al. 2015b). We refer to the two sides of the V shape as "ears."

As small and modest-sized bodies are disrupted, according to their assumed collisional lifetimes, attrition takes its toll on the leading edge of each ear. Only a fraction live long enough to make it to an "escape hatch" resonance that will take them out of the main belt. Some of these bodies also go through YORP cycles, where their obliquity values are reset by various processes. The small bodies have the shortest timescale to undergo YORP cycles, and it causes them to undergo a random walk in semimajor axis, slowing their progress toward an escape hatch resonance.

Eventually, though, this wave of surviving bodies reaches an escape hatch resonance. A specific example is shown in Figure 19 of Bottke et al. (2015b), where Bennu-sized bodies from Eulalia and New Polana reached various inner main belt resonances over timescales of 0.1 to >2 Gyr after the family-forming event. The expected flux of these escaping bodies at the estimated ages of the families was found to be consistent with the available constraints.

Taken together, these results indicate that the NEO population might be dominated by "lucky" asteroids that are long-lived survivors. An analogy might be World War I soldiers running across no man's land to reach the trenches of their enemy; most soldiers fall during the assault, but a few make it. If this scenario is accurate, Itokawa, Toutatis, Bennu, and Ryugu would be survivors of this gauntlet, which would make their putative ancient large craters less surprising and more of a selection effect. On the other hand, a small asteroid can survive and still not have an ancient crater retention age. The takeaway is that it may not be straightforward to interpret the surfaces of these small asteroids.

It is also possible that Itokawa, Toutatis, Bennu, and Ryugu are second-generation family members, but we predict that is unlikely. When big family members disrupt, they will create some modest-sized bodies and lots of small bodies, all of which can now drift more rapidly. The starting location of these fragments, however, will often be closer to the center of the family than at great distances from the center. The initial second-generation population will also be smaller in number than the initial first-generation population, and they experience the same attrition factors as first-generation bodies. All of this suggests that the second-generation bodies that escape the main belt are unlikely to outnumber the first-generation bodies for a considerable time after the family-forming event.

7.3. Factor 3. What Crater Scaling Laws are Applicable to Small Asteroids?

There is considerable debate about the projectile sizes needed to make small craters on asteroids, primarily because the strength of the surface materials is unknown. Estimates in the literature differ by many orders of magnitude, and this can change *f* values from 10 to 40 or more (e.g., O'Brien et al. 2006; Tatsumi & Sugita 2018).

An innovative way to glean insights into this issue was through the SCI experiment carried by JAXA's Hayabusa2 mission to Ryugu. The SCI consisted of a 30 cm disk impactor made of copper that was accelerated by an explosion to an impact speed with Ryugu of $2 \, \mathrm{km \, s^{-1}}$. The impact produced a cone-shaped debris curtain and a crater-like feature that was approximately 17.6 ± 0.7 m in diameter rim to rim (Arakawa et al. 2020). This value is so large that the Hayabusa2 team suggested that Ryugu's surface acts like it has the same strength as cohesionless sand upon impact, corresponding to $f \gg 10$. If so, and if we can assume this result is applicable to all Ryugu craters, it would imply that Ryugu's crater retention age is considerably younger than 1 Ga.

The caveat that we can provide at this time is that the creation of craters with $D_{\mathrm{crater}} > 100$ m on Ryugu may be different than the formation of much smaller craters a few tens of meters across. If true, different projectile sizes are sensitive to how the terrains can change as they become larger (e.g., boulder concentrations per unit area, etc.).

7.4. Factor 4. Do Scaling Laws Change the Size Distributions of Small Craters?

Assuming that the crater retention ages for Itokawa, Toutatis, Bennu, and Ryugu are young carries its own implications. For example, it means that crater scaling laws must change between Eros- and Gaspra-sized and larger objects ($D_{\mathrm{ast}} > 10$ km), which have $f \sim 10$, and smaller asteroids, where presumably $f \gg 10$. From our work above, it is not yet clear how one would tell the difference between the two.

As an example, consider two asteroids with the same age, a large one where $f \sim 10$ and a small one where $f \sim 50$. Our model main belt SFD in Figure 1 shows that the slope of <0.1 km asteroids follows a Dohnanyi-like power-law slope of -2.6 (e.g., O'Brien & Greenberg 2003, 2005; Bottke et al. 2015a). If we assume that projectiles striking from this portion of the SFD will create a crater SFD on these two bodies with the same slope, the only outward difference between the two would be in crater spatial densities.

The hope would be to find a transitional target body where large craters follow $f \sim 10$ and smaller craters follow $f \gg 10$. This would produce a change in the slope of the crater SFD that

would be observable. The issue is that crater erasure on small bodies makes such signatures rare or hard to interpret. We speculate that crater erasure may even be a byproduct of this change in f; models indicate that increasing f for small craters might make them more effective at crater erasure. This scenario warrants further work.

The prevalence of a Dohnanyi-like power-law slope of -2.6 at small asteroid sizes may also help explain the coincidence of why the largest craters on Itokawa, Toutatis, Bennu, and Ryugu have the same crater retention age as their putative source families. For every target body, there must be a largest crater that can form; asteroids striking a surface that are larger than a critical threshold will produce an asteroid-wide surface resetting event and/or disruption. Our work indicates that f values near 10 or $\gg 10$ will be drawn from the same -2.6 slope in the main belt SFD. If $f \gg 10$, we can expect a young crater retention age, with the largest possible crater forming relatively quickly compared to the formation age of the asteroid.

If this logic holds, it could be rare for the surface of a small asteroid to be caught between a reset event and the formation of its largest crater. This would make the true crater retention ages of Itokawa, Toutatis, Bennu, and Ryugu much younger than suggested.

One way to test this hypothesis is to determine the shock-resetting (e.g., Ar–Ar) and surface (cosmic ray exposure) ages of samples returned from Bennu and Ryugu. We might expect to find the formation age of the family in the samples, as was attempted for Itokawa (e.g., Park et al. 2015), but there may also be evidence of other impact events. If they skew toward younger ages, this may be evidence that impacts only affected those rocks that had been brought to the surface over relatively recent times. On the other hand, finding numerous impact ages could tell us that (i) the surface is indeed ancient or (ii) there have been a multitude of resetting events, with the samples recording impacts back to the formation of the target asteroid.

8. Future Work

Future work promises to increase the fidelity of the four components of our crater production models presented in Section 2.1. For example, one way to improve our calculation of Component 1 (assessment of main belt SFD) is for new surveys of main belt asteroids to come online that can more easily detect sub-kilometer asteroids. A present-day example of this comes from Heinze et al. (2019), who discussed how Dark Energy Camera observations have probed the small-body size distribution of the main belt. It is also expected that future wide-field surveys such as the Vera C. Rubin Observatory, previously referred to as the Large Synoptic Survey Telescope (LSST), and NASA's Near-Earth Object Surveillance Mission will be able to detect numerous main belt bodies in the sub-kilometer range across the main belt.

These surveys will also give us increased knowledge of the nature of the kilometer and sub-kilometer main belt populations. This information is needed to calculate improved collision probabilities and impact velocities between our target asteroids and a representative population of main belt asteroids (Component 3).

In terms of crater scaling laws for small asteroids (Component 2), new data will be provided by NASA's Double Asteroid Redirection Test (DART) mission (Cheng et al. 2018) and ESA's Hera mission (Michel et al. 2018). DART is a kinetic impactor that will hit the 160 m moon of Didymos, a 780 m diameter near-Earth asteroid. This event will make a crater and change the angular momentum of the system. Hera will follow-up the DART mission with a detailed post-impact survey of the Didymos system. From Hera, we will gain new insights into the projectile sizes needed to make small craters on asteroids, and this will translate into new constraints for crater scaling laws.

Finally, we predict that new dynamical modeling work and meteorite/sample analysis may lead to additional constraints for Component 4, the crater retention age of target asteroids. For example, future work may help us identify the likely source family of Eros. If that happens, we can use dynamical models to determine the age of the family-forming event and compare that age to the predicted crater retention age of Eros (i.e., as discussed in Section 5.7, we modestly favor a crater retention age of ~ 2.3–3.8 Ga, but that is based on an assumed starting location and evolutionary history for Eros). In addition, new work on the shock degassing ages of meteorites may allow us to pin down the starting location of certain asteroids and refine our predicted crater retention ages. We look forward to an analysis of the samples returned from Bennu by the OSIRIS-REx spacecraft and from Ryugu by the Hayabusa2 spacecraft. They may retain a record of the family-forming event that created them.

9. Conclusions

Here we summarize the main conclusions of our paper.

We have derived a new formulation of the main belt SFD that is modestly different from the one proposed by Bottke et al. (2005b) (Section 3). We have successfully fit it to numerous asteroid crater SFDs observed by spacecraft. Our results for Ceres (multi-kilometer craters only), Vesta, Lutetia, Mathilde, Ida, Eros, and Gaspra yield a crater scaling law where the ratio of crater sizes to projectile sizes is a factor $f \sim 10$ (Section 5).

From a probability standpoint, our results favor the main belt SFDs #5 and #6 (Figure 1; see also Figure 2). When used as input for crater production models, they yield crater retention ages that often match age constraints derived from other sources (e.g., dynamical model ages of asteroid families; shock degassing ages of asteroid samples; Section 5).

Our derived empirical scaling law largely matches the results produced by the crater scaling law of Holsapple & Housen (2007), provided certain parameters are used (i.e., we assume that the surface material acts like cohesive soils, and that the yield strength of most asteroids is on the order of $Y \sim 2 \times 10^7$ dynes cm^{-2}). Typical values from our input parameters yield $f \sim 10$ (Section 3).

Conversely, the Ivanov scaling law (Schmedemann et al. 2014) yields results that are less successful at matching constraints, at least when applied to crater SFDs that have numerous subkilometer craters. In this size range, its parameter choices yield $f \gg 10$ for target asteroids that are $D_{\rm ast} > 10$ km. The $f \gg 10$ values lead to crater retention ages that are inconsistent with independent ages derived using dynamical methods and/or sample evidence (Section 5).

For the spacecraft-observed asteroids and surfaces tested in this paper, we summarize our findings below and in Table 6.

Vesta (Rheasilvia Basin). We find that the crater retention age of the ~ 500 km Rheasilvia basin on Vesta is probably younger than 1.3 Ga, with a plausible value near ~ 1 Ga. These ages are consistent with the ^{40}Ar/^{39}Ar ages found in feldspar

grains taken from eucrite meteorites, which range between 0.6 and 1.7 Ga (Lindsay et al. 2015; Section 5.1).

Ceres (Kerwan Basin). We predict that the crater retention age of the ~280 km Kerwan basin on Ceres, based on fits to the multi-kilometer and larger craters, is approximately 0.8–0.9 Ga. Our preferred model of $f \sim 10$, however, may not fit the crater SFD for $D_{crater} < 2$ km. The inconsistency in the power-law slopes of sub-kilometer craters on Ceres and Vesta could suggest that (i) secondary craters dominate the crater SFD of small craters on Ceres or (ii) the physical properties of Ceres's surface are so different from those of Vesta that they allow $f \gg 10$ for small craters (Section 5.2).

Lutetia (Achaia Region). The crater retention age of the oldest surface on the M-type asteroid Lutetia (Achaia) is of the order of 2.5–3.5 Ga, though error bars indicate it could also be as old as the formation of Lutetia itself (Section 5.3).

Mathilde. The crater retention age of Mathilde, a carbonaceous chondrite asteroid that is larger than Bennu and Ryugu and smaller than Ceres, appears to be somewhere between 2.2 Ga and the formation age of the body itself, which could go back to the planetesimal formation era. Our interpretation is that $f \sim 10$ for this body makes the most sense; $f \gg 10$ would yield crater retention ages so young that we would expect to see a family associated with Mathilde (Section 5.4).

Ida. The crater retention age of the S-type asteroid Ida, a member of the Koronis family, appears to be between 2 and 3 Ga, though it could be older depending on the cratered surface analyzed. This age is consistent with the expected dynamical age of the Koronis family (Section 5.5).

Gaspra. The crater retention age of the S-type asteroid Gaspra, a member of the Flora family, appears to be ~1.3 Ga. This age is consistent with the expected dynamical age of the Flora family. It also matches the ^{40}Ar/^{39}Ar ages of LL chondrite grains returned from Itokawa by the Hayabusa spacecraft: 1.3 ± 0.3 Ga (Park et al. 2015). We predict that Itokawa is very likely to have been a Flora family member prior to becoming an NEO (Section 5.6).

Eros. The crater retention age of the S-type asteroid Eros is between ~2.3 and 3.8 Ga. Although Eros is an NEO with a likely LL chondrite composition, it does not appear to be a lost member of the Flora family. The origin of Eros is currently an unsolved problem (Section 5.7).

Itokawa. Itokawa is a small S-type NEO that was likely to have once been part of the Flora family (see Gaspra above). If we limit our analysis to its largest craters, we find that Itokawa's crater spatial densities match those found on Gaspra, another Flora family member. Moreover, if these large craters formed with $f \sim 10$, they suggest that components of Itokawa's crater history tell the story of the billion-year interval between the formation of the Flora family and the present day (Section 6.1). On the other hand, the crater retention age based on the largest craters could be young if $f \gg 10$.

Toutatis. Based on the results of dynamical models and spectroscopic interpretation, we predict that the 2.5 km S-type NEO Toutatis was once part of the Koronis family. We find that the crater spatial densities of its largest craters match trends in the SFD of Ida, a Koronis family member. If these large craters formed with $f \sim 10$, components of the observed surface on Toutatis could be as old as the Koronis family-forming event (Section 6.2).

Bennu and Ryugu. Bennu and Ryugu are 0.5 and 0.9 km carbonaceous chondrite asteroids, respectively. The crater spatial densities of their largest craters were found to be comparable to the crater SFD found on Gaspra, whose surface is the order of 1.3 Ga old. If these large craters formed with $f \sim 10$, both worlds could have observed surface features as old as the predicted source families for these worlds, Eulalia and New Polana, which are nearly 1 Ga old. Alternatively, they could have young surfaces if the crater scaling law derived from the Hayabusa2 impact experiments is applicable to all observed craters on both worlds (Section 6.3).

The largest craters on Itokawa, Toutatis, Bennu, and Ryugu yield ages of ~1, 2.5, 1, and 1 Ga, respectively, provided $f \sim 10$. There are some reasons to think it could be illusionary, with the reality being that the largest craters on these worlds formed with $f \gg 10$, but we are unable to dismiss these ancient ages out of hand.

If the largest craters on these worlds are indeed old, all four of these NEOs, and in fact most NEOs, are likely the fortunate survivors of collisional evolution within the main belt region. Tracking the collisional and dynamical evolution of individual main belt bodies across the main belt, and accounting for the possibility of a collisional cascade that allows a breakup event to produce daughter fragments, can potentially be simulated by the next generation of numerical models (Section 7).

On the other hand, if the largest craters on these four NEOs are instead relatively young, f either had to go from a value of 10 for Eros/Gaspra/larger bodies to $f \gg 10$ for only slightly smaller bodies or it had to change on the surfaces of the four NEOs themselves. In the latter case, the evidence for this change would be found by modeling the SFD of the smaller craters that have been strongly affected by crater erasure. Finding evidence of how and why this happens could lead us to a better understanding of the physical nature of asteroids and how they are affected by collisions (Section 7).

ORCID iDs

W. F. Bottke https://orcid.org/0000-0002-1804-7814
D. Vokrouhlický https://orcid.org/0000-0002-6034-5452
R.-L. Ballouz https://orcid.org/0000-0002-1772-1934
O. S. Barnouin https://orcid.org/0000-0002-3578-7750
H. C. Connolly, Jr. https://orcid.org/0000-0002-1803-5098
S. Marchi https://orcid.org/0000-0003-2548-3291
P. Michel https://orcid.org/0000-0002-0884-1993
B. Rizk https://orcid.org/0000-0002-0823-9804
D. J. Scheeres https://orcid.org/0000-0003-0558-3842
K. J. Walsh https://orcid.org/0000-0002-0906-1761
D. S. Lauretta https://orcid.org/0000-0002-2597-5950

References

Aljbaae, S., Carruba, V., Masiero, J. R., Domingos, R. C., & Huaman, M. 2017, MNRAS, 471, 4820

Arakawa, M., Saiki, T., Wada, K., et al. 2020, Sci, 368, 67

Barnouin, O. S., Daly, M. G., Palmer, E. E., et al. 2019, NatGe, 12, 247

Belton, M. J. S., Champman, C. R., Klaasen, K. P., et al. 1996, Icar, 120, 1

Belton, M. J. S., Veverka, J., Thomas, P., et al. 1992, Sci, 257, 1647

Benz, W., & Asphaug, E. 1999, Icar, 142, 5

Binzel, R. P., DeMeo, F. E., Turtelboom, E. V., et al. 2019, Icar, 324, 41

Birlan, M. 2002, EM&P, 88, 1

Bottke, W. F. 2014, LPICo, 1773, 2024

Bottke, W. F., Brož, M., O'Brien, D. P., et al. 2015a, in Asteroids IV, ed. P. Michel, F. DeMeo, & W. F. Bottke (Tucson, AZ: Univ. Arizona Press), 701

Bottke, W. F., Durda, D. D., Nesvorný, D., et al. 2005a, Icar, 175, 111

Bottke, W. F., Durda, D. D., Nesvorný, D., et al. 2005b, Icar, 179, 63

Bottke, W. F., Morbidelli, A., Jedicke, R., et al. 2002, Icar, 156, 399

Bottke, W. F., Nesvorný, D., Grimm, R. E., Morbidelli, A., & O'Brien, D. P. 2006a, Natur, 439, 821

Bottke, W. F., Nolan, M. C., Kolvoord, R. A., & Greenberg, R. 1994, Icar, 107, 255

Bottke, W. F., Nolan, M. C., Melosh, H. J., Vickery, A. M., & Greenberg, R. 1996, Icar, 122, 406

Bottke, W. F., Vokrouhlický, D., Brož, M., Nesvorný, D., & Morbidelli, A. 2001, Sci, 294, 1693

Bottke, W. F., Vokrouhlický, D., Rubincam, D. P., & Nesvorný, D. 2006b, AREPS, 34, 157

Bottke, W. F., Vokrouhlický, D., Walsh, K. J., et al. 2015b, Icar, 247, 191

Brož, M., Morbidelli, A., Bottke, W. F., et al. 2013, A&A, 551, A117

Bu, Y., Tang, G., Di, K., et al. 2015, AJ, 149, 21

Campins, H., Morbidelli, A., Tsiganis, K., et al. 2010, ApJL, 721, L53

Campins, H., de León, J., Morbidelli, A., et al. 2013, AJ, 146, 26

Chapman, C. R. 2002, in Asteroids IV, ed. W. F. Bottke et al. (Tucson, AZ: Univ. Arizona Press), 315

Chapman, C. R., Merline, W. J., & Thomas, P. 1999, Icar, 140, 28

Chapman, C. R., Ryan, E. V., Merline, W. J., et al. 1996a, Icar, 120, 77

Chapman, C. R., Veverka, J., Belton, M. J. S., Neukum, G., & Morrison, D. 1996b, Icar, 120, 231

Cheng, A. F., Rivkin, A. S., Michel, P., et al. 2018, P&SS, 157, 104

Chesley, S. R., Farnocchia, D., Nolan, M., et al. 2014, Icar, 235, 5

Clement, M. S., Kaib, N. A., Raymond, S. N., & Walsh, K. J. 2018, Icar, 311, 340

Coradini, A., Capaccioni, F., Erard, S., et al. 2011, Sci, 334, 492

Davison, T. M., Raducan, S. D., Collins, G. S., & Bland, P. A. 2019, LPI, 2132, 2385

de León, J., Licandro, J., Serra-Ricart, M., Pinilla-Alonso, N., & Campins, H. 2010, A&A, 517, A23

Dell'Oro, A., Marzari, F., Paolicchi, P., & Vazani, V. 2001, A&A, 366, 1053

Dohnanyi, J. S. 1969, JGR, 74, 2531

Dunn, T. L., Burbine, T. H., Bottke, W. F., & Clark, J. P. 2013, Icar, 222, 273

Durda, D. D., Bottke, W. F., Enke, B. L., et al. 2004, Icar, 170, 243

Durda, D. D., Bottke, W. F., Nesvorný, D., et al. 2007, Icar, 186, 498

Durda, D. D., Greenberg, R., & Jedicke, R. 1998, Icar, 135, 431

Ďurech, J., Hanuš, J., & Alí-Lagoa, V. 2018, A&A, 617, A57

Dykhuis, M., Molnar, L., Van Kooten, S. J., & Greenberg, R. 2014, Icar, 243, 111

Ernst, C. M., Barnouin, O. S., Daly, R. T. & Small Body Mapping Tool Team 2018, LPI, 2083, 1043

Farinella, P., & Davis, D. R. 1992, Icar, 97, 111

Farnocchia, D., Vokrouhlický, D., Milani, A., Spoto, F., & Bottke, W. F. 2013, Icar, 224, 1

Foley, C. N., Nittler, L. R., McCoy, T. J., et al. 2006, Icar, 184, 338

Fowler, J. W., & Chillemi, J. R. 1992, in IRAS Asteroid Data Processing. The IRAS Minor Planet Survey, Tech. Rep. PLTR-92-2049 (PLTR-92-2049) ed. E. F. Tedesco (Hanscom AFB, MA: Phillips Laboratory), 17

Fu, R. R., Ermakov, A. I., Marchi, S., et al. 2017, E&PSL, 476, 153

Fujiwara, A., Kawaguchi, J., Yeomans, D. K., et al. 2006, Sci, 312, 1330

Gladman, B. J., Davis, D. R., Neese, C., et al. 2009, Icar, 202, 104

Golubov, O., & Scheeres, D. J. 2019, AJ, 157, 105

Granvik, M., Morbidelli, A., Jedicke, R., et al. 2016, Natur, 530, 303

Granvik, M., Morbidelli, A., Jedicke, R., et al. 2018, Icar, 312, 181

Greenberg, R., Bottke, W. F., Nolan, M., et al. 1996, Icar, 120, 106

Greenberg, R., Nolan, M. C., Bottke, W. F., Kolvoord, R. A., & Veverka, J. 1994, Icar, 107, 84

Grott, M., Knollenberg, J., Hamm, M., et al. 2019, NatAs, 3, 971

Hamilton, V. E., Simon, A. A., Christensen, P. R., et al. 2019, NatAs, 3, 332

Hanuš, J., Ďurech, J., Brož, M., et al. 2013, A&A, 551, A67

Harris, A. W., & D'Abramo, G. 2015, Icar, 257, 302

Heinze, A. N., Trollo, J., & Metchev, S. 2019, AJ, 158, 232

Hergenrother, C. W., Maleszewski, C. K., Nolan, M. C., et al. 2019, NatCo, 10, 1291

Hiesinger, H., Marchi, S., Schmedemann, N., et al. 2016, Sci, 353, 4759

Hiesinger, H., van der Bogert, C. H., Pasckert, J. H., et al. 2012, JGRE, 117, E00H10

Hirata, N., Barnouin-Jha, O. S., Honda, C., et al. 2009, Icar, 200, 486

Holsapple, K. A. 2007, Icar, 187, 500

Holsapple, K. A., & Housen, K. R. 2007, Icar, 187, 345

Holsapple, K. A., & Housen, K. R. 2019, P&SS, 179, 104724

Hopkins, M. D., Mojzsis, S. J., Bottke, W. F., & Abramov, O. 2015, Icar, 245, 367

Housen, K. J., & Holsapple, K. A. 2003, Icar, 163, 102

Housen, K. J., Holsapple, K. A., & Voss, M. E. 1999, Natur, 402, 155

Housen, K. J., Sweet, W. J., & Holsapple, K. A. 2018, Icar, 300, 72

Huang, J., Ji, J., Ye, P., et al. 2013, NatSR, 3, 3411

Hudson, R. S., Ostro, S. J., & Scheeres, D. J. 2003, Icar, 161, 346

Ivanov, B. A., & Melosh, H. J. 2013, JGRE, 118, 1545

Ivanov, B. A., Neukum, G., Bottke, W. F., & Hartmann, W. K. 2002, in Asteroids III, ed. W. F. Bottke et al. (Tucson, AZ: Univ. Arizona Press), 89

Ivanov, B. A., Neukum, G., & Wagner, R. 2001, ASSL, 261, 1

Ivezić, Ž., Tabachnik, S., Rafikov, R., et al. 2001, AJ, 122, 2749

Jacobson, S. A., Marzari, F., Rossi, A., Scheeres, D. J., & Davis, D. R. 2014, MNRAS, 439, L95

Jedicke, R., Larsen, J., & Spahr, T. 2002, in Asteroids III, ed. W. F. Bottke et al. (Tucson, AZ: Univ. Arizona Press), 71

Jewitt, D., Hsieh, H. H., & Agarwal, J. 2015, in Asteroids III, ed. W. F. Bottke et al. (Tucson, AZ: Univ. Arizona Press), 221

Jiang, Y., Ji, J., Huang, J., et al. 2015, NatSR, 5, 16029

Jutzi, M., Asphaug, E., Gillet, P., Barrat, J.-A., & Benz, W. 2013, Natur, 494, 207

Kessler, D. J. 1981, Icar, 48, 39

Kitazato, K., Milliken, R. E., Iwata, T., et al. 2019, Sci, 364, 272

Knežević, Z., Lemaitre, A., & Milani, A. 2002, in Asteroids III, ed. W. F. Bottke et al. (Tucson, AZ: Univ. Arizona Press), 603

La Spina, A., Paolicchi, P., Kryszczyńska, A., & Pravec, P. 2004, Natur, 428, 400

Lauretta, D. S., Dellagiustina, D. N., Bennett, C. A., et al. 2019, Natur, 568, 55

Levison, H. F., Bottke, W. F., Gounelle, M., et al. 2009, Natur, 460, 364

Lindsay, F. N., Delaney, J. S., Herzog, G. F., et al. 2015, E&PSL, 413, 208

Lowry, S., Weissman, P. R., Duddy, S. R., et al. 2014, A&A, 562, A48

Manley, S. P., Migliorini, F., & Bailey, M. E. 1998, A&AS, 133, 437

Marchi, S., Bottke, W. F., Cohen, B. A., et al. 2013, NatGe, 6, 303

Marchi, S., Bottke, W. F., O'Brien, D. P., et al. 2014, P&SS, 103, 96

Marchi, S., Chapman, C. R., Barnouin, O. S., Richardson, J. E., & Vincent, J.-B. 2015, in Asteroids IV, ed. P. Michel, F. DeMeo, & W. F. Bottke (Tucson, AZ: Univ. Arizona Press), 725

Marchi, S., Ermakov, A. I., Raymond, C. A., et al. 2016, NatCo, 7, 12257

Marchi, S., Massironi, M., Vincent, J. -B., et al. 2012b, P&SS, 66, 87

Marchi, S., McSween, H. Y., O'Brien, D. P., et al. 2012a, Sci, 336, 690

Marchi, S., Mottola, S., Cremonese, G., et al. 2009, AJ, 137, 4936

Marzari, F., Rossi, A., & Scheeres, D. J. 2011, Icar, 214, 622

Masiero, J., Mainzer, A. K., Grav, T., et al. 2011, ApJ, 741, 68

Masiero, J. R., DeMeo, F. E., Kasuga, T., & Parker, A. H. 2015, in Asteroids IV, ed. P. Michel, F. DeMeo, & W. F. Bottke (Tucson, AZ: Univ. Arizona Press), 323

Massironi, M., Marchi, S., Pajolab, M., et al. 2012, P&SS, 66, 125

Mazrouei, S., Ghent, R. R., Bottke, W. F., et al. 2019, Sci, 363, 253

McSween, H. Y., Emery, J. P., Rivkin, A. S., et al. 2018, M&PS, 53, 1793

Melosh, H. J. 1989, Impact Cratering: A Geologic Process (New York: Oxford Univ. Press)

Michel, P., Ballouz, R.-L., Barnouin, O. S., et al. 2020, Nat. Commun., 11, 2655

Michel, P., Barnouin, O. S., Ballouz, R. -L., et al. 2019, LPI, 2132, 1659

Michel, P., Farinella, P., & Froeschle, C. 1996, Natur, 380, 689

Michel, P., Kueppers, M., Cheng, A., & Carnelli, I. 2018, LPI, 2083, 1144

Minton, D., Richardson, J. E., & Fassett, C. I. 2015, Icar, 247, 172

Morbidelli, A., & Nesvorný, D. 1999, Icar, 139, 295

Morbidelli, A., Nesvorny, D., Bottke, W. F., et al. 2003, Icar, 162, 328

Morbidelli, A., Walsh, K. J, O'Brien, D. P., Minton, D. A., & Bottke, W. F. 2015, in Asteroids IV, ed. P. Michel, F. DeMeo, & W. F. Bottke (Tucson, AZ: Univ. Arizona Press), 493

Moyano-Cambero, C. E., Trigo-Rodríguez, J. M., Llorca, J., et al. 2016, M&PS, 51, 1795
Nakamura, T., Noguchi, T., Tanaka, M., et al. 2011, Sci, 333, 1113
Nesvorný, D., Brož, M., & Carruba, V. 2015, in Asteroids IV, ed. P. Michel, F. DeMeo, & W. F. Bottke (Tucson, AZ: Univ. Arizona Press), 297
Nesvorný, D., Morbidelli, A., Vokrouhlický, D., Bottke, W. F., & Brož, M. 2002, Icar, 157, 155
Nesvorný, D., & Roig, F. 2018, AJ, 155, 42
Nesvorný, D., Roig, F., & Bottke, W. F. 2017, AJ, 153, 103
Nesvorný, D., Vokrouhlický, D., Bottke, W. F., & Levison, H. F. 2018, NatAs, 2, 878
Nolan, M. C., Howell, E. S., Scheeres, D. J., et al. 2019, GeoRL, 46, 1956
O'Brien, D. P., & Greenberg, R. 2003, Icar, 164, 334
O'Brien, D. P., & Greenberg, R. 2005, Icar, 178, 179
O'Brien, D. P., Greenberg, R., & Richardson, J. E. 2006, Icar, 183, 79
Öpik, E. 1951, PRIAA, 54, 165
Ostro, S., Hudson, R. S., Jurgens, R. F., et al. 1995, Sci, 270, 80
Ostro, S., Hudson, R. S., Rosema, K. D., et al. 1999, Icar, 137, 122
Park, J., Turrin, B. D., Herzog, G. F., et al. 2015, M&PS, 50, 2087
Park, R. S., Konopliv, A. S., Bills, B. G., et al. 2016, Natur, 537, 515
Parker, A. H., Ivezić, Ž., Jurić, M., et al. 2008, Icar, 198, 138
Patzold, M., Andert, T. P., Asmar, S. W., et al. 2011, Sci, 334, 491
Penco, U., Dell'Oro, A., Paolicchi, P., et al. 2004, P&SS, 52, 1087
Peplowski, P. N. 2016, P&SS, 134, 36
Peplowski, P. N., Bazell, D., Evans, L. G., et al. 2015, M&PS, 50, 353
Petit, J.-M., Durda, D. D., Greenberg, R., Hurford, T. A., & Geissler, P. E. 1997, Icar, 130, 177
Pravec, P., & Harris, A. W. 2007, Icar, 190, 250
Pravec, P., Harris, A. W., Vokrouhlický, D., et al. 2008, Icar, 197, 497
Pravec, P., Vokrouhlický, D., Polishook, D., et al. 2010, Natur, 466, 1085
Reddy, V., Sanchez, J. A., Bottke, W. B., et al. 2014, Icar, 237, 116
Reddy, V., Sanchez, J. A., Gaffey, M. J., et al. 2012, Icar, 221, 1177
Richardson, D. C., Leinhardt, Z. M., Melosh, H. J., Bottke, W. F., & Asphaug, E. 2002, in Asteroids III, ed. W. F. Bottke et al. (Tucson, AZ: Univ. Arizona Press), 501
Richardson, J. E., Melosh, H. J., & Greenberg, R. 2004, Sci, 306, 1526
Richardson, J. E., Melosh, H. J., Greenberg, R. J., & O'Brien, D. P. 2005, Icar, 179, 325
Robbins, S. J. 2014, E&PSL, 403, 188
Robinson, M. S., Thomas, P. C., Veverka, J., Murchie, S. L., & Wilcox, B. B. 2002, M&PS, 37, 1651
Rubincam, D. P. 2000, Icar, 148, 2
Runyon, K. D., & Barnouin, O. S. 2015, LPI, 1832, 2869
Russell, C. T., Raymond, C. A., Ammannito, E., et al. 2016, Sci, 353, 1008
Russell, C. T., Raymond, C. A., Coradini, A., et al. 2012, Sci, 336, 684
Ryan, E. L., Mizuno, D. R., Shenoy, S. S., et al. 2015, A&A, 578, A42
Scheeres, D. J., Britt, D., Carry, B., & Holsapple, K. A. 2015, in Asteroids IV, ed. P. Michel, F. DeMeo, & W. F. Bottke (Tucson, AZ: Univ. Arizona Press), 745
Scheeres, D. J., McMahon, J. W., French, A. S., et al. 2019, NatAs, 3, 352
Schenk, P., O'Brien, D. P., Marchi, S., et al. 2012, Sci, 336, 694

Schmedemann, N., Kneissl, T., Ivanov, B. A., et al. 2014, P&SS, 103, 104
Schmidt, R. M., & Housen, K. R. 1987, IJIE, 5, 543
Ševeček, P., Brož, M., & Jutzi, M. 2019, A&A, 629, A122
Shoemaker, E. M. 1962, in Physics and Astronomy of the Moon, ed. Z. Kopal (New York: Academic), 283
Sierks, H., Lamy, P., Barbieri, C., et al. 2011, Sci, 334, 487
Spoto, F., Milani, A., & Knežević, Z. 2015, Icar, 257, 275
Statler, T. S. 2009, Icar, 202, 502
Stokes, G., Barbee, B. W., Bottke, W. F., et al. 2017, Update to Determine the Feasibility of Enhancing the Search and Characterization of NEOs, Report of the Near-Earth Object Science Definition Team (Washington, D.C: Science Mission Directorate, Planetary Science Division, NASA)
Sugita, S., Honda, R., Morota, T., et al. 2019, Sci, 364, 252
Takahashi, Yu., Busch, M. W., & Scheeres, D. J. 2013, AJ, 146, 95
Tatsumi, E., & Sugita, S. 2018, Icar, 300, 227
Terada, K., Sano, Y., Takahata, N., et al. 2018, NatSR, 8, 11806
Thomas, N., Barbieri, C., Keller, H. U., et al. 2012, P&SS, 66, 96
Thomas, P. C., Belton, M. J. S., Carcich, B., et al. 1996, Icar, 120, 20
Thomas, P. C., Joseph, J., Carcich, B., et al. 2002, Icar, 155, 18
Thomas, P. C., & Robinson, M. S. 2005, Natur, 436, 366
Thomas, P. C., Veverka, J., Bell, J. F., et al. 1999, Icar, 140, 17
Thomas, P. C., Veverka, J., Simonelli, D., et al. 1994, Icar, 107, 23
Trombka, J. I., Squyres, S. W., Brückner, J., et al. 2000, Sci, 289, 2101
Vedder, J. D. 1998, Icar, 131, 283
Vernazza, P., Binzel, R. P., Thomas, C. A., et al. 2008, Natur, 454, 858
Vernazza, P., Zanda, B., Binzel, R. P., et al. 2014, ApJ, 791, 120
Veverka, J., Thomas, P., Harch, A., et al. 1997, Sci, 278, 2109
Veverka, J., Thomas, P., Harch, A., et al. 1999, Icar, 140, 3
Vokrouhlický, D., Bottke, W. F., Chesley, S. R., Scheeres, D. J., & Statler, T. S. 2015, in Asteroids IV, ed. P. Michel, F. DeMeo, & W. F. Bottke (Tucson, AZ: Univ. Arizona Press), 509
Vokrouhlický, D., Bottke, W. F., & Nesvorný, D. 2016, AJ, 152, 39
Vokrouhlický, D., Bottke, W. F., & Nesvorný, D. 2017, AJ, 153, 172
Vokrouhlický, D., Nesvorný, D., & Bottke, W. F. 2003, Natur, 425, 147
Vokrouhlický, D., Pokorný, P., & Nesvorný, D. 2012, Icar, 219, 150
Walsh, K. J., Delbó, M., Bottke, W. F., Vokrouhlický, D., & Lauretta, D. S. 2013, Icar, 225, 283
Walsh, K. J., & Jacobson, S. A. 2015, in Asteroids IV, ed. P. Michel, F. DeMeo, & W. F. Bottke (Tucson, AZ: Univ. Arizona Press), 375
Walsh, K. J., Jawin, E. R., Ballouz, R. -L., et al. 2019, NatGe, 12, 242
Walsh, K. J., Morbidelli, A., Raymond, S. N., O'Brien, D. P., & Mandell, A. M. 2011, Natur, 475, 206
Watanabe, S., Hirabayashi, M., Hirata, N., et al. 2019, Sci, 364, 268
Wetherill, G. 1967, JGR, 72, 2429
Williams, D., Kneissl, T., Neesemann, A., et al. 2018, Icar, 316, 99
Williams, D. R., & Wetherill, G. W. 1994, Icar, 107, 117
Yoshida, F., & Nakamura, T. 2007, P&SS, 55, 1113
Yoshida, F., Nakamura, T., Watanabe, J.-I., et al. 2003, PASJ, 55, 701
Zappalà, V., Cellino, A., & Dell'Oro, A. 2001, Icar, 157, 280
Zappalà, V., Cellino, A, Di Martino, M., Migliorini, F., & Paolicchi, P. 1997, Icar, 129, 1